ICCC 2023 - Guidelines for citation and reuse

Please cite the conference proceedings as following:
Thailand Concrete Association, Ed. *Further Reduction of CO2 -Emissions and Circularity in the Cement and Concrete Industry, 16th International Congress on the Chemistry of Cement 2023 - ICCC2023* (Bangkok 18.-22.09.2023). Bangkok, 2023. Available at: https://www.iccc-online.org/archive/

Please cite individual papers as following:
Author. Title. In: Thailand Concrete Association, Ed. *Further Reduction of CO2 -Emissions and Circularity in the Cement and Concrete Industry, 16th International Congress on the Chemistry of Cement 2023 - ICCC2023* (Bangkok 18.-22.09.2023). Bangkok, 2023. Available at: https://www.iccc-online.org/archive/

Organized by

TCA
สมาคมคอนกรีตแห่งประเทศไทย
Thailand Concrete Association

THE 16TH INTERNATIONAL CONGRESS ON THE CHEMISTRY OF CEMENT
ICCC 2023
BANGKOK THAILAND

ICCC 16th
2023
INTERNATIONAL CONGRESS ON THE CHEMISTRY OF CEMENT

CONGRESS PROCEEDING VOLUME V

Further reduction of CO_2-emission
and circularity in the cement and concrete industry

SEPTEMBER 18-22, 2023

CENTARA GRAND & BANGKOK CONVENTION CENTRE @CENTRALWORLD

Co-Sponsor by

aci American Concrete Institute *Always advancing*

SEADMA

ACF ACF Concrete World

gcca Global Cement and Concrete Association

ASTM ASTM INTERNATIONAL

Contact infomation :
Email: iccc2023.tca@gmail.com
Website : https://www.iccc2023.org/

PREFACE

The International Congress on the Chemistry of Cement (ICCC) is the renowned global platform that summarizes the state of the art of cement chemistry as well as major trends in cement application. Since the first International Congress on the Chemistry of Cement started in London in 1918, it has provided a strong and fruitful link between the academic world and the cement industry. It has always stimulated scientific exchanges and discussions between researchers, students, and those who have already gained working experience in many fields of chemistry relevant to cement production and its use in concrete and mortar. The ICCC is the venue to present cement and environmental development together with meeting worldwide and renowned experts from all over the world who come to present their works at the congress.

This proceeding collects the papers submitted to the 16th International Congress on the Chemistry of Cement (ICCC 2023), which was held in Bangkok, Thailand between September 18-22, 2023, and organized by Thailand Concrete Association on the theme of "further reduction of CO2-emission and circularity in the cement and concrete industry". The ICCC 2023 attracted more than 565 papers and more than 800 delegates and students from 49 countries.

The scientific program covers the topics of the newest and the most important research and development describing the new dimensions in clinker production, advances in hydration chemistry, enhancing clinker substitution and supplementary cementitious materials, advances in characterization methods and modelling, new low carbon cement and carbonatable binders, new findings in admixture & rheology, new technology for quality concrete, durability & reactive transport, sustainability, circular economy, waste processing and recycling, and standardization of cement and concrete.

The Organizing Committee and the Scientific Committee believe that our participants will be most satisfied with the congress and will gain the knowledge to improve their professional works in the future.

Prof.Thanakorn Pheeraphan
Chairman of the Organizing Committee

Prof.Somnuk Tangtermsirikul
Chairman of the Scientific Committee

Steering Committee Members

The Steering Committee is comprised of 26 members.

1. Prof. Dr. Mark G. Alexander, University of Cape Town, South Africa
2. Prof. Dr. Alexandra Bertron, INSA Toulouse, France
3. Prof. Dr. Shashank Bishnoi; Indian Institute of Technology Delhi, India
4. Prof. Dr. Leon Black, University of Leeds, United Kingdom
5. Dr. Cesar Constantino; Titan America LLC, USA
6. Jesper Sand Damtoft, Aalborg Portland A/S, Denmark
7. Prof. Dr. Jan Deja; Stowarzyszenie Producentów Cementu – PCA, Poland
8. Dr. Wolfgang Dienemann, HeidelbergCement AG, Germany
9. Daniel Duque, Cementos Argos S.A., Columbia
10. Ing. Jan Gemrich, Czech Cement Association, Czech Republic
11. Prof. Dr. Frederik Paul Glasser, University of Aberdeen, Scotland
12. Prof. Dr. R. Doug Hooton, University of Toronto, Canada
13. Prof. Dr. Vanderley M. John, Escola Politécnica da USP, Brasil
14. Prof. Dr. Kimberly Kurtis, Georgia Institute of Technology, USA
15. Christophe Levy, Lafarge Holcim Innovation Center (Chairman), France
16. Prof. Dr. Ippei Maruyama, Nagoya University Furocho, Japan
17. Dr. Bibekananda Mohapatra, Director General of the National Council for Cement and Building Materials, India
18. Dr. Marta Palacios, Instituto Eduardo Torroja, Spain
19. Prof. Dr. Angel Palomo, Instituto Eduardo Torroja, Spain
20. Prof. Dr. Thanakorn Pheeraphan, Thailand Concrete Association (Deputy-Chairman), Thailand
21. Prof. Dr. Martin Schneider, VDZ e.V., Research Institute, Germany
22. Prof. Dr. Karen Scrivener, École Polytechnique Fédérale de Lausanne – EPFL, Switzerland
23. Prof. Dr. Caijun Shi, Hunan University, China
24. Prof. Dr. Sui Tongbo, Sinoma International Engineering Co., Ltd., China
25. Prof. Dr. Jannie S. J. Van Deventer, Zeobond Pty Ltd, Australia
26. Dr. Kazuo Yamada, National Institute for Environmental Studies, Japan

Dr. Joerg Rickert, VDZ (Permanent Secretariat of ICCC), Germany - (Without the right to vote)

Organizing Committee Members

Advisory committee members
1. Dr. Wonchalerm Chalodhorn, Siam City Cement Co. Ltd.
2. Prof.Dr. Chai Jaturapitakkul, King Mongkut's University of Technology Thonburi
3. Prof.Dr. Parinya Jindaprasert, KhonKaen University
4. Mr. Ferdinand Leopolder, The South East Asia Drymix Mortar Association SEADMA,
5. Assoc.Prof.Dr. Pichai Nimityongskul , 1st President of Thailand Concrete Association
6. Mr. Chakporn Oonjitt, Construction Institute of Thailand
7. Mr. Wanchai Phanomchai, Thai Industrial Standards Institute
8. Mr. Chana Poomee, Thai Cement Manufacturers Association
9. Dr. Phirun Saiyasitpanich, Office of Natural Resources and Environmental Policy and Planning
10. Mr. Manasit Sarigaphuti, The Siam Cement Group Public Company Limited
11. Assoc.Prof. Anek Siripanichgorn, Engineering Institute of Thailand
12. Prof.Dr. Boonchai Stitmannaithum, Chulalongkorn University
13. Prof.Dr. Piti Sukontasukkul, King Mongkut's University of Technology North Bangkok
14. Mr. Sumate Surabotsopon, Italian-Thai Development Public Company Limited
15. Prof.Dr. Somnuk Tantermsirikul, Sirindhorn International Institute of Technology
16. Dr. Saranyu Viriyavejakul, Neighboring Countries Economic Development Cooperation Agencies
17. Prof.Dr. Pennung Warnitchai, Asian Institute of Technology
18. Mr. Boonyanit Wongrukmit, Electricity Generating Authority of Thailand

Organizing Committee members

1. Prof.Dr. Thanakorn Pheeraphan, Thailand Concrete Association and NavamindaKasatriyadhiraj Royal Air Force Academy (Chairman)
2. Asst.Prof. Dr. Chuchai Sujivorakul, King Mongkut's University of Technology Thonburi (Deputy Chairman)
3. Mr. Boonrawd Kuptitanhi, The Concrete Products and Aggregate Co., Ltd. (Treasurer)
4. Asst.Prof.Dr. Nattapong Magaratat , King Mongkut's University of Technology North Bangkok (Secretariat)
5. Dr. Praveen Chompreda, K.C.S. & ASSOCIATES. Co., Ltd.
6. Assoc.Prof.Dr. Phongthorn Julphunthong, Naresuan University
7. Miss Sunkamol Khongsawatvorakul, Saint-Gobain Thailand.
8. Mr. Sumet Kiatmetha, Hilti (Thailand) Ltd.
9. Gp.Capt. Nuth Limsuwan, Office of Civil Engineering Royal Thai Armed Forces.
10. Dr. Nontapat Nimityongskul, Asia Cement Public Company Limited.
11. Assoc.Prof. Panuwat Joykad, Srinakharinwirote University
12. Dr. Yut Panitanwong, Concrete Product and Aggregate Co.,Ltd.
13. Mr. Suwatchai Puwapattanachat, SIKA (Thailand) Ltd.
14. Mr. Narin Sayanwisuttikam, KAO Industrial (Thailand) Co., Ltd.
15. Dr. Kritsada Sisomphon, The Siam Cement Group Public Company Limited.
16. Mr. Chalermwut Snguanyat, The Siam Cement Group Public Company Limited.
17. Mr. Pakorn Sutthiwaree, Siam City Cement Public Company Limited.
18. Assoc.Prof.Dr. Weerachart Tangchirapat, King Mongkut's University of Technology Thonburi
19. Asst. Prof. Dr. WarangkanaSaengsoy, Construction and Maintenance Technology Research Center, SIIT
20. Prof.Dr. Wanchai Yodsudjai, Kasetsart University

Scientific Committee Members

1. Prof.Mark Alexander, South Africa
2. Prof.Carmen Andrade, Spain
3. Prof.Sergio Angulo, Brazil
4. Dr.Mohsen Ben Haha, Germany
5. Prof.Susan Bernal Lopez, UK
6. Prof.Alexandra Bertron, France
7. Prof.Shashank Bishnoi, India
8. Prof.Maria Blanco, Spain
9. Prof.Jeff Bullard, USA
10. Prof.Maria Alba Cincotto, Brazil
11. Prof.Jan Deja, Poland
12. Prof.Donguk Choi, South Korea
13. Prof.Josee Duchesne, Canada
14. Mr.Wilmar Echeverri, Colombia
15. Prof.Ivan Escalante, Mexico
16. Dr.Duncan Herfort, Denmark
17. Prof.Bruno Huet, France
18. Prof.Jason Ideker, USA
19. Prof.Edgardo Irassar, Argentinia
20. Prof.Zhengwu Jiang, China
21. Prof.Maria Juenger, USA
22. Dr.Marios Katsiotis, Greece
23. Prof.Shiho Kawashima, USA
24. Prof.Paula Kirchheim, Brazil
25. Prof.Jiaping Liu, China
26. Mr.Federico Lopez, Mexico
27. Prof.Barbara Lothenbach, Switzerland
28. Prof.Horst Ludwig, Germany
29. Prof.Ippei Maruyama, Japan
30. Prof.Thomas Matschei, Germany
31. Mr.Mike McDonald, South Africa
32. Dr.Sean Monkman, Canada
33. Prof.Paulo Monteiro, USA
34. Mr.Carlos Orozco, Colombia
35. Dr.Marta Palacios, Spain
36. Prof.Martin Palou, Slovakia
37. Dr.César Pedrajas, Spain
38. Prof.Rafael Pileggi, Brazil
39. Prof.Kedsarin Pimraksa, Thailand
40. Prof.John Provis, UK
41. Prof.Francisca Puertas, Spain

Scientific Committee Members

42. Prof.Jueshi Qian, China
43. Prof.Aleksandra Radlinska, USA
44. Dr.Nailia Rakhimova, Russia
45. Prof.Matteo Romano, Italy
46. Prof.Nicolas Roussel, France
47. Dr.Kwesi Sagoe-Crentsil, Australia
48. Prof.Manu Sanathanam, India
49. Prof.Miguel Sanjuán, Spain
50. Prof.Caijun Shi, China
51. Dr.Denise Silva, USA
52. Prof.Somnuk Tangtermsirikul, Thailand   (Chairman)
53. Dr.Theodor Staněk, CZ
54. Prof.Arezki Tagnit-Hamou, Canada
55. Mr.Antonio Telesca, Italy
56. Dr.Paul Tennis, USA
57. Prof.Michael Thomas, Canada
58. Prof.Jorge Tobon, Canada
59. Prof.Sandro Torres, Brazil
60. Prof.Matthieu Vandamme, France
61. Dr.Yury Villagrán Zaccardi, Argentina
62. Prof.Fazhou Wang, China
63. Prof.Zhang Wensheng, China
64. Prof.Claire White, USA
65. Dr.Frank Winnefeld, Switzerland
66. Dr.Hong Wong, UK
67. Dr.Kazuo Yamada, Japan
68. Prof.Cheng Yu, China
69. Prof.Doug Hooton, Canada
70. Peter Kruspan, Switzerland

Contents

Contents

Hydration mechanism of wollastonite-blended magnesium potassium phosphate cements

Biwan Xu[1,2*], Barbara Lothenbach[2], and Frank Winnefeld[2]

[1] *Department of structural engineering, 200092 Shanghai, China*

Email: xubiwan@tongji.edu.cn
[2] *Laboratory for Concrete & Asphalt, Swiss Federal Laboratories for Materials Science and Technology (Empa), 8600 Dübendorf, Switzerland.*

Email: Barbara.Lothenbach@empa.ch Email: Frank.Winnefeld@empa.ch

ABSTRACT

Magnesium potassium phosphate (MKP) cement has been mainly used as rapid repair materials in the field of civil engineering and as immobilization material for heavy metals and low-level nuclear wastes in the field of waste management. The addition of wollastonite as a supplementary material in MKP cement can improve the cement properties such as efflorescence resistance, heat resistance, flexural and compressive strengths. However, the role of wollastonite in MKP cements is yet not well understood. This study explores the hydration mechanisms of wollastonite-blended MKP cements considering the impact of the key factors such as magnesium-to-phosphate (Mg/PO_4) molar ratio and water-to-solid (w/s) ratio through experimental approaches and thermodynamic modelling. The experimental results show a higher wollastonite reaction in MKP cements with a lower Mg/PO_4 molar ratio. Less magnesia reacted establishes a lower pH value, which is favorable for the reaction of wollastonite. The hydration of wollastonite does not lead to the formation of crystalline hydrates, but to the precipitation of amorphous hydroxyapatite and magnesium silicate hydrate (M-S-H) as suggested by both experimental and thermodynamic findings. Those phases largely contribute to higher flexural and compressive strengths of the MKP cements at later ages.

KEYWORDS: *Magnesium potassium phosphate cement; Wollastonite; Hydration mechanism; Thermodynamic modelling.*

1. Introduction

Magnesium potassium phosphate (MKP) cement is an alternative to Portland cement. Generally, the main hardening mechanism of MKP cement can be described through the following equation, giving K-struvite ($MgKPO_4 \cdot 6H_2O$) as main hydration product.

$$MgO + KH_2PO_4 + 5H_2O \rightarrow MgKPO_4 \cdot 6H_2O \tag{1}$$
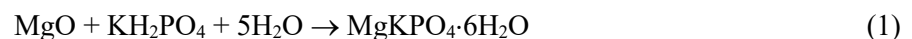
Wollastonite ($CaSiO_3$) is an inosilicate mineral and has been used in cementitious materials for decades (Low and Beaudoin (1992)). The use of wollastonite in MKP cements can improve cement properties such as efflorescence resistance (Xu et al. (2020)), heat resistance (Gao et al. (2016)), flexural and compressive strengths (Xu et al. (2020, 2021)); however, the role of wollastonite in MKP cements is not yet well understood. This study explores the hydration mechanisms of wollastonite-blended MKP cements considering the key factors of magnesium-to-phosphate (Mg/PO_4) molar ratio and water-to-solid (w/s) ratio through experimental approaches and thermodynamic modelling.

2. Experimental

Dead-burnt magnesia (MgO), monopotassium dihydrogen phosphate (KH$_2$PO$_4$) and wollastonite were used as starting materials (Xu et al. (2020, 2021)). The MKP cements were prepared at Mg/PO$_4$ molar ratios of 2.7 and 4, w/s ratios of 0.25, 0.5, and 5, and with wollastonite at the levels of 0, 35%, and 40%, by weight of the binder (sum of magnesia, KH$_2$PO$_4$ and wollastonite). The samples were cured at 20 °C and 70% relative humidity (RH). Flexural and compressive strengths were determined on two prisms with the dimension 20 mm × 20 mm × 100 mm. The solid phase assemblages of the hydrated pastes were determined by X-ray diffraction (XRD) and thermogravimetric analysis (TGA). The pH development in MKP cement suspensions was monitored in-situ for 24 h. The sample preparation and test protocols were detailed in (Xu et al. (2019)). Thermodynamic modelling was carried out using the geochemical GEMS-PSI software, coupled with the thermodynamic data for magnesium potassium phosphates (Lothenbach et al. (2019)).

3. Results and discussion

3.1 Flexural and compressive strength of pastes

As displayed in **Fig. 1**, the MKP cements without wollastonite show better strengths at the higher Mg/PO$_4$ molar ratio of 4. The strength reduction at lower Mg/PO$_4$ molar ratio of 2.7 over time could be attributed to the unreacted KH$_2$PO$_4$, formation of intermediate hydrates, and thus to potential expansion and micro-cracking (Xu et al. (2019)). The use of wollastonite greatly improves the strengths, especially at later ages. Furthermore, the wollastonite-blended MKP cements demonstrate higher strengths at the lower Mg/PO$_4$ molar ratio of 2.7, in contrast to the plain MKP cements without wollastonite.
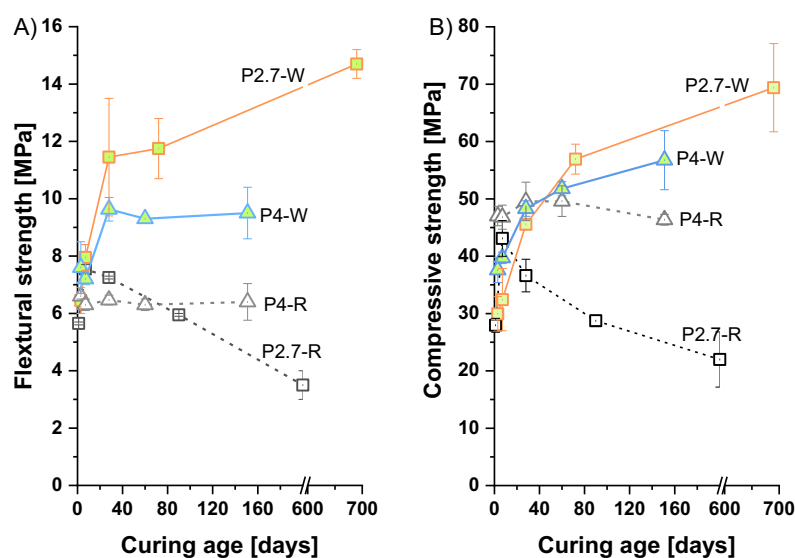
Fig. 1 A) Flexural strength, B) compressive strength of the MKP cement pastes at w/s ratio of 0.25 without (P2.7-R and P4-R) / with wollastonite (P2.7-W and P4-W). The number in the sample names refers to the molar Mg/PO$_4$ ratio. Note that the wollastonite levels in the samples P2.7-W and P4-W are 40% and 35%, respectively.

3.2 Hydration kinetics

The pH-development of the suspensions share two common characteristic maxima (P1, P2) as labelled in **Fig. 2**. Compared with the plain MKP cement suspensions, the use of wollastonite extends the plateau after the peak P2 to later reaction time, especially for the lower Mg/PO$_4$ molar ratio of 2.7, indicating the slowed-down MgO reaction. Further, the pH values of the wollastonite-blended MKP cement suspensions after 24 h are reduced by around 1.2 units, which can be attributed to the lower portion of MKP cement used in the blend and to partial chemical reaction of wollastonite.
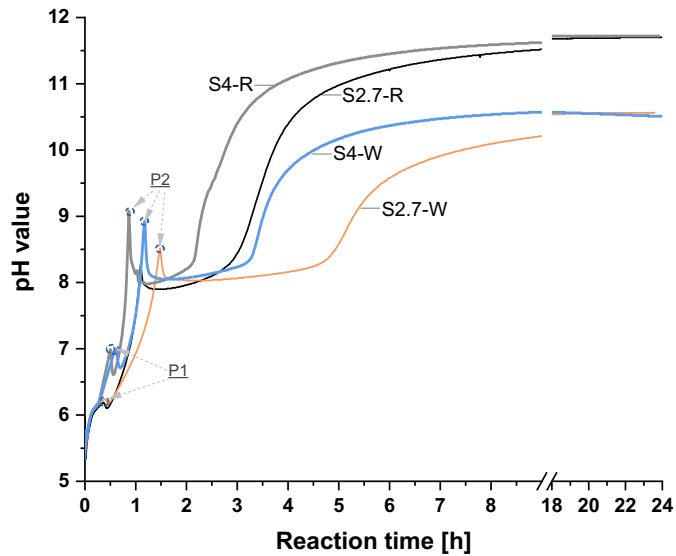
Fig. 2 The pH development curves of the MKP cement suspensions at w/s ratio of 5 without (S2.7-R and S4-R) / with wollastonite (S2.7-W and S4-W). Note that the wollastonite levels in the samples S2.7-W and S4-W are 40% and 35%, respectively.

3.3 Phase assemblage

The effect of the Mg/PO_4 molar ratio on the hydrate assemblages of wollastonite-blended MKP cements is predicted as given in **Fig. 3**. At lower Mg/PO_4 molar ratios, hydrates such as newberyite ($MgHPO_4 \cdot 3H_2O$), brushite ($CaHPO_4 \cdot 2H_2O$), $CaK_3H(PO_4)_2$ are more likely to form due to the lower pH. The increase of the Mg/PO_4 molar ratio increases the pH, thus favoring precipitation of hydrates such as K-struvite, calcium hydroxyapatite (HAP), magnesium silicate hydrate (M-S-H), and even traces of brucite.
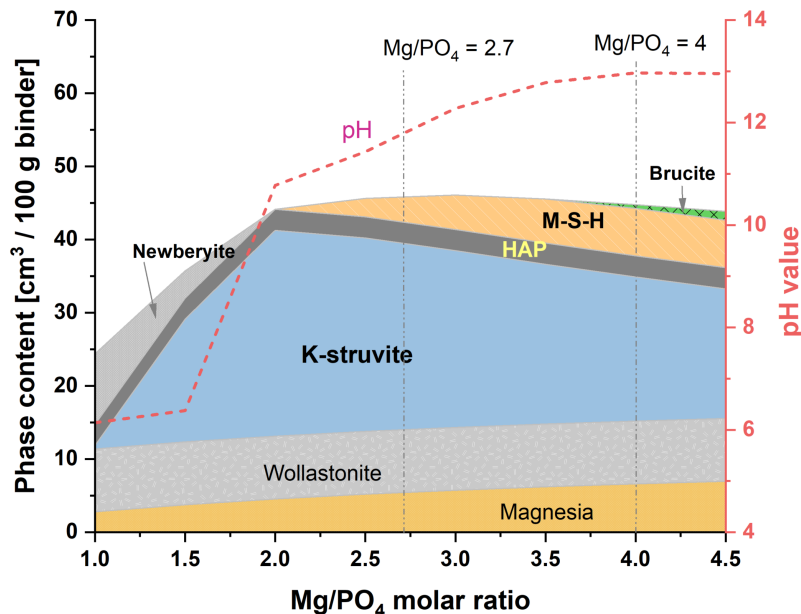
Fig. 3 Phase assemblages of wollastonite-blended MKP cement pastes as predicted by thermodynamic modelling, considering Mg/PO_4 molar ratios from 1 to 4.5, a w/s ratio of 0.5, a wollastonite level of 35% (by weight of binder), and reaction degrees of magnesia and wollastonite of 0.35 and 0.30, respectively.

Consistent with the modelling results, the XRD and TGA results given in **Fig. 4** confirm K-struvite as the main hydrate in wollastonite-blended MKP cements; however, no additional crystalline hydrate was determined by XRD in both pastes. The further hydrates predicted by thermodynamic modelling such as HAP and M-S-H may exist in ill-crystalline or amorphous forms as evidenced by energy-disperse

3

microanalyses in (Xu et al. (2020, 2021)). The potential presence of some M-S-H is also mirrored in the slightly increased water loss between 300 to 600°C. In addition, the TGA data of the sample P2.7-W* shows a small weight loss at around 700 °C, indicating the formation of a small amount of calcite.
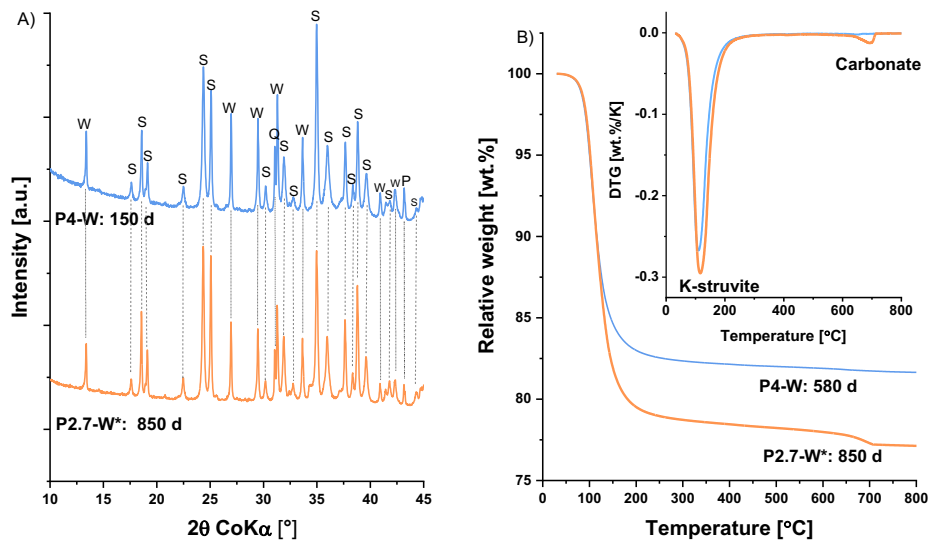
Fig. 4 A) XRD patterns and B) TGA/DTG curves of the wollastonite-blended MKP cement pastes at Mg/PO_4 molar ratios of 2.7 and 4. Note that the samples P2.7-W* and P4-W were prepared at w/s ratio of 0.5 and 0.25. The wollastonite levels in the samples P2.7-W* and P4-W were 40% and 35%, respectively. S = K-struvite ($MgKPO_4 \cdot 6H_2O$), Q = quartz (SiO_2), W = wollastonite-*2M* ($CaSiO_3$).

3. Conclusions

Wollastonite can be used as an effective supplementary cementitious material in MKP cements, which can not only help to lower the CO_2 emissions by replacing a part of the dead-burnt magnesia, but also improves cement performance. This study explored the influence of wollastonite on mechanical strength and hydration of MKP cements at different Mg/PO_4 molar ratios through experimental approaches and via thermodynamic modelling. The experimental findings show that wollastonite can well improve strengths of MKP cements at later age, in particular at lower Mg/PO_4 molar ratios. Wollastonite reacts more at lower Mg/PO_4 molar ratios, and forms ill-crystalline or amorphous phases, such as calcium hydroxyapatite (HAP) and magnesium silicate hydrate (M-S-H) as suggested by thermodynamic modelling.

Acknowledgements

References

Gao, X., Zhang, A., Li, S. and Sun, B. (2016) "The resistance to high temperature of magnesia phosphate cement paste containing wollastonite", *Materials and Structures*, 49: 3423-3434.

Low, N.M.P. and Beaudoin, J.J. (1992) "Mechanical properties of high-performance cement binders reinforced with wollastonite micro-fibers", *Cement and Concrete Research*, 22: 981-989.

Lothenbach, B., Xu, B. and Winnefeld, F. (2019) "Thermodynamic data for magnesium (potassium) phosphates", *Applied Geochemistry*, 111: 104450.

Xu, B., Winnefeld, F., Kaufmann, J. and Lothenbach, B. (2019) "Influence of magnesium-to-phosphate ratio and water-to-cement ratio on hydration and properties of magnesium potassium phosphate cements", *Cement and Concrete Research*, 123: 105781.

Xu, B., Lothenbach, B. and Winnefeld, F. (2020) "Influence of wollastonite on hydration and properties of magnesium potassium phosphate cements", *Cement and Concrete Research*, 131: 106012.

Xu, B., Winnefeld, F. and Lothenbach, B. (2021) "Effect of temperature curing on properties and hydration of wollastonite blended magnesium potassium phosphate cements", *Cement and Concrete Research*, 142: 106370.

Accelerating mechanism of calcium additives on alkali activated cementitious material

Feng Wu, Hui Li, Huimei Zhu

（*College of Material Science and Engineering, Xi'an University of Architecture and Technology，Xi'an, 710055*）

Abstract: In this paper, the alkali activated cementitious materials (AAMs) were prepared with coal gasification residue as raw material and NaOH as alkali activator, different calcium materials were added to AAMs, the effects of different calcium additives on the mechanical properties and micro morphology of AAMs were compared, the accelerating mechanism of different calcium additives was discussed. The results shows that the different calcium additives presents different mechanisums of enhacing the strength and optimizing microstructure obviously. $Ca(OH)_2$ provides non-uniform surface and easier to generate C-S-H gel with high Si / Ca ratio, and the strength of AAMs was obviously improved. PC (ordinary portland cement) needs to be hydrated to generate $Ca(OH)_2$ and then participate in the C-S-H gels formation reaction, the acceleration effect was poor. The C-S-H gel and C-A-S-H gel production of AAMs can be promoted with the addition of 5% $Ca(OH)_2$. The crystallization degree and microstructure of hydration products can obviously enhance, and the pore structure and distribution are optimized, the effect of the accelerated agent is more obvious.

Keywords: *AAMs, calcium additives, accelerating effect, mechanical properties, microstructure.*

Introduction

AAMs is a new type of binder that replaces cement with environmentally friendly materials. It is a product of the reaction between aluminum silicate and alkali activator, and has a three-dimensional network structure. The most common precursors of AAMs are fly ash (FA), ground blast furnace slag (GGBFS) and metakaolin, a by-product of traditional industry. CGR should be a pozzolanic active mineral (I. Yoshitaka. 2012). Domestic scholars have shown that CGR has volcanic ash activity and has a good contribution to the flow ability and strength of cement-based materials (S. Fang, et al., 2020). Coal gasification residue should have a certain pozzolanic activity, which can be used as the precursor of AAMs. However, such studies are rarely reported. The type of hydration products of AAMs has a great relationship with the calcium content in the raw materials, the amount of calcium element in the raw material affects the type of hydration product. On the basis of previous studies, this paper focuses on the influence of adding different calcareous materials to alkali activated coal gasification slag based cementitious materials on their strength development and hydration product types.

1 Experiment

1.1 Raw material

The CGR chemical composition is shown in Table 1, and its mineral composition is shown in Figure 1. It can be seen that the coal gasification slag is mainly rich in SiO_2, Al_2O_3, Fe_2O_3 and CaO, with the total content of more than 80%. It should has potential cementitious activity, which can be used as raw materials for AAMs. The carbon content of CGR used is 1.52%, with a specific surface area of 320 m^2/kg and a density of 2.72 g/cm^3. The alkali activator used in the experiment is analytically pure sodium hydroxide. The calcium additives used are cement and calcium hydroxide. The cement is made by mixing

95% clinker with 5% gypsum (with a CaO content of 60%), with a specific surface area of 330 m^2/kg and a density of 3.27 g/cm^3; Calcium hydroxide is analytically pure.

Table 1 The composition of CGR / wt%

Oxide	SiO₂	Al₂O₃	CaO	Fe₂O₃	MgO	Na₂O	K₂O	P₂O₅	SO₃	Other	LOI
Content	48.75	20.05	10.69	9.67	2.84	1.65	2.11	0.17	0.56	1.88	1.52
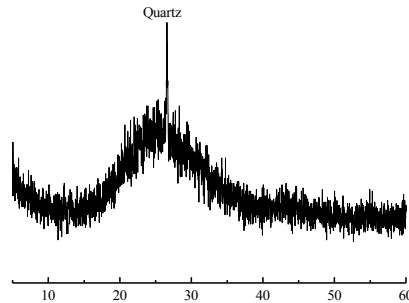
Fig.1 Mineral composition of CGR

1.2 Sample preparation and testing methods

Preparation of AAMs: Weigh 5% sodium hydroxide and dissolve it in water to prepare an alkali solution. Add 95% solid sample to the alkali solution and stir evenly to obtain a slurry. Pour it into 3 cm × 3 cm ×5cm trial mold, it is compacted and smoothed, and steam cured at 80 ℃ for 24 hours before demolding. It is then transferred to a standard curing box for curing until the specified age, and its compressive strength is tested. Crush the sample and soak it in alcohol to terminate hydration. Mineral composition analysis was conducted using a D/Max 2200 X-ray diffractometer (XRD). The molecular structure was analyzed by PerkinElmer Spectrum Two Fourier transform infrared spectrometer (FTIR). Observe the microstructure of hydration products using JSM 5900 scanning electron microscopy (SEM).

2. Test Results and Discussion

2.1 Macromechanical properties

Table 2 Mix ratio of PC and Ca(OH)₂ in AAMs

Type	CGS / wt%	NaOH / wt%	PC / wt%	Ca(OH)₂/wt%	W/C	Curing temperature/℃
NH	95	5%		—	0.4	80 (24h)
NH-PC	95	5%	10%	—	0.4	80 (24h)
NH-CH	95	5%	—	5%	0.4	80 (24h)
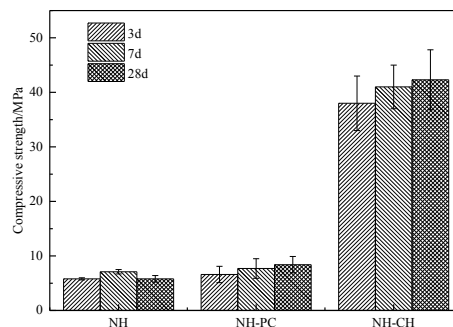
Fig.2 Effect of different calcium additives on compressive strength of AAMs

Table 2 shows the proportion of different calcium raw materials added to AAMs. It can be seen that

when the AAMs hardens to 28 days, its compressive strength decreases to a certain extent compared to 7 days, and there is a phenomenon of strength shrinkage. The addition of PC and Ca(OH)₂ into AAMs has a significant difference in their macroscopic mechanical properties. Ca(OH)₂ has a strong promoting and enhancing effect on coagulation. Ca(OH)₂ can significantly increase the compressive strength of the sample at 3 days, 7 days, and 28 days, with an increase of 555%, 432%, and 629%. The effect of PC on the strength development of the sample is similar to that of Ca(OH)₂, but the reinforcement effect of PC is relatively weak. The addition of Ca(OH)₂ and PC can counteract the phenomenon of later strength shrinkage of AAMs.

2.2 Mineral Phase Analysis (XRD)

(a. 3 days)   (b. 28 days)
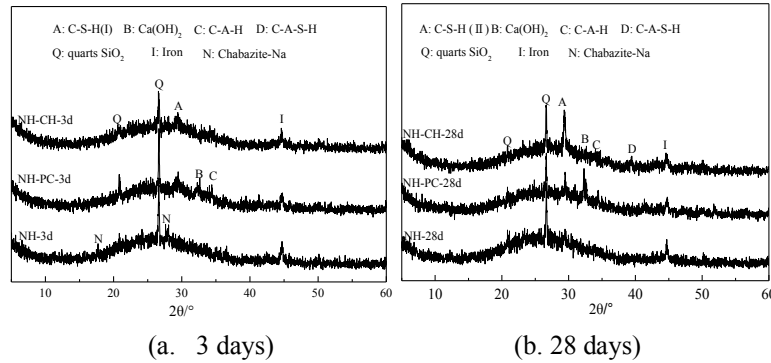
Fig.3 XRD patterns of AAMs after adding calcium at age of 3 days and 28 days

Figure 3 shows the XRD patterns of AAMs hardened with PC and Ca(OH)₂ slurry for 3 days and 28 days. When 10% PC was added, the hydration products showed obvious C-S-H (I) characteristic peaks. Compared with NH system; When 5% Ca(OH)₂ was added, a more obvious C-S-H characteristic peak appeared, and the amorphous hump in CGR became smoother, indicating that more active Si and Al were dissolved to participate in the reaction. It is reported that normally, cement hydration should form C-S-H (II) with a high Ca/Si ratio. Since the PC content in this test is only 10% (CaO content is 60%), another type of gel with low Ca/Si ratio has been formed (Tang, Z., et al., 2019). The characteristic peaks of C-S-H and C-A-S-H can be found in XRD, but the characteristic peaks of N-A-S-H cannot be identified, we will discuss the effect of adding different calcium materials on the formation of rules of C-A-S-H and N-A-S-H in AAMs by FTIR.

2.3 Fourier transform infrared analysis (FTIR)
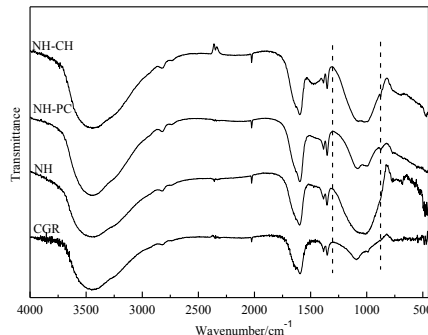
Fig.4 FTIR spectra of hydration products of AAMs after adding calcium

Figure 4 shows the 28 days FTIR spectrum of AAMs calcium doped hardening. After the addition of PC and Ca(OH)₂, there is an obvious Si-O-Si contraction vibration peak between 1200 and 900 cm⁻¹, in which 980~1000 cm⁻¹ and 1050~1100 cm⁻¹ respectively correspond to the absorption bands of hydrated

C-A-S-H and N-A-S-H. The strength and width of the expansion vibration spectrum in the range of 1200 cm^{-1}~900 cm^{-1} vary depending on the calcium source added, It can also be confirmed that hydration reaction occurred after calcium was added into AAMs, and at the same time, the formation of C-A-S-H reduced the content of N-A-S-H, and the strength of cementitious materials was greatly improved. Adding calcareous additives to the N-A-S-H gel can not only modify the aggregation morphology of the N-A-S-H gel, but also promote the formation and aggregation of the C-S-H gel and the C-A-S-H gel.

2.4 Microstructure (SEM)

(a)   (b)   (c)
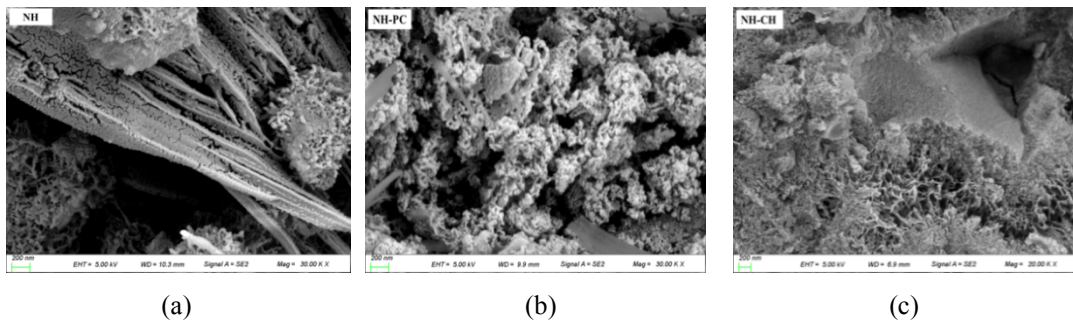
Fig.5 SEM of samples hardened for 28 days after adding calcium (30000×)

Figure 5 shows the microstructure of the sample hardened for 28 days after adding different calcium raw materials at a magnification of 30000 times. In the NH system, the surface of CGR is eroded and becomes a large number of cracks and flocculent or granular hydration products, which are concentrated on the surface of CGR. When 10% PC was added to NH system, the erosion of CGR was intensified, the surface zeolite phase was densely distributed, the network structure of hydration products was relatively compact, and the interface gap between unreacted particles and hydration products was large; When 5% $Ca(OH)_2$ is added to the NH system, the CGR particles basically all participate in the reaction, and the generated hydration products are fibrous at the reaction interface, which is conducive to interface bonding, and the hydration products form an interpenetrating network structure, which is more compact. It can be seen that $Ca(OH)_2$ is more conducive to the polymerization reaction of Ca^{2+} with active Si and Al.

3 Conclusion

$Ca(OH)_2$ has a significant promoting effect on the cementitious material. PC needs to be hydrated to generate $Ca(OH)_2$, which increases the alkali concentration of the reaction environment and releases Ca^{2+} to participate in the reaction. But $Ca(OH)_2$ can be directly dissolved in water and react with active Si and Al released from CGR to form C-S-H gel with low Ca/Si ratio. The addition of $Ca(OH)_2$ in AAMs promoted the formation of C-S-H gel and C-A-S-H gel, while the content of N-A-S-H gel decreased, the microstructure of cementitious materials became more compact, the pore structure and pore distribution were optimized, and the accelerating effect was more obvious.

Acknowledgement

References

I. Yoshitaka. (2012) "Utilization of coal gasification slag collected from IGCC as fine aggregate for concrete", in: Proceedings of the EUROCOALASH 2012 Conference, Thessaloniki, Greece, p. 1.

S. Fang, E.S.S. Lam, B. Li, et al. (2020) "Effect of alkali contents, moduli and curing time on engineering properties of alkali activated slag", Construct. Build. Mater, 249: 118799.

Tang, Z., Li, W.G., Hua, Y., et al. (2019) "Review on designs and properties of multifunctional alkali-activated materials (AAMs)", Constr. Build. Mater, 200:474–489.

The Effects of Supplementary Cementitious Materials on the Hydration Kinetics of G-Oil Cement

M. T. Palou[1, 2*], R. Novotný[3], E. Kuzielová[1,2], M. Žemlička[1], J. Čepčianska[1], J. Podhorská[1]

[1]Institute of Construction and Architecture, Slovak Academy of Sciences,
Dúbravská cesta 9, SK–845 03 Bratislava, Slovak Republic
[2]Faculty of Chemical and Food Technology, Slovak University of Technology
Radlinského 9, SK–812 37 Bratislava, Slovak Republic
[3]Materials Research Centre, Faculty of Chemistry, Brno University of Technology
Purkyňova 118, CZ–612 00 Brno, Czech Republic

*[*] martin.palou@savba.sk

ABSTRACT

The present study was undertaken to study the kinetics of the hydration reaction of G-Oil Well Cement and its blends by conduction calorimeter and thermogravimetric analysis. The coupling effect of temperature (25, 40, 50, 60, 80 °C) and material composition (100, 95, 90, 85, 80, 75, 70, 65 %) with different substitution levels by blast slag furnace, metakaolin, and limestone were analyzed on the light of hydration products and activation energy of different reactions. The apparent activation energies calculated from the hydration peaks characterizing the different reactions decrease with the increase in the substitution levels, but that of the second peaks (33.31 to 31.95 kJ°mol^{-1}) is higher than that of the former (31.33 to 27.88 kJ ° mol^{-1}) at the same level of substitution. Thermogravimetric analysis of the samples after calorimetric measurement shows that the main hydration products are C-S-H, C-A-S-H, CH, and calcium carbonate. Their quantity depends on the composition of the material and the temperatures.

KEYWORDS: *G-oil well cement, material composition, hydration, temperature, thermal analysis, kinetics*

1. Introduction

G-Oil Cement (GOWC) is a specific class of binders used mainly as zonal isolation materials during oil well cementing operations. Indeed, the cement slurry, primarily prepared at normal temperatures, is pumped through the steel casing to the bottom of the well and then up through the annulus between the casing and the surrounding rock (De Andrade and Sangesland (2016). The temperatures and vapor pressures increase with the well depth making cement slurry hydrating under different conditions, including hydrothermal ones. From the chemical point of view, C-S-H, ettringite, and CH are formed when the temperature does not exceed 110 °C. At different equilibrium temperature/pressure phases, C-S-H gradually changes its structure from semi-crystalline to crystalline one while ettringite is decomposed. The transformation of the C-S-H to α-C_2SH phase at a temperature exceeding 150 °C leads to the beginning of strength deterioration due to the change in pore structure (Jupe et (2006)). These changes continue with increasing temperature/pressure causing the transformation of a-C_2SH to $C_6S_5H_3$. Some products like $C_5S_2H_2$ and scawtite ($C_7S_6CH_2$,) to some extent are also formed (Kuzielová eet al.(2019)). Therefore, Supplementary Cementitious Materials (Blast furnace slag, silica fume, metakaolin, fly ash) are added, concomitantly or individually, to the commercial Oil-well cements to prevent this high-temperature transformation (Palou et al. (2014)). The main objective of the present work is to study the effect of Supplementary Cementitious Materials and temperatures on hydration heat and kinetics of G-Oil cement via conduction calorimeter and

thermal analysis to determine its suitability for developing heavyweight structure for application in the underground depository.

2. Experimental

The Class G-Oil Well Cement used in this study was manufactured by Dyckerhoff GmbH Hauptverwaltung, Germany. Granulated blast furnace slag (Kotouč Štramberk, spol. s r.o., Czech Republic); metakaolin (metakaolin L05 Mefisto from České lupkové závody, a.s., Czech Republic); and finely ground limestone (Calmit, spol. s.r.o., Slovakia) were used as Supplementary Cementitious Materials. Their oxide composition, surface area, and related mineralogical were reported by (Palou et al. (2014)).

2.1. *Material composition*

Table 1 shows the mix proportions of GOWC and Supplementary Cementitious Materials (Blast Furnace Slag-BFS, Metakaolin-MK, and finely ground limestone –LS). The replacement levels of GOWC by combining 3 SCMs were 0%, 5%, 10%, 15%, 20%, 25%, 30%, and 35% by mass, respectively.

Table 1 Mix composition of blends (wt. %).

	GOWC	BFS	Metakaolin	Limestone
GOWC100	100	0	0	0
GOWC95	95	5	0	0
GOWC90	90	10	0	0
GOWC85	85	10	5	0
GOWC80	80	10	5	5
GOWC75	75	15	5	5
GOWC70	70	15	5	10
GOWC65	65	15	5	15

The study of cement hydration kinetics in the temperature range of 25°C to 80°C was conducted using the conduction isothermal calorimeter to record the heat flow and determine the heat of G-oil well cement and its composites. By way of illustration, 5 coupled figures of heat flow and heat of hydration curves are presented to illustrate the influence of the material composition, to demonstrate the influence of different temperatures on each sample, and to calculate the „apparent activation energy. "

The hydration products of the samples after calorimetric measurement were analyzed by TGA/DSC technique (TGA/DSC-1, STARe software 9.30, Mettler Toledo). After having stopped hydration, 10.00 (± 0.03) mg of finely ground samples were heated in the open platinum crucibles until 1000 °C at the heating rate of 10 °C min^{-1} under an N_2 atmosphere.

3. Results and Discussion

3.1. Assessment of hydration of GOWC and its blends by conduction calorimetry

The heat flow and cumulated hydration heat during the first 48 h hydration of GOWC and its blends at different temperatures are depicted in Figs. 1. In general, three main exothermic peaks with four main stages (dissolution, induction, acceleration, and deceleration) can be observed at the curves of the hydration heat flow of all samples.

The first observed peak after the induction period is due to the hydration of C_3S, resulting from the nucleation and crystallization of C-S-H and CH. In addition, the second peak observed in the deceleration period is attributed to the second exothermic reaction related to C_3A (formation of ettringite after depletion of the protective layer or decomposition of AFt into AFm). Moreover, Fig. 1 (60°C and 90°C) of heat flow illustrates a phase of acceleration due to the alkali-activated reactions or the formation of monocarboaluminate $Ca_4Al_2(CO_3)(OH)_{12}.H_2O$ and hemicarboaluminate $Ca_4Al_2(CO_3)_{0.5}(OH)_{13}1.5H_2O$ due to the presence of limestone. Also, it can be observed that the total released hydration heat of blended

cements is lower than the reference one. Though the decrease of cumulative heat is related to the content of GOWC in mixtures, the difference between the overall heat of hydration tends to disappear with increasing hydration temperatures and converge towards the value of 325 j°g⁻¹. This fact could confirm that the alkali-activation reactions are more temperature-sensitive than the hydration of the reference GOWC.
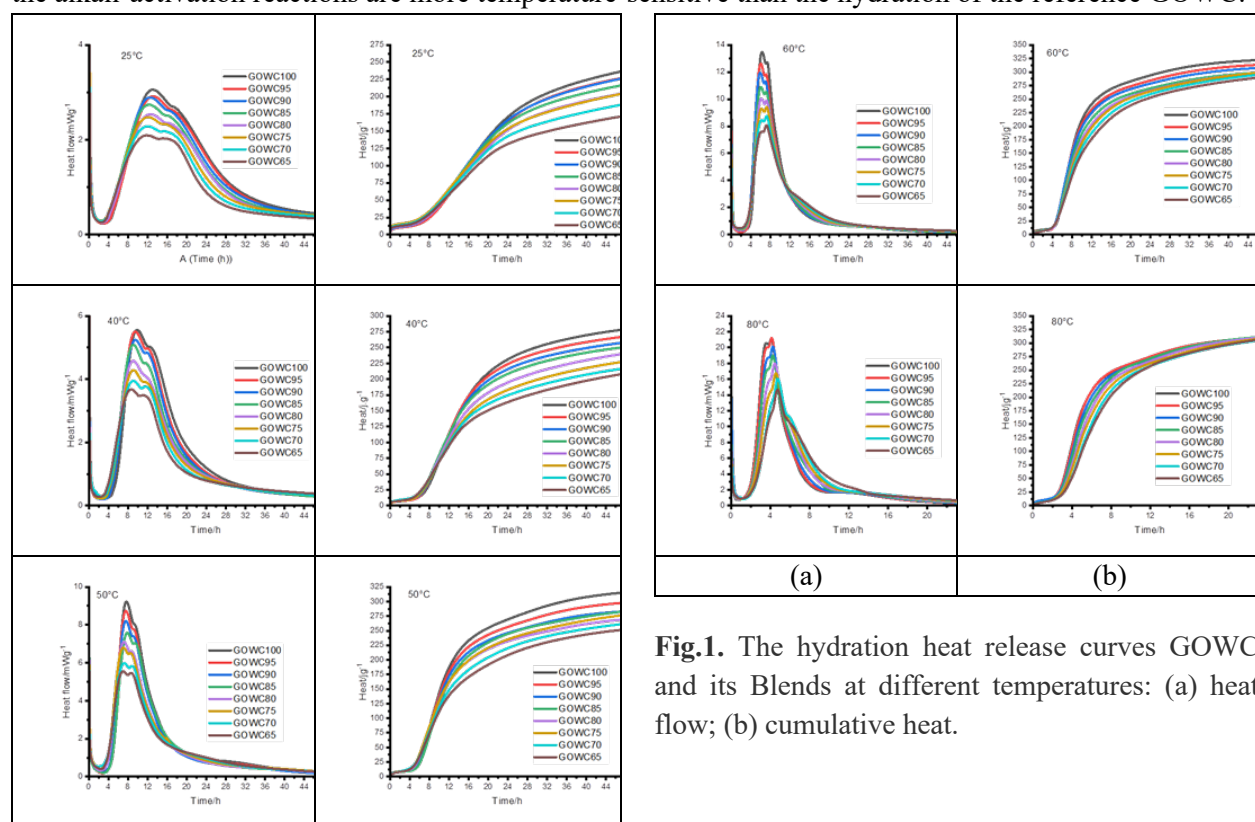
Fig.1. The hydration heat release curves GOWC and its Blends at different temperatures: (a) heat flow; (b) cumulative heat.

3.2. Apparent activation energy

Apparent activation energy using Arrhenius (Eq.1) general rule was calculated for each reaction represented by peaks at the curve of heat flow of hydration based on five different temperatures.

$$k(T) = A \exp\left(-\frac{E_a}{RT}\right) \tag{1}$$

where k is the temperature-sensitive rate or rate constant, A is a pre-exponential constant sometimes called the attempt frequency, and R is the ideal gas constant (8.314 J/(mol°K⁻¹); T is the absolute temperature (K); E_a is the activation energy (J°mol⁻¹).

Table 2 Values of E_a for each peak and samples

	Pre-exponential factor	First peak	Pre-exponential factor	Second peak
	A	E_a (kJ°mol⁻¹)	A	E_a (kJ°mol⁻¹)
GOWC100	13.79	31.33	14.46	33.31
GOWC95	13.74	31.29	14.47	33.40
GOWC90	13.36	30.41	14.18	32.72
GOWC85	12.86	29.25	14.02	32.46
GOWC80	12.81	29.35	14.04	32.70
GOWC75	12.34	28.25	13.73	31.99
GOWC70	12.24	28.22	13.66	31.98
GOWC65	12.03	27.88	13.57	31.95

The values of E_a (kJ°mol^{-1}) are reported in Table 2. They decrease with the degree of substitution, but the E_a of the second peak is higher than that of the first one. It indicates a relatively strong barrier to overcome for the second reaction of C_3A. Indeed, the formation of ettringite after the induction period requires the rearrangement of the gel structure surrounding the original minerals into crystal one before the penetration of water and dissolved ions to activate the reaction. Moreover, the presence of SCM-bearing aluminum compound (BFS, MK) contributes to the formation of ettringite and mainly under the temperature effects. Therefore, temperature becomes a key factor in increasing the second peak intensity.

3.3. Determination of hydration products by thermal analysis

The determination of hydration products is mainly based on the TG/DTG analysis at four temperature intervals. The dehydration of C–S–H, gypsum, and ettringite occurs at 100–140°C temperature, followed by thermal decomposition of C–A–S–H products at 140–420 °C, and then CH at 420–500 °C. 600–1000 °C corresponds to the decomposition of different carbonated calcium. Fig. 2 represents the effect of SCMs under two extreme temperatures (25 and 80 °C).

CH is released by the hydration of calcium silicate phases and consumed in the alkali-activated reaction and overall carbonation. The hydration products and their amount depend on material composition and curing temperatures. The formation of C–S–H is retarded at temperatures over 50°C, which supports the formation of C-A-S-H mainly in the presence of SCMs.
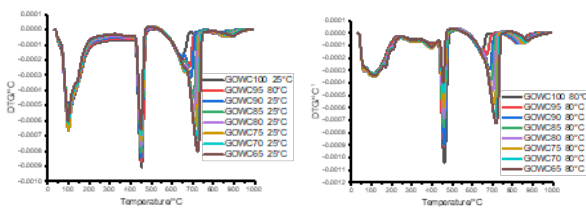
Fig. 2. Influence of material composition on DTG curves at 25°C and 80°C.

4. Conclusions

The conduction calorimeter assessing the hydration heat evolution at different temperatures has provided data for calculating the activation energy. Two main peaks, which intensities vary with material composition and temperature, represent the hydration reaction of the "silicate" and "aluminate" phases. Their apparent activation energy depends on material composition. The higher the substitution level, the lower the value of apparent activation energy. The 48-hour total heat evolved varies between 172 J°g^{-1} and 310 J°g^{-1}. Some blends can be considered as low heat cements for massive underground structures. The DTG figures provide a deep analysis of the decomposition and phase changes in the main cement hydrates in the temperature range of 0 to 1000°C. The hydration products are similar and stable at up to 80 °C at least.

References
De Andrade, J. and Sangesland, S. (2016) "Cement Sheath Failure Mechanisms: Numerical Estimates to Design for Long-Term Well Integrity", *Journal of Petroleum Science and Engineering*, 147:682–698

Boháč, M., Palou M.T., Novotný, R., Másilko, J., Všianský, D., Staněk, T (2014) "Investigation on early hydration of ternary Portland cement–blast–furnace slag–metakaolin blends," Construction and Building Materials (2014):64;333–341

Jupe, A.C., Wilkinson, A.P., Luke, K., Gary, P. And Funkhouser, G.P. (2008) "Class H cement hydration at 180 °C and high pressure in the presence of added silica ". Cement and Concrete Research, 38(5):660-666.

Kuzielová, E., Žemlička, M., Másilko, J., Palou, M.T. (2019) "Development of G-oil well cement phase composition during long therm hydrothermal curing". *Geothermics*, 80:129-37.

Palou, M.T., Šoukal F., Boháč. M., Šiler. P., Ifka, T. and Živica, V. (2014) "Performance of G-Oil Well cement exposed to elevated hydrothermal curing conditions", *Journal of Thermal Analysis and Calorimetry*, 118(2):865–74.

The 16th International Congress on the Chemistry of Cement 2023 (ICCC2023)
"Further Reduction of CO_2 -Emissions and Circularity in the Cement and Concrete Industry"
September 18–22, 2023, Bangkok, Thailand

Industrial Deployment of Calcined Clays Cements.

Néstor Isaías Quintero Mora[1*]

[1] *CEMEX, Monterrey, Mexico*

Email: nestorisaias.quintero@cemex.com

ABSTRACT

Cement is one of the most used materials in the world, and its production is classified as an energy intensive process that accounts for approximately 4% to 6% of all anthropogenic CO_2 emissions in the world. For many years the cement industry has strived to reduce its CO_2 emissions by substituting cement clinker by Supplementary Cementitious Materials (SCMs). This substitution is a frequent practice in the cement industry, and it includes the use of materials classified as by-products that fit into the cement production process, thus supporting the circular economy scenarios.

CEMEX promotes the use of these type of materials to continue reducing its CO_2 footprint thus contributing towards a carbon neutral world. Currently 30% of Cemex's CO_2 emission reduction goal vs. the 1990 baseline has been achieved and by 2030 it is expected to reach around 47%, which is approximately equivalent to 430 kg CO_2/ton c.

The present efforts aim to explore and improve the experience of manufacturing new SCMs such as calcined clays, in which diverse types of clays are thermally treated. Calcined clays have allowed Cemex to continue reducing the overall CO_2 footprint while maintaining the properties and performance of the cements. Industrialization of this process is essential to properly activate the ~~calcined~~ clays, so that it can be incorporated into the cement production resulting in reduced CO_2 emissions and making Cemex one of the industry leaders in its use.

KEYWORDS: *Calcined Clays, low carbon cements, CO_2 footprint.*

1. Introduction

Some clay minerals are potential candidates to be transformed into new supplementary cementitious materials or SCMs. They can partially replace Portland cement, and consequently enhance strength, improve durability, and reduce the CO2 emissions (Samet et al. 2007) associated with cement production.

In recent years, there has been a growing trend in thermal activation of clays due to their low cost and availability in many countries and as well because some clays achieve pozzolanic properties when thermally activated.

The pozzolanic activity is a result of a thermal activation of kaolinite and some other compounds present in the clays.

There is a distinct difference between metakaolin and other pozzolanic materials, such as fly ash and silica fume in the fact that metakaolin is a primary product obtained during a controlled process, while fly ash and silica fume are secondary products of other industrial processes.

As kaolinite is heated, the temperature leads to a loss of chemical water and consequently a phase transformation from kaolinite to an amorphous phase with high reaction ability, called metakaolin.

However, it has been found other compounds achieving good activation at different temperatures.

The 16th International Congress on the Chemistry of Cement 2023 (ICCC2023)
"Further Reduction of CO_2 -Emissions and Circularity in the Cement and Concrete Industry"
September 18–22, 2023, Bangkok, Thailand

Temperature, heating rate and time significantly influence producing thermally activated materials in a reactive state, which would be between 600° and 800°C. If temperature is too high inert crystalline phases will be formed.

The main characteristic of the produced calcined clay is its pozzolanic activity or its ability to react with calcium hydroxide (Thomas, 2013) to obtain compounds with cementitious properties.

This reaction forms additional cementitious CSH gel, together with crystalline products, which include calcium aluminate hydrate and alumina-silicate hydrates.

And finally, similar cementitious materials such as slag represent about 5%-10% of the amount of cement, which unlikely options to increase (Scrivener, 2018)

2. Objective

The main objective is to deploy the use of calcined clays at industrial scale using existing assets, and as well assuring that the material will maintain the characteristics evaluated at laboratory scale. For this purpose, a set of laboratory testing has been defined using different clay materials from selected location in Middle East, South America, and Central America. Finding the clay activation temperature is crucial, but as well to replicate the temperature control at a large-scale system is on e of the hardest topics to achieve.

3. Laboratory tests

Finding the right temperature and materials is crucial, therefore, to ensure full clay activation, we tested it at temperatures ranging from 500°C to 950°C.

Several tested materials reached close to 100% Activity Index. The Activity Index is measured by comparing the strength of a reference Ordinary Portland Cement (OPC/CEM I), versus a blended cement containing 70% OPC and 30% of a pozzolanic material, in this case calcined clay.
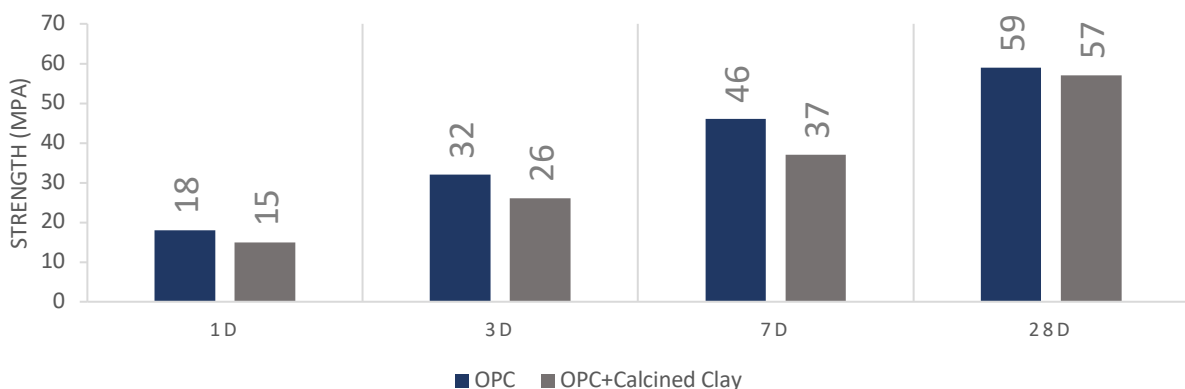
Fig. 1: Cement performance introducing calcined clays materials.

In table 1, some examples are shown of clays evaluated across Cemex and as can be seen, in many cases Kaolinite its main constituent. Traditionally research has found out that Kaolinite provides the reactivity to the calcined clay, however in other cases clays are a mixture of different compounds that can be activated as well such as illite containing materials, among others.

As shown in table 1, it is possible to have low kaolinite content and a high activity index, the most important factor is finding the right activation temperature.

Another important expect to observe is that the temperature for activation differs from one to another.

The 16th International Congress on the Chemistry of Cement 2023 (ICCC2023)
"Further Reduction of CO_2 -Emissions and Circularity in the Cement and Concrete Industry"
September 18–22, 2023, Bangkok, Thailand

Table 1. Activity Index vs. Kaolinite content.

Compound	Site 1	Site 2	Site 3	Site 4	Site 5
Kaolinite	78%	4%	65%	-	9%
Activity Index (AI)	110%	90%	90%	99%	88%

4. Industrialization

After testing at laboratory scale, a first Industrialization test was held in a location in the Middle east, where three different materials were tested: kaolin, clay and a mixture of clay and feldspar.

Testing Kaolin resulted in higher fuel consumption, higher CaO, and higher Loss of Ignition than expected. Concluding that the Kaolin pile was contaminated with limestone.

For the combination of clays, the strength result was not as high as what was obtained in the laboratory testing, but still was in a good range of 95%- 98% pozzolanic activity at 28 days, compared to 110% at laboratory scale.

For the second industrial test in South America, the main goal of was to enhance the existing pozzolanic activity at a temperature close to 800°C, reduce the cement clinker factor with replacement of the activated clays thus reducing CO_2 emission levels and to establish the main parameters and control variables to guarantee optimal results for clay activation in industrial tests.

This test was successful due to the ability to accomplish good stability at nominal kiln conditions and good quality of calcined clays. The plant was also able to successfully identify the new main control variables while also reducing fuel consumption.

As for the third set of trials in Central America plant, the goal was to produce an activated clay with pozzolanic activity by a calcination process in one of the wet kilns.

The main challenge was to evaporate the excess water and achieve the required temperatures for thermal activation of the clay

Table 2. Operating conditions optimization.

Description\ Plant	Middle East	Central America	South America
Materials	Kaolinite, mix of Clays + local Clay	Clay from the plant	Clay from the Plant
Kiln arrangement	Double preheater string with double calciner and bypass system	Wet kiln	Single string without calciner
Clay activation	In rotary kiln	In rotary kiln	In rotary kiln
Cooler	Grate	Grate	Rotary
Adaptations	• Material crushed	• Kiln speed decreased	• Material crushed
	• Dosing line to the kiln inlet	• Cooler grates and fans adjusted in case of dust production	• Preheater not used

The 16th International Congress on the Chemistry of Cement 2023 (ICCC2023)
"Further Reduction of CO_2 -Emissions and Circularity in the Cement and Concrete Industry"
September 18–22, 2023, Bangkok, Thailand

• Preheater not used	• Control of new process parameters vs temperature and expected AI	• Dosing line adapted to feed clay to the kiln inlet
• Kiln speed decreased & Cooler fans adjusted	• No color control	• Control of new process parameters vs temperature and expected AI
• No color control		• No color control
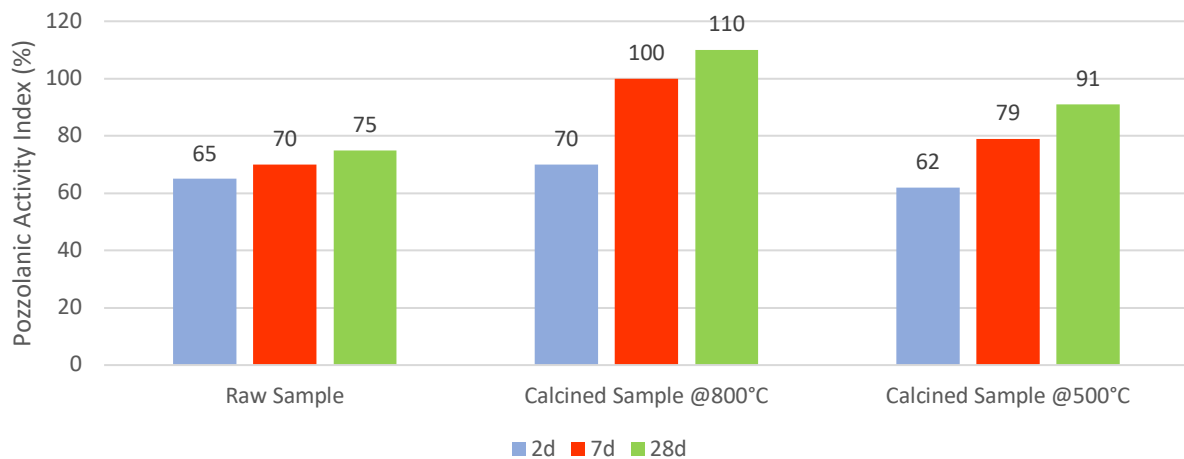
Fig. 2 Pozzolanic Activity Index of raw clay and calcined at different temperatures.

5. Conclusions

Operational conditions and temperature control are the key parameters, since it can drastically affect the quality of the material produced. As shown in Figure 2, the calcined sample that only reached 500°C, resulted in a significant loss of quality.

The quality of the calcined clay obtained at an industrial level is critical to make it suitable to replace the clinker content in cement production.

Calcined clay's ability to reduce cement's clinker factor can be a key element in Cemex's decarbonization strategy and goals.

6. References

[1] Samet B., Mnif, T., Chaabouni M. (2007). Use of a kaolinitic clay as a pozzolanic material for cements: Formulation of blended cement. *Cement and Concrete Composites*, 29(10) 741-749.

[2] Thomas, M., Jewell, R., & Jones, R. (2017). Coal fly ash as a pozzolan. *Coal Combustion Products*, pp 121-154.

[3] Scrivener, K., Martirena, F., Bishnoi, S. & Maity, S. (2018). Calcined clay limestone cements (LC3). *Cement and Concrete Research*, 114, pp 49-56

Use of machine learning for predicting phase assemblages of supplementary cementitious materials-blended cements

A.B. Degefa[1*], H.K. Yoon[2], J.Y. Bak[3] and S. Park[4]

[1] *Department of Civil Engineering, Pukyong National University, 45 Yongso-ro, Nam-gu, Busan 48513, Republic of Korea*

Email: aaronpknu@pukyong.ac.kr

[2] *Department of Artificial Intelligence, Sungkyunkwan University, 25-2 Sungkyunkwan-ro, Jongno-gu, Seoul, Republic of Korea*

Email: hkyoon95@g.skku.edu

[3] *Department of Artificial Intelligence, Sungkyunkwan University, 25-2 Sungkyunkwan-ro, Jongno-gu, Seoul, Republic of Korea*

Email: jy.bak@skku.edu

[4] *Department of Civil Engineering, Pukyong National University, 45 Yongso-ro, Nam-gu, Busan 48513, Republic of Korea*
Email: solmoi.park@pknu.ac.kr

ABSTRACT

The role of supplementary cementitious materials (SCMs) in reducing CO$_2$ emissions by lowering the clinker content is becoming invaluable. As such, developing a tool to predict the major properties of SCMs can be a significant step toward ensuring their effective use in hydrated Portland cement. In this research, the major hydration products of SCM-blended cements are predicted using artificial neural network (ANN) machine learning (ML) by employing different input data which are easily adaptable for a wide range of SCMs. The prediction results show that the model has a root mean squared logarithmic error of 0.6 on average. The model's applicability is tested for the current two most frequently utilized SCMs, namely fly ash and metakaolin by predicting the phase assemblages and investigating their correlations to oxide composition. The findings indicate that ML models can be utilized efficiently to predict phases of SCM-blended cements while also ensuring the better design of SCM addition.

KEYWORDS: *Portland cement; Machine learning; Supplementary cementitious materials; Phase assemblage*

1. Introduction

The cement industry frequently uses supplementary cementitious materials (SCMs) to mitigate significant carbon dioxide emissions caused by Portland cement (PC) production. These materials have been extensively researched and are considered a foundation for future projects. With a wealth of accumulated data available, machine learning can be utilized to predict multiple sets of SCM attributes.

The microstructural evolution of PC with SCMs involves a thorough investigation of the major stable phases formed during the hydration process. These include C-(A)-S-H, portlandite, monosulfate (monocarbonate), ettringite, hydrogarnet, hydrotalcite, and stratlingite. Accurately forecasting these phases would benefit the optimization of concrete mixture preparation and the prediction of hardened concrete characteristics. Various techniques have been utilized in predicting these phases, such as Nuclear magnetic resonance (NMR) spectroscopy, scanning electron microscopy/backscattered electron image analysis

17

coupled with energy dispersive spectroscopy (SEM-EDS/BSE-EDS), quantitative X-ray diffractometry (QXRD), and X-ray computed tomography (CT). Although the aforementioned techniques generally provide reliable results, they do have limitations. For instance, NMR has limited sensitivity, especially for isotopes with low natural abundance, and requires a certain level of expertise to execute experiments and interpret spectra accurately. Additionally, the presence of paramagnetic species, such as Fe in PC and fly ash, can alter the relaxation and chemical shift of adjacent nuclear spins, which can affect the characterization process (Walkley and Provis, 2019). SEM-EDS/BSE-EDS requires a large number of photos to obtain quantitative data and is heavily reliant on experience, which can lead to issues with grey value overlapping (Scrivener, 2004). QXRD may also encounter issues related to overlapping contributions from amorphous SCM products and C-S-H. Furthermore, due to the diversity of refining procedures and techniques used, reproducibility of findings between labs may be challenging (Soin et al., 2013). Lastly, CT's ability to deliver spatial resolution that provides equal grey scale values for distinct solid phases in the reconstructed image volume is limited (Deboodt et al., 2021).

Machine learning (ML) approaches can be employed to overcome challenges in identifying phases in hydrated SCM-blended cements. In this study, a machine learning model was developed to predict which solid phases of SCMs will form based on basic information about the materials. An artificial neural network (ANN)-based ML system was used due to its ability to generate reliable predictions from existing data. The findings of this study reveal that the predictions are strongly correlated with past experimental results and observations.

2. Methods

The data collected was made of 254 observations, 24 independent variables, and the hydrated PC-SCM phase outputs as a dependent variable. Inputs included oxide composition of PC and SCMs (SiO_2, Al_2O_3, Fe_2O_3, CaO, MgO, SO_3, Na_2O, and K_2O), the water-to-cement ratio ranging from 0.25-0.8, the proportion of binder materials (PC/SCM), curing temperature ranging from 10-50 ^{0}C, curing time ranging from 3-1000 days, particle size, surface area, specific gravity and the phase outputs.

In this study, a dataset was used to train and test an ANN ML algorithm. The dataset was randomly split into 80:20 training and test groups. The ANN had a basic three-layer structure with an input layer, a hidden layer, and an output layer. The input layer accepted numerous input characteristics, and the hidden layer utilized activation functions such as relu, abs, sigmoid, and softplus to introduce nonlinearity to the model and identify appropriate weights and biases. The best activation functions were found to be softplus and abs, and the dataset was divided into five parts for analysis, with the testset outcomes averaged across each partition. The study focused on the hydrated phase assemblage of PC-SCMs obtained from the ML predictions, and phase diagrams were constructed based on the SCMs' dominant oxide composition. Throughout the paper, the curing time and water-to-cement ratio were kept constant at 90 days and 0.4, respectively.

3. Results and discussion

3.1 Phase assemblage of hydrated PC with SCM

The effect of SCM replacement on the phase assemblage of hydrated cement for replacement values of 0,13,26,39,52, and 65 is described in this section. Figure 1 depicts the phase outputs of the model for metakaolin blended PC. The consumption of portlandite increases with metakaolin content. Up until 52% metakaolin substitution, the quantity of C-(A)-S-H formed rises; after that point, it starts to decline slightly; however, it still accounts for more than 50% of the available phases. Hydrogarnet stability decline towards cement and metakaolin-dominant compositions. Additionally, the greater alumina and silica concentration of metakaolin makes C-A-S-H formation easier in PC-metakaolin (Zhao and Khoshnazar, 2020). Monosulfate and hydrotalcite are found in small amounts and increase with metakaolin substitution. The concentration of ettringite is extremely low, at around less than 1%. Furthermore, the increase in metakaolin replacement results in more free water. Briki et al. (Briki et al., 2021) reported similar variations in phase assemblage for portlandite, monosulfate, and free water.
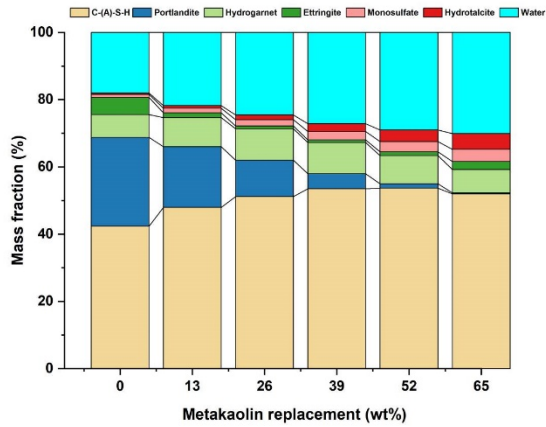
Figure 1 The effect of metakaolin replacement on the phase composition of hydrated PC at different concentrations
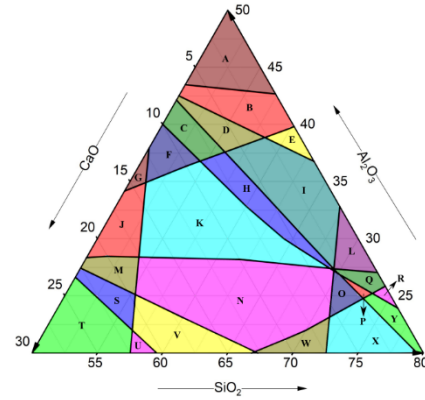
Figure 2 Phase assemblage output in CaO-SiO₂-Al₂O₃ composition for 25% fly ash replacement in hydrated PC

Table 1 Description of the regions shown in Figures 2. 'a' and 's' represent abundant and scarce solid phases, respectively.

Region	Predicted phase output					
	C-(A)-S-H	Portlandite	Ettringite	Monosulfate	Hydrogarnet	Hydrotalcite
A	s	s	s	-	a	s
B	s	s	s	-	-	s
C	s	s	s	-	-	-
D	-	s	s	-	-	s
E	-	s	-	-	-	s
F	-	-	s	-	-	-
G	-	-	s	s	-	-
H	-	s	-	-	-	-
I	-	s	-	-	-	s
J	-	-	-	s	-	-
K	-	-	-	-	-	-
L	-	s	-	a	-	s
M	-	-	-	s	s	-
N	-	-	-	-	s	-
O	-	-	-	a	s	-
P	-	-	-	a	s	s
Q	-	s	-	a	s	s
R	-	s	a	a	s	s
S	a	-	-	s	s	-
T	a	a	-	s	s	a
U	a	a	-	-	s	a
V	a	-	-	-	s	-
W	-	-	a	-	s	-
X	-	-	a	a	s	-
Y	-	-	a	a	s	s

3.2 Phase diagrams based on dominant oxide composition

This section describes the influence of the main oxide compositions on the phase formation of the PC-SCM hydrated system. To illustrate this, the ternary diagrams demonstrate the concentrations of solid phases for a 25% fly ash substitution in hydrated PC, based on the main oxides (CaO-SiO₂-Al₂O₃) in the PC-fly ash system. The major oxide ranges are established using the quantity of fly ash present in the PC-SCM combined environment, while the other oxides are kept constant. Once the ranges are determined, solid

phases that are abundant and scarce are designated as those that represent >75% and 25% of the difference between the maximum and lowest solid-phase masses, respectively, using the oxide composition range.

Figure 2 depicts the CaO-SiO_2-Al_2O_3 ternary phase diagram for 25% fly ash substitution. The percentage ranges of the main oxides are $0 \leq CaO \leq 30$, $50 \leq SiO_2 \leq 80$, and $20 \leq Al_2O_3 \leq 50$. While it is reasonable to assume that SiO_2 composition has a major role in determining hydrated PC-fly ash phase stability, the explanations that follow focus on oxide composition variations occurring within the ranges specified. For example, CaO-dominated oxide composition indicates ($CaO=30\%$, $SiO2=50\%$, and $Al2O3=20$). The amount of C-(A)-S-H solid phase is largely determined by the concentration of CaO, with its formation being significantly promoted by higher CaO concentrations (Walkley et al., 2016). The highest concentrations of C-(A)-S-H solid phase can be expected to precipitate when ($CaO/(CaO+SiO_2+Al_2O_3) > 0.2$). Portlandite and hydrotalcite also prefer CaO-dominated environments, remaining stable when ($CaO/(CaO+SiO_2+Al_2O_3) > 0.24$). The consumption of Portlandite is highly facilitated for increased concentrations of Al_2O_3. Ettringite and monosulfate are stable in SiO_2-dominated compositions. However, ettringite becomes highly unstable in Al_2O_3-dominated compositions, while monosulfate becomes unstable in CaO-dominated compositions. Lastly, Al_2O_3-dominated compositions promote the formation of hydrogarnet.

4. Conclusions

The aim of this research was to create and analyze a model that can predict the primary phases of hydrated SCM-blended cements. The study examined the phase assemblage output and the impact of oxide composition on the development of these phases in hydrated PC-SCMs. The model's phase outputs demonstrate how the PC-SCM can be enhanced to produce the necessary phase output. Additionally, precise design of SCM additions can be achieved by calculating the stability fields of the primary phases in the hydrated PC-SCM system based on the oxide composition of the SCMs. In the case of PC-fly ash, for instance, C-(A)-S-H, portlandite, and hydrotalcite outputs were improved by adding extra amounts of CaO, while ettringite and monosulfate were enhanced by using additional amounts of SiO_2.

References

Briki, Y., Avet, F., Zajac, M., Bowen, P., Haha, M. Ben, and Scrivener, K. (2021). Understanding of the factors slowing down metakaolin reaction in limestone calcined clay cement (LC3) at late ages: *Cement and Concrete Research*, Vol. 146, No. October 2020, p. 106477, DOI: 10.1016/j.cemconres.2021.106477.

Deboodt, T., Wildenschild, D., Ideker, J.H., and Burkan Isgor, O. (2021). Comparison of thresholding techniques for quantifying portland cement hydrates using synchrotron microtomography: *Construction and Building Materials*, Vol. 266, p. 121109, DOI: 10.1016/j.conbuildmat.2020.121109.

Scrivener, K.L. (2004). Backscattered electron imaging of cementitious microstructures: Understanding and quantification: *Cement and Concrete Composites*, Vol. 26, No. 8, pp. 935–945, DOI: 10.1016/j.cemconcomp.2004.02.029.

Soin, A. V., Catalan, L.J.J., and Kinrade, S.D. (2013). A combined QXRD/TG method to quantify the phase composition of hydrated Portland cements: *Cement and Concrete Research*, Vol. 48, pp. 17–24, DOI: 10.1016/j.cemconres.2013.02.007.

Walkley, B., and Provis, J.L. (2019). Solid-state nuclear magnetic resonance spectroscopy of cements: *Materials Today Advances*, Vol. 1, DOI: 10.1016/j.mtadv.2019.100007.

Walkley, B., San Nicolas, R., Sani, M.A., Rees, G.J., Hanna, J. V., van Deventer, J.S.J., and Provis, J.L. (2016). Phase evolution of C-(N)-A-S-H/N-A-S-H gel blends investigated via alkali-activation of synthetic calcium aluminosilicate precursors: *Cement and Concrete Research*, Vol. 89, pp. 120–135, DOI: 10.1016/j.cemconres.2016.08.010.

Zhao, D., and Khoshnazar, R. (2020). Microstructure of cement paste incorporating high volume of low-grade metakaolin: *Cement and Concrete Composites*, Vol. 106, DOI: 10.1016/j.cemconcomp.2019.103453.

Comparison of superabsorbent polymer characterization by filtration test in water and cementitious filtrate

L.F.M. Souza[1*], M.A.R.Fontes[2], and L.B.Agostinho[3]

[1] *Federal University of Uberlândia, Uberlândia, Brazil*
Email: luiza.f.souza@ufu.br
[2] *Federal University of Uberlândia, Uberlândia, Brazil*
Email: matheus.abdala@ufu.br
[3] *Federal University of Uberlândia, Uberlândia, Brazil*
Email: liviaborba@ufu.br

ABSTRACT

The use of internal curing (IC) has been a strategy to mitigate autogenous shrinkage in high performance concretes (HPC). Superabsorbent polymers (SAP) are one of these techniques, as they can retain water, and by osmotic pressure, release it during the cement hydration. They can reduce the autogenous shrinkage by reducing capillary pressure, as they replace the water in the matrix as it is consumed by the reaction. Therefore, reduce meniscus, reducing possible cracks. However, SAP desorption, leave voids in the concrete, potentially damaging its mechanical properties. Thus, the measuring and determination of SAP absorption and desorption behavior is necessary to be well implemented in cementitious materials. There are many tests for it, but not all of them are normalized, so, a detailed analysis of these tests is needed for a better researchers networking of data and standardization of the methods. This study has the objective to contribute to this, by comparing the methodology and results of the filtration test in two different liquids: tap water and cementitious filtrate. It was verified that the environment slightly interferes in the results. This fact shows that SAP mechanisms depends on the surroundings, in other words, the polymer is sensitive, so, your absorption and desorption can change in order to its atmosphere. Therefore, for an optimized concrete, mortar or paste design containing SAP, it is necessary the knowledge of how much their cement slurry will change its potential. Then, the right design for each situation will be determined, searching the maximization of the polymer potential and minimization of its disadvantages on the matrix.

KEYWORDS: *Superabsorbent polymer, autogenous shrinkage, internal curing, cementitious materials, supplementary cementitious materials.*

1. Introduction

High performance concretes (HPC) suffers from autogenous shrinkage due to their low water-cement ratio (w/c), addition of supplementary cementitious materials (SCM), and high cement consumption (Jensen and Hansen, 2001). This leads to self-desiccation and can affect the mechanical properties of these concretes. Internal curing by SAP is one strategy to mitigate these effects, so proper dosage depends on proper characterization of the polymer, including its sorptivity. This property can change depending on the composition and as well as the properties of the sorbed fluid (Snoeck *et al*., 2018). Therefore, three test methods were evaluated in this work: filtration test, mainly using RILEM TC 260-RSC (Snoeck *et al*., 2018). Some procedures were modified to simplify the method and evaluate its impact on the reliability of the results.

2. Methodology

The SAP used in this work is a covalently crosslinked acrylamide/acrylic acid polymer prepared by suspension polymerization with spherical particles, and average diameter of 100 μm. The amount of dry SAP for this test should also be determined in advance by a dummy test in the liquid to be used to ensure that there is sufficient liquid to be freely swollen by the polymer. This amount must be weighed to an

accuracy of 0.001 g. In this work, this amount was 0.050 g in 100 g of fluid analyzed in two ways: tap water and cement-based solution. The latter was prepared by a filtrate of cement slurry with a w/c of 5 (Mechtcherine *et al.*, 2018a). This solution aims to achieve a pH environment close to that of the cementitious materials. Two mixing methods have been used, in the literature for this purpose: 45 minutes of decantation (Wehbe and Ghahremaninezhad, 2017) and 24 hours of automatic stirring followed by filtration (Snoeck, Pel and De Belie, 2017)(Zhao, Jensen and Hasholt, 2020). Both were used in this study to compare their effects on SAP absorption. The dry polymers were then immersed in the liquids, and after 1, 5, 10, 30, 60 minutes, 3, and 24 hours, the entire solution was filtered and its mass weighed. Between these intervals, the beakers were sealed to prevent carbonation. Three samples were taken for each liquid. Equation (1) determines the SAP sorption (*SC*).

$$SC = \frac{m_{fluid} - m_{filtered}}{m_{SAP}} \tag{1}$$

The recommendation states that the filter paper should be saturated with the test liquid before filtration to avoid influencing the results. In this work are two groups of samples, one following this recommedation and another using a procedure similar to the tea bag test, as described in the same recommendation. The dry and wet masses of ten filter papers were recorded, and the average amount of absorbed water was used to exclude its influence on the results. Then, dry paper filters were used for the filtration experiments, and the results were adjusted according to the average amount of absorbed water on the previously obtained tissue. For comparison, a tea bag test was also performed, but only with tap water, according to the RILEM recommendation.

3. Results and Discussion

The filtration test in cement slurry showed that there is no difference between the two types of mixtures, as the two tests are very similar, being a complementary result to (Zhao, Jensen and Hasholt, 2020). Which compared the absorption evolution of SAP in cement slurry filtrate under different convection conditions and despite their differences, all measurements gave approximately the same 24-hour absorption capacity. In the present study, the obtained absorbance after 24 hours was the same for both methods namely 662 g/g. Figure 1(a) shows the comparison between the filtration tests with tap water and cement slurry filtrate, each with pre-wetted paper filters (wet filtration) and non-pre-wetted paper filters (dry filtration), and the tea bag test with tap water. First, the significant difference in results between dry and wet filtration in both tested liquids is noticeable, as shown in Figure 1(b). This invalidates the proposed procedure, which is different from the RILEM recommendation for the filtration test. In tap water, this difference increased with the time of the measurement, with a higher value of 119% after 24 hours of absorption. In cement slurry filtrate, this difference increased with time until 1-hour absorption (282%) and then decreased until 24-hour absorption.
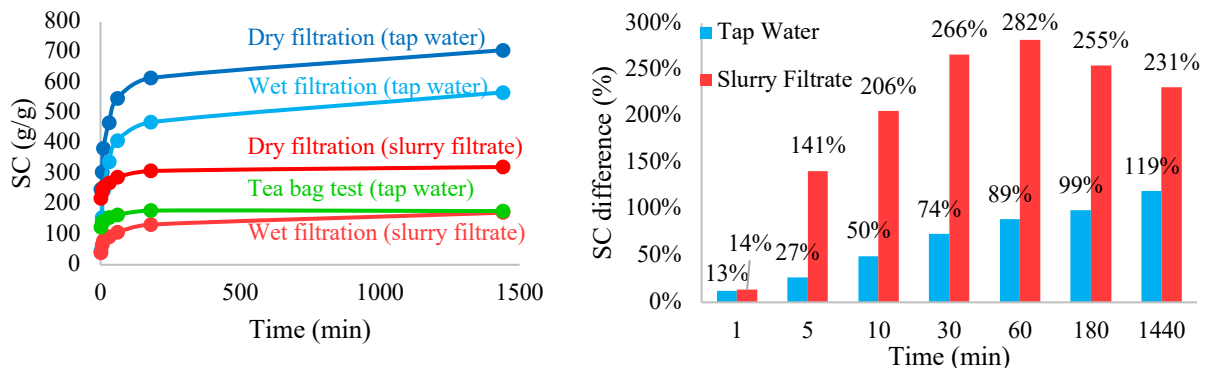
Figure 1 – (a) Comparison of SAP absorption in filtration test in tap water (blue lines), filtration test in cement slurry filtrate (red and pink lines) and tea bag test in tap water (green line), (b) Dry and wet filtration percentual different in SC values, in each measurement time

At 1 minute of liquid-polymer contact, the SAP absorption in cement slurry filtrate was 82% smaller than its value in tap water in both dry and wet filtration, as shown in Figure 2. Whereas in any other time, the difference between tap water and cement slurry filtrate absorption were higher in wet filtration. The higher difference between the two filtrations (wet and dry) was 38%, at 30-minute absorption. This difference between the two liquids decreases with time in both filtrations. From an absorption of 3 hours, it begins to stabilize, reaching values of 20% for dry filtration and 47% for wet filtration. This is different from the literature; Yuanliang *et al.* (2022) conducted filtration tests of cross-linked poly sodium acrylate SAP with deionized water and foam concrete pore solution and found a decrease in absorption in water to 80% on average after 24 hours, while this rate was 52% after 1 minute. Snoeck *et al.* (2016) also did this with demineralized water and cement filtrate in cross-linked potassium salt polyacrylate with average diameter of 475 μm, but only measured at a contact time of 5 minutes and a found an 80% decrease from water to cement filtrate liquid, which approximates to the wet filtration values of this work at the same time. Chidiac *et al.* (2021) used distilled water and cement slurry filtrate (w/c=10) for the filtration test in polyacrylate SAP with average diameter of 125 μm and came up with a decrease of 79%, close to the obtained values in wet filtration of this work, at 1 and 5-minute measurements.
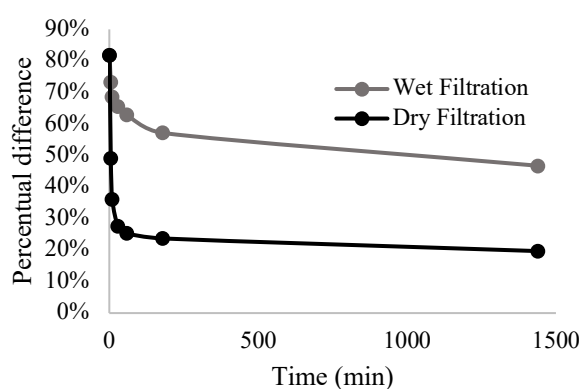
Figure 2 – Absorption in tap water and cement slurry filtrate percentual difference, in wet filtration (grey line) and dry filtration (black line)

In the tea bag test, an increase of 44% in the absorption of SAP is observed with water contact between 1 minute and 24 hours. Absorption measured in the filtration test with water increased by 47% for wet filtration and 186% for dry filtration between 1 minute and 24 hours. Comparing the values of the tea bag with the study of Mechtcherine *et al.* (2018) performed with cross-linked poly(acrylate-co-acrylamide) SAP with diameters above 200 μm in demineralized water, the absorption of SAP was in the range of 250-400 g/g, which is slightly different from the present work that reached a range of 120-200 g/g in tap water. Thus, it is clear that the substitution of the saturation of the paper filters with the test liquids by their previous weighing to estimate the water absorbed by them was not fully approved. The absorption SAP measured by the dry filtration test in both liquids showed much higher values compared to those reported in the literature. Zhong *et al.* (2019) tested different SAPs with different chemical structures in deionized water and cement slurry filtrate (w/c=5). They found absorption values between 200-400 g/g when water and SAP were in contact for 24 hours. While dry filtration in the present study gave a value of 707 g/g.

The SAP main driving force of swelling is osmotic pressure, which is proportional to the concentration of ions in the aqueous solution (Mechtcherine and Reinhardt, 2012). Tan and He (2022) have demonstrated that the absorption of SAP is higher in pure water than in tap water, because the latter has a higher ion concentration. Therefore, the values of this work in the filtration test in tap water were expected to be lower than those of Zhong *et al.* (2019), in deionized water. This was in the range of 150-400 g/g, which matches the range of wet filtration from this work (200-350 g/g) and does not match the values of dry filtration (250-710 g/g).The same discrepancy was observed in the slurry filtrate; while the cited work found values in a range of 5-25 g/g, the present study reached 568 g/g for dry filtration and 172 g/g for wet filtration in the 24-hour measurement. However, even if the values are consistent with the literature, a range of 5-20 g/g is also reported in the literature for use in concrete (Zhong *et al.*, 2021)(Palma e Silva *et al.*, 2022). Therefore, if no additional water is used, these methods are not so relevant.

3. Conclusions

The main conclusions found in this work can be summarized as follows:

(1) Using dry paper filters, even with the correction applied in this study, need to be more tested and explored to comprovate its efficienty on replacing the Recommendation procedure, by saturating them before the tests.

(2) In a cementitious filtrate, the absorption rate of SAP decreases. Even with the gap in the dry filtration test, this work could show this difference between the two liquids.

(3) The different methods to obtain the cement slurry did not seam to interfear at the absorption behaviour of the type of SAP used at this present work.

(4) Further reasearches with SAP need to be done to evaluate its sorption behaviour in concrete environment, to enable future optimizations of cementitious materials with SAP in their dosage.

References

Chidiac, S.E. *et al.* (2021) 'Efficiency measure of SAP as internal curing for cement using NMR & MRI', *Construction and Building Materials*, 278, p. 122365. Available at: https://doi.org/https://doi.org/10.1016/j.conbuildmat.2021.122365.

Jensen, O.M. and Hansen, P.F. (2001) 'Water-entrained cement-based materials: I. Principles and theoretical background', *Cement and Concrete Research*, 31(4), pp. 647–654. Available at: https://doi.org/https://doi.org/10.1016/S0008-8846(01)00463-X.

Mechtcherine, V. *et al.* (2018a) 'Testing superabsorbent polymer (SAP) sorption properties prior to implementation in concrete: results of a RILEM Round-Robin Test', *Materials and Structures/Materiaux et Constructions*, 51(1). Available at: https://doi.org/10.1617/s11527-018-1149-4.

Mechtcherine, V. *et al.* (2018b) 'Testing superabsorbent polymer (SAP) sorption properties prior to implementation in concrete: results of a RILEM Round-Robin Test', *Materials and Structures/Materiaux et Constructions*, 51(28). Available at: https://doi.org/10.1617/s11527-018-1149-4.

Mechtcherine, V. and Reinhardt, H.W. (2012) *Application of superabsorbent Polymers (SAP) in Concrete Construction*, *Springer*.

Palma e Silva, A.A. *et al.* (2022) 'Evaluation of mechanical properties and microstructure of high-performance mortars with superabsorbent polymers and metakaolin by means of X-ray computed microtomography', *Journal of Building Engineering*, 51(February). Available at: https://doi.org/10.1016/j.jobe.2022.104219.

Snoeck, D. *et al.* (2016) 'X-ray computed microtomography to study autogenous healing of cementitious materials promoted by superabsorbent polymers', *Cement and Concrete Composites*, 65, pp. 83–93. Available at: https://doi.org/https://doi.org/10.1016/j.cemconcomp.2015.10.016.

Snoeck, D., Pel, L. and De Belie, N. (2017) 'The water kinetics of superabsorbent polymers during cement hydration and internal curing visualized and studied by NMR', *Scientific Reports*, 7(1). Available at: https://doi.org/10.1038/s41598-017-10306-0.

Snoeck, D., Schröfl, C. and Mechtcherine, V. (2018a) 'Recommendation of RILEM TC 260-RSC: testing sorption by superabsorbent polymers (SAP) prior to implementation in cement-based materials', *Materials and Structures/Materiaux et Constructions*, 51(5). Available at: https://doi.org/10.1617/s11527-018-1242-8.

Snoeck, D., Schröfl, C. and Mechtcherine, V. (2018b) 'Recommendation of RILEM TC 260-RSC: testing sorption by superabsorbent polymers (SAP) prior to implementation in cement-based materials', *Materials and Structures/Materiaux et Constructions*, 51(116). Available at: https://doi.org/10.1617/s11527-018-1242-8.

Tan, Y., Chen, H. and He, R. (2022) 'Water distribution and transport-kinetics model in fresh cement-based mixtures containing superabsorbent polymers based on 1H low-field NMR', *Cement and Concrete Composites*, 127, p. 104396. Available at: https://doi.org/https://doi.org/10.1016/j.cemconcomp.2021.104396.

Wehbe, Y. and Ghahremaninezhad, A. (2017) 'Combined effect of shrinkage reducing admixtures (SRA) and superabsorbent polymers (SAP) on the autogenous shrinkage, hydration and properties of cementitious materials', *Construction and Building Materials*, 138, pp. 151–162. Available at: https://doi.org/https://doi.org/10.1016/j.conbuildmat.2016.12.206.

Yuanliang, X. *et al.* (2022) 'Effect of superabsorbent polymer on the foam-stability of foamed concrete', *Cement and Concrete Composites*, 127, p. 104398. Available at: https://doi.org/10.1016/j.cemconcomp.2021.104398.

Zhao, S., Jensen, O.M. and Hasholt, M.T. (2020) 'Measuring absorption of superabsorbent polymers in cementitious environments', *Materials and Structures/Materiaux et Constructions*, 53(11). Available at: https://doi.org/10.1617/s11527-020-1442-x.

Zhong, P. *et al.* (2019) 'Internal curing with superabsorbent polymers of different chemical structures', *Cement and Concrete Research*, 123, p. 105789. Available at: https://doi.org/https://doi.org/10.1016/j.cemconres.2019.105789.

Zhong, P. *et al.* (2021) 'Mechanisms of internal curing water release from retentive and non-retentive superabsorbent polymers in cement paste', *Cement and Concrete Research*, 147, p. 106494. Available at: https://doi.org/https://doi.org/10.1016/j.cemconres.2021.106494.

Multi-phase and Multi-ion Modelling of Electric Current, Electric Potential and Species Transport in Reinforced Concrete During Active corrosion Process Applied to Optimization of a Patching Repair Process

K. Szyszkiewicz-Warzecha

AGH University of Science and Technology, Faculty of Materials Science and Ceramics, Kraków, Poland
email: szyszkin@agh.edu.pl

ABSTRACT

Corrosion of the reinforcement bars in concrete constructions is one of the most important factor affecting their safety and useful lifetime. Due to the enormous scale of global usage of reinforced concrete, the problem of dealing with this degradative phenomenon is very important. Hence, the proper modelling of corrosion phenomena in reinforced concrete structures is crucial for the implementation of efficient corrosion control based on a good understanding of the underlying processes. A 3D corrosion model of reinforced concrete structures based on the Nernst–Planck flux for ionic species is presented and its application to cathodic protection with sacrificial anode (SACP) and patch repair aftereffects is demonstrated. Example of computing the optimal placement of the anode is included.

1. Introduction

During the service time of concrete structures, especially bridges, dams, roads, or parking garages, one repair technique is particularly frequently applied – the patch repair, where a part of defective or contaminated concrete cover of rebars is replaced with a fresh "patch". For example, if the contaminated concrete cover contains a high concentration of chlorides it is possible that the protective passive film on the rebar surface will break down, and in consequence the corrosion processes on the rebar surface will commence [1]. Hence, the patch is meant to reduce that risk by replacing the contaminated portion of concrete with fresh one which is free of chlorides. However, concerning the performance of repair it has been noted that recurring corrosion after patch repair is possible. To emend the effectiveness of repair, a sacrificial anode embedded into the concrete can be used. [2] The material of the anode is a less noble metal, such as zinc or magnesium, which corrodes more readily than the iron based rebar. However, the effectiveness of this method is not well understood and relatively little work on this topic is found in the literature. Relevant questions include the location and size of the anode and the influence of other ions on the electric current distributions. The main goal of this paper is to investigate the change of macrocell corrosion after patch repair. The study is based on a 3D model comprising electric potential, current density, flow of ions and heterogeneous redox reactions on the rebars surface. More specifically, the model involves transport of four components (O_2, Zn^{2+}, OH^-, Fe^{2+}), kinetics of electrode processes similar to the Butler–Volmer equation with concentration polarization. Numerical simulations based on this model evaluate the intensity of corrosion before and after repair and for various locations of the sacrificial anode. Additional, two cases are also considered: the cathodic protection with applied negative potential to the rebar (impressed current cathodic protection) and without applied potential. This approach is very helpful as experimental assessment for many possible cases of the patch and/or anode arrangements would be very costly, impractical or simply not feasible.

2. Description of the mathematical model

A schematic picture of a typical patch repair is shown in Figure 1. We assume that a central part (yellow block) is the patch which replaced a contaminated part around the cylindrical rebar. Moreover, the zinc

anode in the form of a small cylinder (pink color) is placed in the patch some distance away from the rebar. Two situations before repair are considered: (i) the middle (approx. one third length) of the rebar is in an active corrosion state and the rest surface is in a passive state; (ii) the middle of the rebar is in passive state and the rest surface is in an active state.

In dilute electrolytic solutions without convective flows, the flux of each dissolved species $(i = O_2, Zn^{2+}, OH^-, Fe^{2+})$ is given by [3]

$$\mathbf{J}_i = -D_i \nabla c_i - z_i u_i c_i \nabla \varphi \tag{1}$$

The flux $\mathbf{J}_i \, (\mathrm{mol}/\mathrm{m}^2 \cdot \mathrm{s})$ of species i is a vector describing the direction of species movement and its intensity. The flux of species i expressed in equation (1) is composed of two parts: (i) diffusion term $(-D_i \nabla \varphi)$ and (ii) migration term $(-z_i u_i c_i \nabla \varphi)$. Here, $D_i \, (\mathrm{m}^2/\mathrm{s})$ denotes its diffusion coefficient, $u_i \, (\mathrm{m}^2/\mathrm{s} \cdot \mathrm{V})$ denotes its mobility, $c_i \, (\mathrm{mol}/\mathrm{m}^3)$ gives its concentration, z_i is its charge number (for oxygen obviously $z_{O_2} = 0$), and $\varphi \, (\mathrm{V})$ is the electrostatic potential whose negative gradient, $-\nabla \varphi$, is the electric field density. We see that in dilute electrolytes the transport of each species is characterized by two transport parameters: diffusion coefficient (D_i) and mobility (u_i). But these two parameters are approximately related by the Einstein–Smoluchowski equation [3], $u_i = z_i (F/RT) D_i$, thus the flux expression is now simplified to

$$\mathbf{J}_i = -D_i (\nabla c_i + \tfrac{z_i F}{RT} c_i \nabla \varphi), \tag{2}$$

where: T is the temperature (K), F is Faraday's constant, and R is the universal gas constant.

Now a material balance for species i is

$$\frac{\partial c_i}{\partial t} = -\operatorname{div} \mathbf{J}_i + R_i, \tag{3}$$

with $R_i \, (\mathrm{mol}/\mathrm{m}^3 \cdot \mathrm{s})$ describing the homogeneous reaction in which species i is produced/consumed. The electric field could be in principle computed by using the Poisson equation, $\Delta \varphi = -\frac{F}{\varepsilon_r \varepsilon_0} \sum_i z_i c_i$, but it is almost impossible for larger domains (on the order of meters) as the numerical solution for Poisson equation with very small electrical imbalance would required the mesh with element size below 10^{-8} m. Hence, in the literature there are several approximations which replace the Poisson equation with some other equation. In this work the electroneutrality approximation will be used:

$$\sum_i z_i c_i = 0, \tag{4}$$

where the sum is over all ionic species.

Boundary conditions result from the assumed corrosion reactions [4]

$$\begin{aligned}
&\textit{iron oxidation}: && \mathrm{Fe} \rightarrow \mathrm{Fe}^{2+} + 2e^- \\
&\textit{zinc oxidation}: && \mathrm{Zn} \rightarrow \mathrm{Zn}^{2+} + 2e^- \\
&\textit{oxygen reduction}: && \mathrm{O}_2 + 2\mathrm{H}_2\mathrm{O} + 4e^- \rightarrow 4\mathrm{OH}^-
\end{aligned} \tag{5}$$
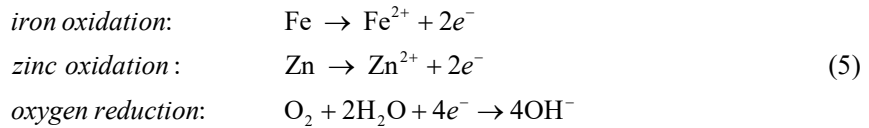
The Tafel equation which connects the electrode potential with the current density allows to define boundary condition for species Fe^{2+}, Zn^{2+}, O_2 and OH^-. Hence, we have the following equalities on the boundary:

$$\text{active bar}: \quad -\boldsymbol{n} \cdot \mathbf{J}_{Fe^{2+}} = \frac{1}{2F} i_{Fe}, \quad -\boldsymbol{n} \cdot \mathbf{J}_{O_2} = \frac{1}{4F} i_{O_2}, \quad -\boldsymbol{n} \cdot \mathbf{J}_{OH^-} = \frac{1}{F} i_{O_2},$$

$$\text{passive bar}: \quad -\boldsymbol{n} \cdot \mathbf{J}_{O_2} = \frac{1}{4F} i_{O_2}, \quad -\boldsymbol{n} \cdot \mathbf{J}_{OH^-} = \frac{1}{F} i_{O_2}, \tag{6}$$

$$\text{sacrificial anode}: \quad -\boldsymbol{n} \cdot \mathbf{J}_{Zn^{2+}} = \frac{1}{2F} i_{Zn}, \quad -\boldsymbol{n} \cdot \mathbf{J}_{O_2} = \frac{1}{4F} i_{O_2}, \quad -\boldsymbol{n} \cdot \mathbf{J}_{OH^-} = \frac{1}{F} i_{O_2},$$

where analytical form of the relation between current density through the electrode/electrolyte interface and the potential difference across this interface is:

anodic Tafel eq : $i = i^0 \cdot e^{2.303(\varphi_s - \varphi - E_{eq})/b_a}$, cathodic Tafel eq : $i = i^0 \cdot e^{-2.303(\varphi_s - \varphi - E_{eq})/b_c}$,

cathodic Tafel with concentration polarization : $i = i^0 (c_i / c_{ref}) e^{-2.303(\varphi_s - \varphi - E_{eq})/b_c}$,   (7)

where all relevant parameters: i^0 (A/m^2) exchange current density, E_{eq} (V *vs. ref*) electrode reaction equilibrium potential (vs. reference electrode, usually SCE), Tafel coefficients b_a, b_c (V) are selected for the specific reaction and electrode.

Ther parts of the boundary system which are not covered by condition (5) and (6) will be assume as isolating boundary:

$$-\boldsymbol{n} \cdot \mathbf{J}_i = 0, \quad i = O_2, \ Zn^{2+}, \ OH^-, \ Fe^{2+}.$$ (8)
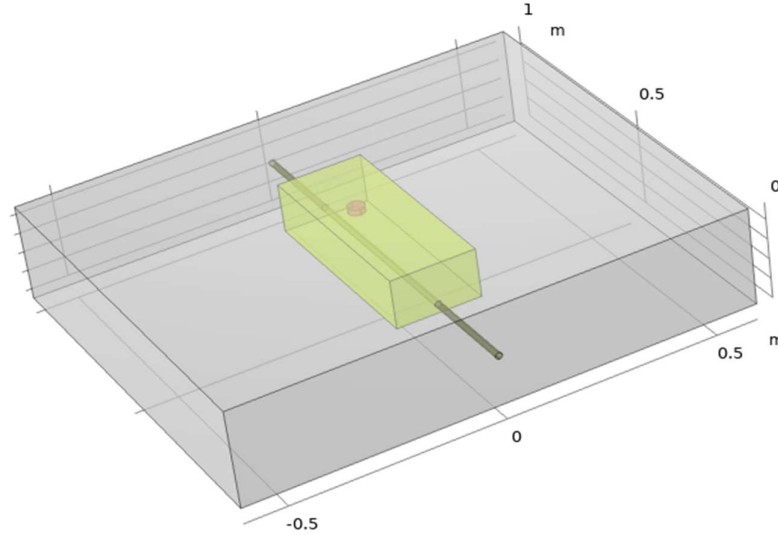
Figure 1. Geometry and arrangements of basic elements in patch repair considered in the work. Grey block represents a fragment of the concrete with embedded rebar (horizontal long dark-grey cylinder. Yellow block represents the part where contaminated concrete was replaced with a fresh one. Pink small cylinder represents the zinc anode.

3. Results of numerical simulations

A typical simulations consider the situation before and after repair. The model allows for computing all interesting quantities (concentrations and fluxes of all species, current density distributions, total current on the active bar etc.). For example, in the case of corroding rebar (Figure 1) the total corrosion current on the active part was calculated to be $1.87 \cdot 10^{-5}$ A before patch repair. After applying the patch repair as indicated in the picture and assuming that diffusion coefficients in the patch a reduced by one order as compared to values before repair we obtained the current value $6.51 \cdot 10^{-6}$ A which is almost ten times smaller. Moreover, the sensitivity analysis have shown that this value is not much effected by the diffusion coefficients in the patch, but rather on the presence of the SACP anode. Another type of simulations was related to the dependence of the corrosion current on the locations of the anode (SACP) and can be viewed as the search for its optimal position. For simplicity we performed only one dimensional optimization by changing the location of the SACP only in one direction. The results are presented in Figure 2, and from it we see that the plot is symmetric with respect to the middle position (as expected due to the symmetry of the model with respect to the plane perpendicular to the rebar axis), but more interestingly we see that better effectiveness is achieved not by placing the anode in the middle but near one of the edges of the patch.
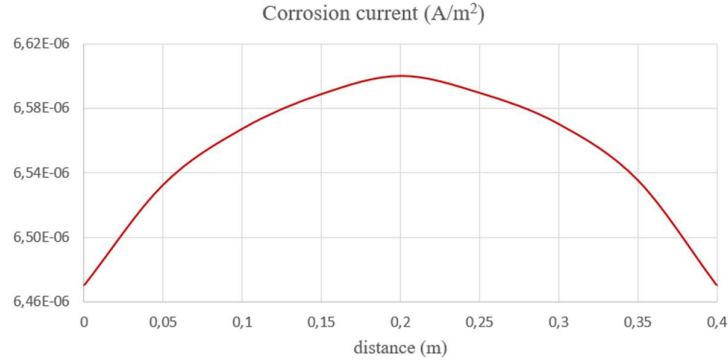
Figure 2. Corrosion current as a function of the location of SACP along the rebar. Distance = 0 corresponds to the initial position of SACP shown in Figure 1. Increasing values of distance correspond to moving the anode to the front.

We have also evaluated the impact of the active cathodic protection in the presented system. To this goal, the computations were performed with applied voltage $E_{app} = -0.7$ V (the rebar being negatively polarized relative to the SACP). Now the value of the corrosion current is changed dramatically, as from the anodic dissolution current it turns out to be the cathodic current with the value $I = -1.13 \cdot 10^{-4}$ A.

4. Conclusions

This study shows how a multi-species transport model with current and potential distribution can be applied to investigate cathodic protection and patch repair effects. It is more advanced than most of the treatments in the current literature which basically are simple electrical models based on Ohm's law ($\mathbf{i} = -\sigma \nabla \varphi$) with one bulk parameter (conductivity) [5]. Such models solve in fact a simple equation for the electric potential (Laplace's equation) with nonlinear boundary conditions (of the Tafel type). Some of these models do include very weak coupling with oxygen through the boundary conditions (concentration polarization), but still this is very simplistic. Currently, the models which are better description of reality should include the transport of all relevant species (ionic and neutral) where the current density is given by $\mathbf{i} = F \sum_i z_i \mathbf{J}_i$. Moreover, these models allow for realistic treatment of the surface reactions (such as shown in (5)) with each species having its own characteristic physical parameters (exchange current density, charge transfer coefficients, equilibrium potentials etc.). The main difficulty in this approach is the calculation of the electric potential. In theory, the Poisson equation could be used, but it is – for numerical reasons – not possible currently for larger domains (Poisson's equation has been successfully used in the domain of small sizes, for example the ion selective membranes or ionic channels in the biological membranes). Thus, in concrete construction (sizes on the order of meters) some approximation to replace the Poisson equation must be used There are two that are frequently used: the Laplace equation or the electroneutrality. We believe that the electroneutrality equation is a better approximation than the Laplace equation (which is very good for metal conductors) because the tests we have performed unequivocally show that when the Laplace equation is used with transport equations (2) and (3), a value of the charge density ($F \sum_i z_i c_i$) in the system assumes unreasonably larger values ($\sim 10^3$ C/dm^3) or higher which definitely can not exist in the macroscopic stable systems. This, often overlooked fact, leads us to promoting the use of electroneutrality condition (4) as the well justified approximation for computing the electric potential in the multi-ion transport systems.

References

[1] Zhang, B. *et al.* (2018) "Unmasking chloride attack on the passive film of metals", *Nat. Comm.* **9**, 2559.

[2] Lozinguez, E. *et al*. (2018) "Contribution of Sacrificial anode in reinforced concrete patch repair: Results of numerical simulations", *Constr. Build. Mat*. **178**, 405–417.

[3] Allen J. Bard, Larry R. Faulkner, "Electrochemical Methods – Fundamentals and Applications", Wiley, 2001, second edition.

[4] Muehlenkamp, E.B. et al. (2005) "Effect of Moisture on the Spatial Uniformity of Cathodic Protection of Steel in Reinforced Concrete", *Corrosion* **61**(6), 519–533.

[5] Cao, C. *et al*. (2013) "Modelling of interaction between corrosion-induced concrete cover crack and steel corrosion rate", *Corr. Sci*. **69**, 97–109.

Improved tensile performance of strain-hardening geopolymer composites using treated CBA and polyethylene fiber

Suhawn Ju[1*], Minchang Kang[2], and Sukhoon Pyo[3]

[1] *Department of Urban and Environmental Engineering, Ulsan National Institute of Science and Technology (UNIST), 50 UNIST-gil, Ulju-gun, Ulsan 44919, Republic of Korea*
Email: gn00147@unist.ac.kr
[2] *Department of Urban and Environmental Engineering, Ulsan National Institute of Science and Technology (UNIST), 50 UNIST-gil, Ulju-gun, Ulsan 44919, Republic of Korea*
Email: cmway013@unist.ac.kr
[3] *Department of Urban and Environmental Engineering, Ulsan National Institute of Science and Technology (UNIST), 50 UNIST-gil, Ulju-gun, Ulsan 44919, Republic of Korea*
Email: shpyo@unist.ac.kr

ABSTRACT

In this study, a strain-hardening geopolymer composite (SHGC) based on ground granulated blast furnace slag (GGBFS) was developed by incorporating treated coal bottom ash (CBA) and polyethylene (PE) fiber. Treated CBA and PE fiber were used to improve the tensile performance and sustainability of SHGC, and CBA was treated using a solution-dissolving method based on a previous study. Through the solution-dissolving method, not only CBA was utilized as a silicate source for an alkaline solution, but also residue CBA was replaced with sand to mix a geopolymer composite. The morphological surface change after treating CBA was observed through SEM image analysis. SHGC was prepared by containing 2% PE fiber and replacing 100% of sand with treated CBA, and the mechanical performance of the SHGC was evaluated through compressive strength and direct tensile test. Using treated CBA enhanced the tensile behavior of SHGC compared to the sand series. In particular, it showed improvement not only in tensile strength but also in various indicators such as energy absorption capacity and strain-hardening capability.

KEYWORDS: *Strain-hardening geopolymer composites; Polyethylene fiber; Surface morphology; GGBFS; Coal bottom ash*

1. Introduction

Among the primary energy consumption, coal is the second major source occupying around 30% after oil, according to a report of world energy by British Petroleum (BP) ("BP Statistical Review of World Energy 2022, 71st edition," 2022). This use of coal-related energy has mass-produced coal bottom ash (CBA), which occupies about 20% of solid waste worldwide (Ban et al., 2022). The CBA, a by-product of coal-fired power plants, is difficult to recycle compared to the other coal ash types such as fly ash; therefore, most of CBA is buried in landfills. This study not only used CBA as a silicate source by dissolving in an alkali activator but also prepared a strain-hardening geopolymer composite (SHGC) using residual CBA as a fine aggregate after making the alkali activator.

2. Experiment

2.1 Materials

Ground granulated blast furnace slag (GGBFS), fly ash, CBA, and silica sand were used as binders, and an alkaline activator was prepared using sodium hydroxide solution, CBA, and silica fume.

2.2 Sample preparation

The alkaline activator was stirred at 75°C for 24 hours using a magnetic stirrer after dissolving the CBA or silica fume in the sodium hydroxide solution. Table 1 summarizes the mix proportions and describes the sample names by CBA content. After mixing, the mixture was casted into molds and demolded after one day. After demolding, the samples were cured under sealed conditions at 80°C for one day. A direct tensile test was performed to evaluate the tensile performance of the SHGC depending on the CBA content.

Table 1. Mix proportion of SHGC

Sample	Design parameter			Mix design (kg/m³)									
	CBA content	PE fiber 1)	SP Content 2)	Precursor		Fine aggregate			Activator			
				GGBFS	fly ash	silica sand No.6	silica sand No.8	treated CBA	water	NaOH	SF	ion CBA
CBA0	0%	2%	4%	790.8	197.7	156.0	66.9	-	428.2	137.0	98.0	-
CBA25	25%	2%	6%	793.0	198.2	119.1	51.0	49.9	428.8	137.2	73.7	21.4
CBA50	50%	2%	6%	794.5	198.6	79.6	34.1	99.9	429.6	137.4	49.2	42.8
CBA75	75%	2%	6%	796.1	199.0	39.9	17.1	150.2	430.5	137.7	24.7	64.4
CBA100	100%	2%	6%	793.4	198.3	-	-	199.6	429.0	137.2	-	98.3

1)   Volume fraction
2)   Mass ratios of precursor weight

3. Result and discussions

3.1 Treated CBA

Figure 1 shows the amount of Si^{4+} extracted from CBA and SF in sodium hydroxide solution. When the same weight was used, the amount of Si^{4+} extracted from CBA was approximately 30% of that from SF. Additionally, the amount of Al^{3+} was analyzed but was not observed. Based on the ICP results, the calculated amount of Si^{4+} obtained when using CBA as a silicate source in the alkaline activator was determined, and the experimental mix design was finalized.
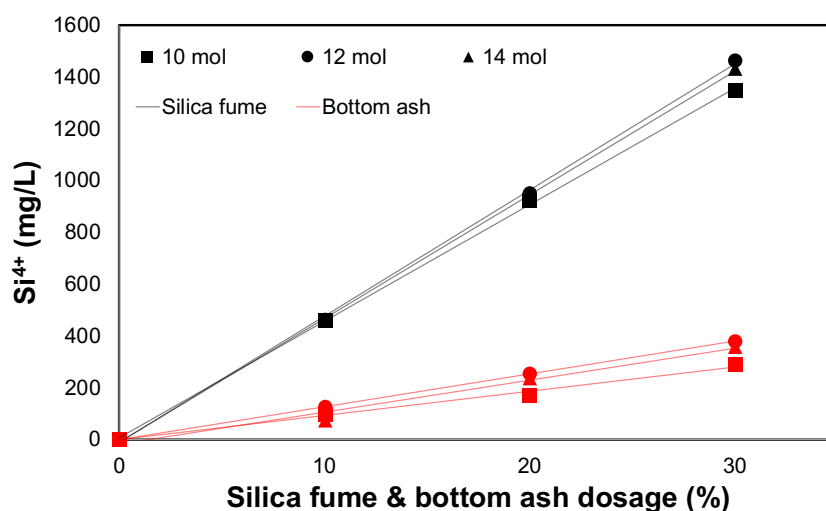
Figure 1. Amounts of Si^{4+} extracted from of CBA and SF in sodium hydroxide solution.

Figure 2 presents the XRD patterns of raw CBA and the residual CBA after preparing the alkaline activator. Raw CBA shows the crystal phase of mullite and quartz, as well as an amorphous phase. The amorphous phase is observed in a broad bump between 18-30°, and it can be observed that this broad bump decreases

in the residual CBA. This indicates that the amorphous phase of raw CBA was dissolved in the sodium hydroxide solution, resulting in the extraction of Si^{4+}.
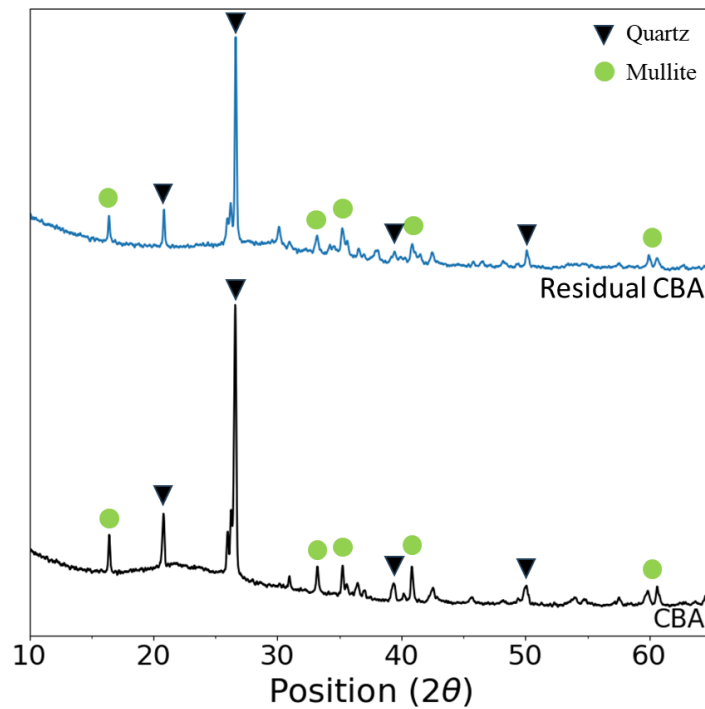
Figure 2. XRD patterns of raw CBA and residual CBA.

Figure 3 shows the surface changes of CBA after the preparation of the alkaline activator. It was observed that the surface of the CBA was rough after the silicate source of the amorphous phase in the raw CBA was extracted into the sodium hydroxide solution. It can be said that such a change in the surface of the CBA will have a positive effect on the tensile performance.
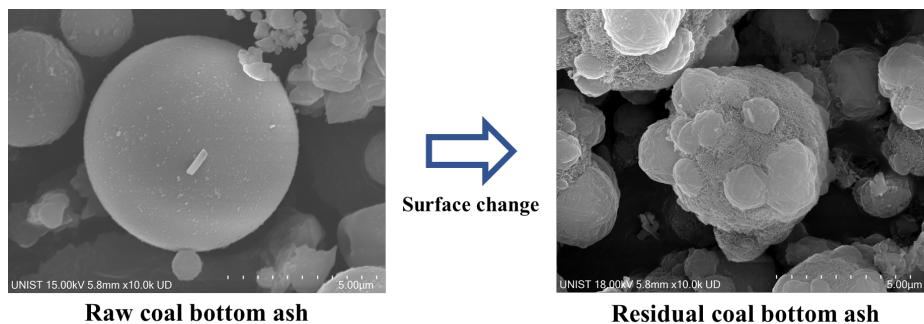
Figure 3. SEM images of the raw CBA and residual CBA.

3.2 Tensile performance

The results of the direct tensile test of SHGC by CBA content are illustrated in Figure 4. The CBA0 specimen, in which CBA was not incorporated, showed a comparable trend to previous research results (Yoo et al., 2022; Shaikh et al., 2018), and it was observed that the tensile performance improved with an increasing amount of CBA. This can be attributed to the rough surface of residual CBA, which has a positive impact on enhancing tensile performance.
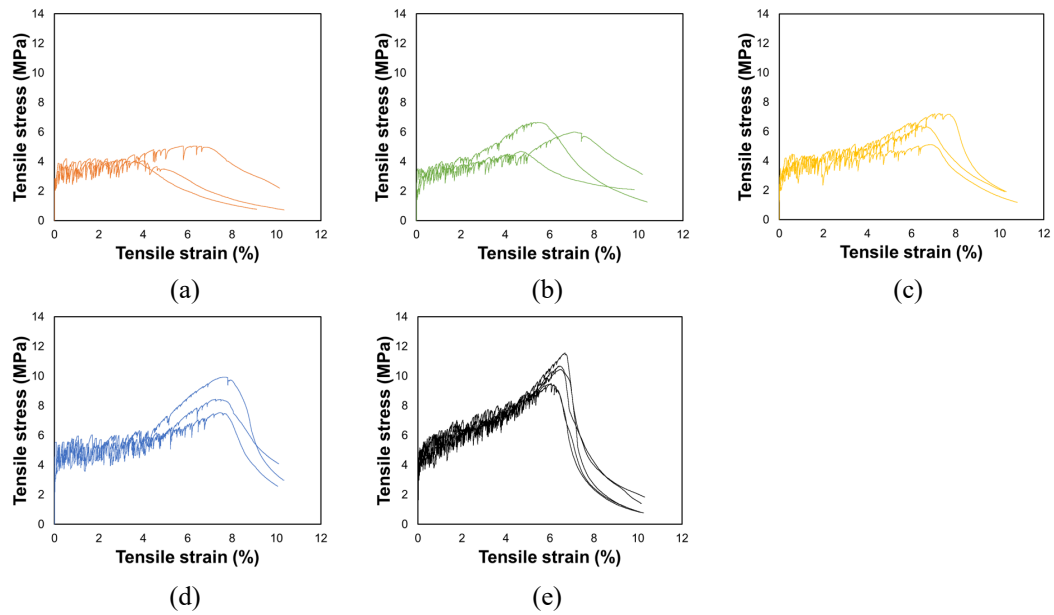
Figure 4. Tensile stress vs. strain curve according to CBA content:
(a) CBA0, (b) CBA25, (c) CBA50, (d) CBA75, and (e) CBA100

4. Conclusions

This study employed the method of utilizing CBA as a silicate source developed in a previous study, while also utilizing the remaining bottom ash as fine aggregates to develop an eco-friendly SHGC. The results confirmed that as the amount of CBA increases, the tensile performance improves, thereby suggesting a novel sustainable method of utilizing CBA in SHGC.

Acknowledgements

References

BP Statistical Review of World Energy 2022, 71st edition, 2022.

  https://www.bp.com/en/global/corporate/energy-econ

Ban, C.C., Le Ping, K.K., Jia, L.J., Siddique, R., Tangchirapat, W., Bin Megat Johari, M.A., 2022. Coal bottom ash as constituent binder and aggregate replacement in cementitious and geopolymer composites: A review. J. Build. Eng. 104369. https://doi.org/10.1016/j.jobe.2022.104369

Shaikh, F.U.A., Fairchild, A., Zammar, R., 2018. Comparative strain and deflection hardening behaviour of polyethylene fibre reinforced ambient air and heat cured geopolymer composites. Constr. Build. Mater. 163, 890–900. https://doi.org/10.1016/j.conbuildmat.2017.12.175

Yoo, D.Y., Lee, S.K., You, I., Oh, T., Lee, Y., Zi, G., 2022. Development of strain-hardening geopolymer mortar based on liquid-crystal display (LCD) glass and blast furnace slag. Constr. Build. Mater. 331, 127334. https://doi.org/10.1016/j.conbuildmat.2022.127334

The 16th International Congress on the Chemistry of Cement 2023 (ICCC2023)
"Further Reduction of CO_2 -Emissions and Circularity in the Cement and Concrete Industry"
September 18–22, 2023, Bangkok, Thailand

Effect of CO_2 curing on bonding strength and microstructure in the interfacial transition zone

Y. Huang[1], X. Hu[1], and C.J. Shi[1*]

[1] *College of Civil Engineering, Hunan university, Changsha, 410082, China*
Email: yanhuang666@hnu.edu.cn
[1] *College of Civil Engineering, Hunan university, Changsha, 410082, China*
Email: xianghu @hnu.edu.cn
[1] *College of Civil Engineering, Hunan university, Changsha, 410082, China*
Email: cshi@hnu.edu.cn

ABSTRACT

The interfacial transition zone (ITZ) between aggregate and cement paste is a key factor for the performance and failure mechanism of concrete due to its high porosity and enrichment of the oriented calcium hydroxide ($Ca(OH)_2$) crystals, and CO_2 curing is a promising technique for consuming $Ca(OH)_2$ and forming calcium carbonate ($CaCO_3$) to reduce porosity and improve strength. However, the effect of CO_2 curing on the mechanical and microscopic properties of the ITZ is not clear. In this study, the effect of CO_2 curing on ITZ was investigated using splitting tensile bonding tests, X-ray diffraction (XRD) and backscattered electron imaging (SEM-BSE). In addition, the thickness of the ITZ was determined by the decreasing segment of porosity across the interface between the aggregate and cement paste. Results showed that the porosity and thickness of the ITZ were significantly reduced after CO_2 curing, and there were almost none of the $Ca(OH)_2$ crystal in the ITZ, which was replaced by a significant precipitation of $CaCO_3$. This indicated that the $CaCO_3$ crystals fill the pores and thus improve the bonding strength in the ITZ.

KEYWORDS: *CO_2 curing, interfacial transition zone, splitting tensile bonding strength, backscattered electron imaging*

1. Introduction

CO_2 is the main greenhouse gas blamed for global warming. Extensive studies have been conducted on strategies to mitigate CO_2 emissions, in which CO_2 curing techniques not only improving the performance of concrete, but also capturing and storing CO_2 (He et al,2016; Song et al, 2022). However, effects of CO_2 curing on the performance of the ITZ are critical and thorny problems, as the ITZ is generally considered to be the weakest link in concrete (Wang et al, 2020; Sun et al, 2020). Therefore, studying the effect of CO_2 curing on performance the ITZ will contribute to a further understanding of the influence of CO_2 curing on the properties of concrete.

This work aims to clarifies the bonding strength and microstructure of the ITZ based on the early accelerated CO_2 curing. The bonding strength of ITZ between cement paste and aggregate will be investigated by performing the splitting tensile strength test. The porosity distribution and chemical composition around the ITZs will be measured by the SEM and XRD.

2. Experimental program

2.1 Materials

The P.I 42.5 type Portland cement with a specific surface area of 356 m^2/kg was utilized in this work, and its chemical composition is shown in Table 1. The cube aggregates with 20 mm × 20 mm × 10 mm were

extracted from the limestone by cutting to test the bonding strength and microstructure properties of ITZ between the cement paste and aggregate.

Table 1 Chemical composition of Portland cement.

SiO$_2$	Al$_2$O$_3$	Fe$_2$O$_3$	CaO	MgO	SO$_3$	Na$_2$Oeq	f-CaO
20.78	5.08	3.29	63.46	2.30	2.15	0.56	0.80

2.2 Mix process

The water to cement ratio of 0.35 (mass basis) was used to study the bonding strength and microstructure of the ITZ. The mixing process of specimen was described as follows. Firstly, the cube aggregates were kept in water for more than 24 hours before casting to keep the surface moist. Before casting, they were removed and any excess water on the surfaces was dried by a damp cloth. Then, the aggregate was placed on one side of the mold and the fresh cement paste was filled into the other side, and the Fig. 1 showed the details of the specimen.
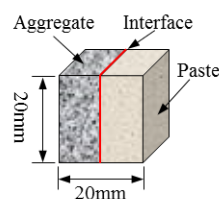
Fig. 1 A sketch of specimen with dimension details.

2.3 Curing regimes

After 8 h after casting, the molds were removed and divided into two batches. One batch was left in a room with 20 ± 2°C and 60% relative humidity for 4 h to make the specimens lose water for pre-condition. Then, the specimens were sealed on five sides, with hot paraffin coating and only one side of the paste exposed to ensure that CO_2 gas only diffused in one dimension. Next, the specimens were accelerated carbonated for two and a half days in a CO_2 chamber at a pressure of 0.2 MPa, a temperature of approximately 20°C and 60% RH. The other batch was cured in saturated lime water at 20°C for 3 d.

2.4 Samples preparation

To understand the effect of CO_2 curing on the chemical composition of the ITZ, the powders in the ITZ were collected for XRD analysis using a computer numerical controlled machine, which were ground to a finer powder and passed through a 45 μm sieve. And all finer powder samples were dried in a vacuum oven at 40 °C for 2 days.

To comprehend the effect of CO_2 curing on the microstructure of the ITZ, the small cube samples with 10 mm × 10 mm × 10 mm in the centre of the specimen was cut using a low-speed diamond saw-cutting system. After cutting, the samples were stored in the ethyl alcohol solution for 3 d to stop the hydration and then kept in the vacuum drying oven (40 ± 2 °C) for another 2 d. Then, the samples were vacuum-impregnated with a low viscosity and high permeability epoxy resin. Finally, the samples were ground and polished by an automatic grinding and polishing machine to ensure that the observation surface is smooth and flat for the SEM-BSE test.

2.5 Testing methods

The bonding strength of ITZ between cement paste and aggregate was measured by performing the splitting tensile test using microcomputer control electronic universal testing machine. A displacement-controlled load was applied at a rate of 0.05mm/min to ensure a quasi-static loading process.

The XRD analysis was performed using R-axis Spider X-ray diffraction and a Cu kα X-ray radiation source. The 2θ scanning range was 5° – 70°, the step size was 0.02°, and the speed was 2 °/min.

The BSE image analysis was tested by A field emission scanning electron microscope (SEM) equipment equipped with a backscattered electron (BSE) image detector to survey the porosity changes of ITZ at different curing regimes. At least 30 images of the ITZ for each sample were taken at 800× magnification

and the resolution were 2048 × 2176 pixels (pixel size of 0.131 μm). In order to characterize the performance of the ITZ along the distance from the aggregate surface, concentric expansion method was used to divide several successive strips of equal distance, so that each BSE image was delineated with 30 strips of 5 μm wide. The porosity of each strip was determined as the percentage of area of pores to total area of the strip (Xie et al, 2015).

3. Results and discussions

3.1 Bonding strength

Fig. 2 showed the splitting tensile bonding strength of different curing methods for 3d. It can be visually observed that the CO_2 curing significantly improved the bonding strength of the ITZ. The splitting tensile bonding strength of ITZ under saturated lime water curing was 1.06MPa, while the ITZ bonding strength subjected to CO_2 curing was 1.74 MPa, which was 64.1% higher than that of ITZ under saturated lime water curing. It indicated that CO_2 curing for 3 days can significantly improve the bonding strength of the ITZ.
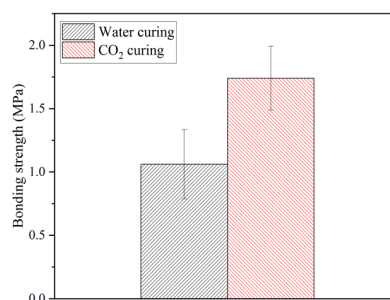
Fig. 2 Splitting tensile bonding strength of ITZ subjected to different curing methods

3.2 XRD analysis

Fig. 3 showed the XRD patterns of the ITZ with different curing methods. The results of the XRD pattern indicated that many diffraction peaks of $Ca(OH)_2$ were observed in water curing. However, after the CO_2 curing, these diffraction peaks disappeared and many new $CaCO_3$ diffraction peaks emerged. This showed that CO_2 curing can promote the convert of $Ca(OH)_2$ to $CaCO_3$, which filled the pores and cracks in ITZ and improved the performances of concrete. In addition, the C_2S and C_3S diffraction peaks of the cement clinker were evident in the water curing samples compared to the CO_2 curing samples. This indicated a more intense carbonation reaction and a higher degree of reaction (Lu et al, 2022). The Rietved method was used to quantify the content of each phase in the samples and the results were shown in Table 2. The results showed that the relative $CaCO_3$ content after CO_2 curing was approximately 61.6%, and the unhydrated cement clinker after CO_2 curing was approximately half of the water curing, indicating a higher degree of reaction to carbonation. This could be a possible evidence of the fast carbonation reaction kinetics and the formation of $CaCO_3$ prior to the formation of $Ca(OH)_2$ in the CO_2-cured samples (Tu et al, 2016).
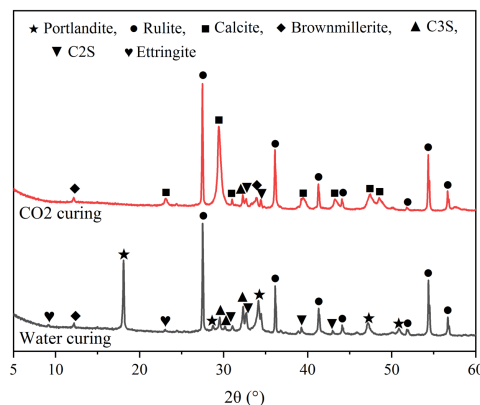
Fig. 3 XRD results of ITZ with different curing regimens

Table 2 Qualitative XRD results of ITZ

Sample	Portlandite	Calcite	Brownmillerite	C_3S	C_2S	Ettringite	Amorphous
Water curing	20.6	0	4.4	10.9	6.7	1	56.4
CO_2 curing	0	61.6	4.9	6.8	2.8	0	23.9

3.3 Microscopic characterization of ITZ

Fig. 4 gived the BSE results of the ITZ with different curing regimes, which showed that sample with CO_2 curing had lower porosity in the ITZ than those with water curing. In general, lower porosity of the ITZ suggestd stronger and more durable interface between cement paste and aggregates. In addition, as the distance from the aggregate surface increased, the porosity gradually decreased and eventually tended to a steady state in all sample. Therefore, many experts and scholars refer to the descending section as the ITZ (Xie et al, 2015). Based on Fig. 4, it can be concluded that the thickness of the ITZ of water curing was about 100 μm, while that of CO_2 curing was about 80 μm, a reduction of 20%, which demonstrated the effectiveness of CO_2 curing in reducing the thickness and porosity of the ITZ.
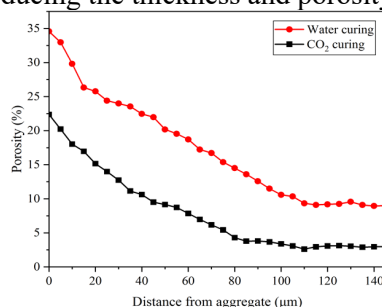
Fig.4 BSE results of the ITZ with different curing regimes.

4. Conclusions

The bonding strength and microscopic properties of the ITZ were investigated under different curing regimes. The experimental results showed that CO_2 curing improved significantly the bonding strength of the ITZ by 64.1% from 1.06 MPa of water curing to 1.74MPa with CO_2 curing. In addition, based on the SEM-BSE results, the porosity of the ITZ subjected to CO_2 curing was substantially reduced, and the thickness of the ITZ was also decreased from around 100 μm to 80 μm. What's more, the product of the ITZ after water curing was mainly $Ca(OH)_2$ and the unhydrated cement clinker represented 22 % of the sample, whereas the product of the ITZ after CO_2 curing was mainly $CaCO_3$ crystals and the unreacted cement clinker accounted for only 14.5% of the sample and 65.9% of the clinker content with water curing. This is due to the more violent and the higher degree of carbonation reaction.

Reference

He, P.P., Shi, C.J., Tu, Z.J., et al. (2016) "Effect of further water curing on compressive strength and microstructure of CO_2 -cured concrete", *Cement and Concrete Composites*, 72:80-88.

Lu, B., Drissi, S., Liu, J. H., et al. (2022) "Effect of temperature on CO_2 curing, compressive strength and microstructure of cement paste", *Cement and Concrete Research*, 157: 106827.

Tu, Z. J., Guo, M. Z., Cai, S. P., et al. (2016) "Effects of limestone powder on CaCO3 precipitation in CO2 cured cement pastes", Cement and Concrete Composites, 72: 9-16.

Song, B.X., Liu, S.H., Hu, X., et al. (2022) "Compressive strength, water and chloride transport properties of early CO_2-cured Portland cement-fly ash-slag ternary mortars", *Cement and Concrete Composites*, 134: 104786.

Sun, D. D., Shi, H. S., Wu, K., et al. (2020) "Influence of aggregate surface treatment on corrosion resistance of cement composite under chloride attack", *Construction and Building Materials*, 248: 118636.

Wang, X. Y., Dong, S. F., Ashour, A., et al. (2020) "Effect and mechanisms of nanomaterials on interface between aggregates and cement mortars", *Construction and Building Materials*, 240: 117942.

Xie, Y. T., Corr, D. J., Jin, F., (2015) "Experimental study of the interfacial transition zone (ITZ) of model rock-filled concrete (RFC)", *Cement and Concrete Composites*, 55: 223-231.

The 16th International Congress on the Chemistry of Cement 2023 (ICCC2023)
"Further Reduction of CO_2 -Emissions and Circularity in the Cement and Concrete Industry"
September 18–22, 2023, Bangkok, Thailand

Incorporation of construction and demolition waste (CDW) in fiber cement submitted to the accelerated carbonation process

D.O. Lima[1], R.H. Filomeno[2], M.R. Frías[3,*], and H. Savastano Junior[4]

[1] *University of São Paulo (USP), São Paulo, Brasil*
Email: Daniela.engcivil@usp.br
[2] *University of São Paulo (USP), São Paulo, Brasil*
Email: rafaelfilomeno@usp.br
[3] *Eduardo Torroja Institute for Construction Science (IETcc-CSIC), Madrid, Spain*
Email: mfrias@ietcc.csic.es
[4] *University of São Paulo (USP), São Paulo, Brasil*
Email: holmersj@usp.br

ABSTRACT

One of the main problems associated with the socioeconomic development of a country is the generation of construction and demolition waste (CDW), which represents between 30-50% of the total waste generated worldwide. The motivation of the present work is to develop materials with less cement utilization, and strategies for CO_2 sequestration. Thus, the work aimed to evaluate the application of the fine fraction of CDW (<63 μm) from waste concrete, to partially replace Portland cement (10% by mass) in the production of fiber cement composites submitted to the carbonation process in the early ages. The fiber cement pads were produced with 10% of bleached hardwood kraft pulp of eucalyptus by the slurry dewatering and pressing method and were analyzed before and after the accelerated carbonation curing. The accelerated carbonation took place in a laboratory chamber at 60°C, 5 bar of pressure, CO_2 saturation, and sample moisture of 60% for 24 h. The samples were evaluated for physic-mechanical and microstructural performance and X-ray diffraction. The carbonated samples presented an increase of approximately 60% in flexural strength compared with their non-carbonated counterparts. Although there is a tendency for carbonation to decrease the deformation capacity of fiber cement, the addition of CDW compensated for this embrittlement, providing an increase of 40% in specific energy, due to the better packing of the particles and optimizing the fiber interface. This behavior was confirmed through the microstructural assessment of the material, presenting a more compact and less porous matrix and fiber-matrix transition zone. In general, the substitution of 10% by mass of Portland cement by the fine fraction of CDW, contributes beneficially to the physic-mechanical performance of fiber cement, improving the effectiveness of the carbonation process.

KEYWORDS: *Construction and demolition waste; Eco-efficient cement; Fiber-cement; Accelerated carbonation.*

1. Introduction

Civil construction activities generate a large amount of waste, called construction and demolition waste (CDW). An alternative to minimize the impacts caused by this type of waste is to reuse it as a secondary raw material, such as aggregates, fillers, or eco-efficient pozzolana. Concerning the fine fraction of CDW (< 5 mm), studies have evaluated its viability as complementary cementitious materials for the production of eco-efficient cement (Frías et al, 2020; Monasterio et al, 2022). Concluding that depending on the origin, granulometry, chemical, and mineralogical composition, the recycled concrete fines generated during the production of recycled concrete aggregates can be used as filler or as supplementary cementitious materials (SCM), since the fine fractions can have cementitious properties, due to the presence of unhydrated cement grains in its composition (Frías et al, 2020; Moreno-Juez et al, 2021).

In this context, aiming at new applications for the use of CDW, the study evaluated the physic-mechanical and microstructural behavior of fiber cement reinforced with bleached eucalyptus cellulosic pulps, partially replacing Portland cement by recycled concrete fines (< 63 μm) subjected to thermal curing and the accelerated carbonation process, for the production of thin flat sheets without a structural function.

2. Materials and Methods

2.1 Materials

The composites were produced with type III Portland cement (ASTM C150); ground limestone, fixed in the formulation at 12.8% by mass; and bleached hardwood kraft pulp of eucalyptus (fixed at 10%, by mass), donated by Infibra (Brazil). The CDW was donated by the concrete recycling plant (Eco-X), Guarulhos - SP, Brazil. The material was previously dried in an oven at 60°C for 24 h. Then, it was sieved to obtain the fraction that passed through a 0.15 mm sieve. The fines were milled to fragment the particles at 63 μm. The materials presented D_{50} of 9.07 μm, 24.0 μm, and 16.4 μm, to the Portland cement, CDW, and limestone, respectively.

2.2 Methods

2.2.1 Production and curing of the fiber cement composites

The fiber cement pads (200 x 200 x 5) mm³ were produced by slurry dewatering and pressing method (Savastano et al, 2000). CDW was used to replace 10% of Portland cement, by mass. Initial curing was accomplished at a saturated condition (± 28 ºC) for 24 h. Then, thermal curing was used for the reference conditions and accelerated carbonation was used for the additional treatments. Thermal curing was controlled thermal bath chamber, with a relative humidity of ~ 90% at a temperature of 60 ºC (water vapor at 55 ºC), for 6 days. This process occurred in the formulations with CDW (CDW_TC) and without CDW (REF_TC). The accelerated carbonation was carried out after the initial 24 h of curing, the plates were placed in a laboratory chamber at 60ºC, under a pressure of 5 bar, CO_2 saturation (~100%), and sample moisture of 60% for 24 h, according to Filomeno et al (2020). This accelerated carbonation step used formulations with CDW (CDW_CO2) and without CDW (REF_CO2).

2.2.2 Characterization of fiber cement

X-ray diffraction (XRD) was determined operating at 40 kV and 30 mA, in a step of 0.02º per second and measurement interval between the Bragg angles (2θ) from 5º to 60º, with intensities recorded for 2º/min. Before the XRD analysis, the samples were previously ground and sieved (Filomeno et al, 2020).
The mechanical properties were obtained using a four-point bending test, following Tonoli et al (2007). Modulus of rupture (MOR), and specific energy (SE) were determined. The bulk density (BD), and apparent porosity were evaluated according to the procedures established by ASTM C 948-81. The results of the physic-mechanical analysis were treated statistically using the statistical software SAS 9.4 (Statistical Analysis System). The microstructural analysis was performed using scanning electron microscopy with backscattered electron image (SEM-BEI) to evaluate the fiber-matrix interface and the transition zone on the polished surface of the fiber cement.

3. Results and Discussion

3.1 X-Ray Diffraction (XRD)

The diffractograms (Fig. 1) show an increase in the intensity of calcite peaks after the carbonation process, due to the reaction that occurs between dissolved CO_2 and calcium hydroxide mainly, resulting in the dissolution of portlandite and precipitation of $CaCO_3$ (Hunnicutt et al, 2017). The accelerated carbonation process led to the disappearance of $Ca(OH)_2$ (broadband 2θ = 28.6º, 50.7º, and 54.3º), this

factor can provide greater durability of the vegetable fibers in the cementitious matrix. In composites with CDW, peaks related to quartz were identified, due to the aggregates in the original concrete.
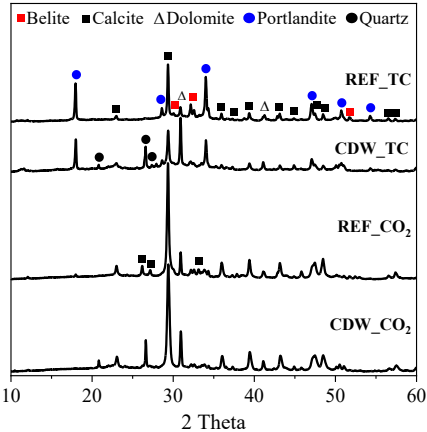
Fig. 1 – X-ray diffractograms of carbonated and non-carbonated fiber cement samples.

3.2 Physic-mechanical characterization

Fig. 2a shows the correlation of the modulus of rupture (MOR) versus specific energy (SE) of carbonated and non-carbonated fiber cement with 10% CDW. The CDW_TC composite presented physic-mechanical performance statistically equal to REF_TC. The MOR was 9.74 MPa (± 0.89a) and 8.68 MPa (± 0.91a), respectively. And SE of 5.49 (± 0.44a) and 3.69 (± 0.89a), demonstrating that with reduced levels of substitution, CDW does not impair the properties of the composite. The carbonated samples presented an approximately 60% increase in MOR compared to their non-carbonated counterparts. Furthermore, although there is a tendency for carbonatation to decrease the ability of energy absorption of the fiber cement, the addition of CDW compensated for this embrittlement, providing an increase of approximately 40% in the SE. This behavior is due to better particle packing and optimization of the fiber-matrix interface. Except for the MOR property, no statistically significant difference was observed for the other physic-mechanical properties of the carbonated samples. The bulk density (BD) results (Fig. 2b) confirm the better behavior of carbonated fiber cement, presenting a denser structure due to the reduction of apparent porosity, filled by the formation of $CaCO_3$.

(a)   (b)
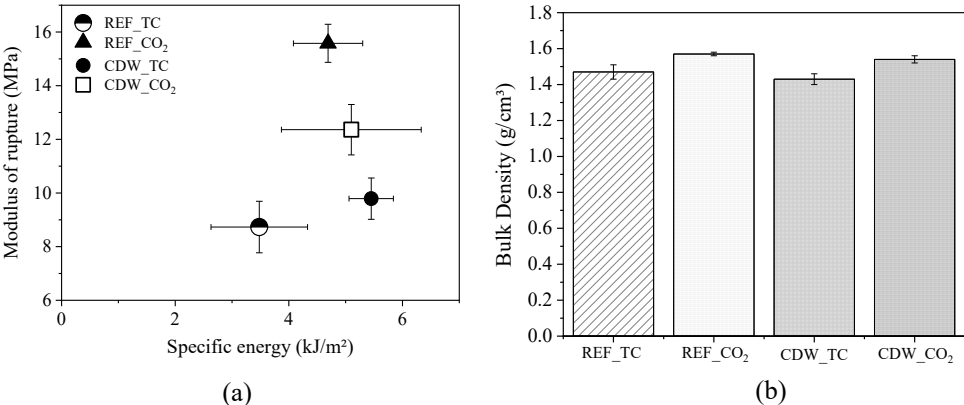
Fig. 2 – Physic-mechanical properties: (a) MOR and SE, and (b) BD of fiber cement.

3.3 Scanning Electron Microscopy (SEM)

The micrographs of the composites are shown in Fig. 3. Arrow 1 indicates fiber contamination by calcium hydroxide. Arrow 2 represents the lack of adhesion between the fiber and the cementitious matrix. It is observed that the carbonation process improved the structure of the matrix, making it more compact, densified structure, and less porous matrix, improving the fiber-matrix transition zone, as indicated by arrow 3.
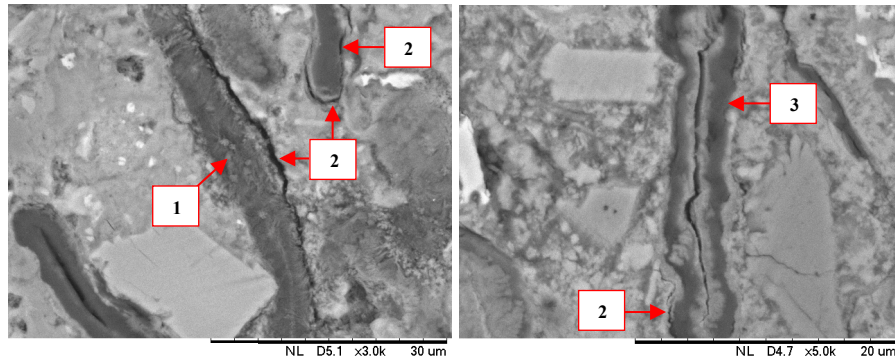
Fig. 3 - Fiber cement: (a) Sample without carbonation, and (b) sample with accelerated carbonation.

4. Conclusions

The use of CDW and accelerated carbonation presented efficient results to improve fiber cement performance with a high cellulose pulp content. Accelerated carbonation densified the cement matrix, refining the porosity and presenting an increase of 60% for the MOR compared to the non-carbonated counterpart. The use of CDW preserved the specific energy and bulk density of the fiber cement even after the accelerated carbonation process and did not present significant statistical differences for the other physic-mechanical properties. In general, the use of 10% CDW does not impair the physic-mechanical performance of the composites. The CDW compensated for the embrittlement, guaranteeing stability in the deformation of the fiber cement. The XRD analysis showed that the accelerated carbonation process led to the disappearance and reduction in the intensity of peaks referring to $Ca(OH)_2$, in addition to an increase in the $CaCO_3$ content.

Acknowledgments

References

American Society for Testing and Materials. ASTM C 948-81: Standard test method for dry and wet bulk density, water absorption and apparent porosity of thin sections of glass-fiber reinforced concrete. ASTM International, West Conshohocken, PA, 2016.

Filomeno, R. H., Rodier, L. B., Ballesteros, J. E. M., Rossignolo, J. A., and Savastano, H. (2020) "Optimizing the modified atmosphere parameters in the carbonation process for improved fiber-cement performance", *Journal of Building Engineering*, 32: 101676

Frías, M., et al (2020) "Multi-Technique Characterization of a Fine Fraction of CDW and Assessment of Reactivity in a CDW/Lime System", *Minerals*, 10(7): 590.

Hunnicutt, W., Struble, L., and Mondal, P. (2017) "Effect of synthesis procedure on carbonation of calcium-silicate-hydrate*", Journal of the American Ceramic Society*, 100(8): 3736–3745.

Monasterio, M., Caneda-Martínez, L., Vegas, I., and Frías, M. (2022) "Progress in the influence of recycled construction and demolition mineral-based blends on the physical-mechanical behaviour of ternary cementitious matrices", *Construction and Building Materials*, 344: 128169.

Moreno-Juez, J., Vegas, I. J., Frías, M., Vigil de la Villa, R., and Guede-Vásquez, E. (2021) "Laboratory-scale study and semi-industrial validation of viability of inorganic CDW fine fractions as SCMs in blended cements", *Construction and Building Materials*, 271: 121823.

Savastano, H., Warden, P., and Coutts, R. S. (2000) "Brazilian waste fibres as reinforcement for cement-based composites", *Cement and Concrete Composites*, 22(5): 379–84.

Tonoli, G. H. D., Joaquim, A. P., Arsène, M.-A., Bilba, K., and Savastano, H. (2007) "Performance and durability of cement based composites reinforced with refined sisal pulp", *Materials and Manufacturing Processes*, 22(2): 149–156.

Alkali-Silica Reactivity in Belitic Calcium Sulfoaluminate (BCSA)

Meghana Maddala[1], Omkar Deo[2], Julio Paniagua[2], Neel Bhuskute[2], Eric P. Bescher[1*]

[2]*CTS Cement Manufacturing Corporation, Garden Grove, CA, USA*
Email: odeo@ctscement.com

[1,*] *Department of Materials Science and Engineering, University of California Los Angeles, Los Angeles, CA, USA*
[*]Email: bescher@ucla.edu

ABSTRACT

Alkali-silica reaction (ASR) is a significant concern for the durability and sustainability of concrete. The widespread occurrence of ASR in portland cement concrete has prompted the use of mitigating admixtures to limit concrete expansion. Supplementary cementitious materials, such as kaolin, fly ash or lithium salts are commonly used for this purpose, but they are either costly or becoming scarce. Preliminary data suggest that belitic calcium sulfoaluminate cement (BCSA) exhibits ASR-mitigating properties. It is speculated that the lower alkali content of the binder, combined with its self-desiccating nature, can lead to excellent ASR mitigation properties. However, there is a lack of data on the topic. This work investigates the behavior of three aggregates (borosilicate glass, Spratt, and Eagle Valley) of different reactivities in BCSA mortars and portland cement mortars. When samples were subjected to accelerated ASR testing per ASTM C441 and C1260, BCSA mortars exhibited lower expansion rates in both of these test protocols. In some instances, BCSA mortars exhibited 1/30th of the portland cement mortars' expansion using the same aggregate. These results indicate that BCSA can be used to mitigate ASR.

KEYWORDS: *alkali-silica reactivity*, *belitic calcium sulfoaluminate cement, low-carbon binders, sustainability, low-carbon concrete durability.*

1. Introduction

As a building material, concrete exhibits high durability, low cost, high fire resistance, and minimal maintenance. However, aggressive environments can lead to the premature degradation of concrete structures. ASR is one of the primary causes of failures for concretes, leading to their expansion and cracking. ASR occurs as a result of (a) the existence of reactive aggregates with amorphous soluble silica, (b) high [OH⁻] concentration in the interstitial pore solution or high alkali concentration, (c) accessibility of an active source of soluble calcium (mainly portlandite) to react with the dissolved silica to form expansive calcium aluminosilicate hydrate (C-A-S-H) gel, and (d) high humidity conditions. Most ASR mitigation measures aim to eliminate one or more of these requirements for ASR. Preventive measures include the use of supplementary cementitious materials (SCMs) or lithium compounds (Thomas (2011)). SCMs reduce the amount of alkalis available in the pore solution while consuming calcium hydroxide to produce more calcium-silicate-hydrate (C-S-H). It has been shown by Chappex and Scrivener (2012) and Szeles et al (2017) that aluminum can act as an ASR mitigating agent. Non-expansive C-A-S-H gel is formed due to aluminum and hydrated alumina, enabling better alkali binding and preventing its leaching into the pore solution.

Preliminary data suggest that BCSA provides some ASR mitigating properties due to its low alkali content and self-desiccating nature. BCSA contains belite instead of alite as its main phase. The absence of alite results in lower manufacturing temperatures for the BCSA clinker and lower limestone requirements. As a result of manufacturing the BCSA clinker 200°C lower than portland cement clinker and the ease of grinding due to a more porous clinker, BCSA is a low carbon footprint binder with 30% fewer carbon

emissions than portland cement (Gartner (2004), Sharp et al. (1999), and Zhang (2000)). With the rising need for better infrastructure and faster construction, especially in developing countries, the demand for cement will continue to grow. There will also be a corresponding rise in the demand for non-reactive aggregates capable of producing durable concrete.

The widespread occurrence of ASR has prompted research on the chemical and physical mechanisms for ASR, aggregate reactivity, alkalis, and soluble silica sources, and, most importantly, measures to mitigate ASR. This work shows the potential of using BCSA and its ability to mitigate ASR based on two accelerated standard test protocols.

2. Materials and Test Methods

2.1 Materials

This study uses two types of binders: ordinary portland cement Type II/V (OPC) from CalPortland® and a commercial BCSA cement called Rapid Set® from CTS Cement Manufacturing Corp. The binders have alkali contents between 0.40% and 0.47%. Three types of aggregates with different levels of reactivity are also used, which include (a) the most reactive aggregate, borosilicate glass (Pyrex® 7740) per ASTM C441, (b) a moderately reactive aggregate called Eagle Valley (EV), and (c) a generally highly reactive aggregate called Spratt (Sp). The main phases in the cement were: belite 48.0 wt%, ye'elimite 27.4 wt%, anhydrite 10.6 wt%, bassanite 3.7% wt%.

2.2 Test Methods

2.2.1 ASTM C441

ASTM C441 method aims to test the effectiveness of a cementitious blend in preventing excessive ASR in mortar. The test is performed using borosilicate aggregate per the standard for its ability to induce ASR due to extreme reactivity. The test helps compare expansions between an experimental and a control binder. It is an accelerated test that gives results in 16 days. One disadvantage of this test is the borosilicate glass's variability, mainly if it is obtained from different sources. However, in this study, the borosilicate aggregate is obtained from the same supplier, and the results are used only for comparison. Hence, the effect of variability is minimized.

2.2.2 ASTM C1260

ASTM C1260 is a test method that evaluates the extent of reactivity of an aggregate to cause ASR. This study uses aggregates with two different reactivity levels (a) a highly reactive aggregate – Sp and (b) a moderately reactive aggregate – EV. These aggregates are selected to compare the binder performance when exposed to different reactive materials. ASTM C1260 is also an accelerated test determining whether an aggregate is reactive within 16 days. The main disadvantage of this test is its severity since the samples are submerged in an alkali-rich environment at 80°C. The conditions of this test do not accurately represent the field conditions; hence the results from this test alone should not be used to assess aggregate reactivity. The findings from this test, along with those from C441, should provide a better indication of the ASR potential of a cementitious mix. It should be noted that many ASR test methods require the use of C150 cements, a classification to which BCSA cement does not belong.

3. Results and Discussion

3.1 Findings from ASTM C441

Figure 1 shows the expansions for mortars made using BCSA and OPC with three different aggregates: Borosilicate, Eagle Valley, and Spratt. While aggregates with different reactivities show similar expansions in mortars made with BCSA (**Fig. 1a**), the difference between expansions of aggregates with varied reactivities is very prominent in the case of mortars made with OPC (**Fig. 1b**). The OPC mortar with borosilicate glass expands more rapidly than the BCSA mortars made with the same aggregate. Despite a slight early age expansion due to ettringite formation, the expansion of these BCSA mortars is nearly 30 times lower than corresponding OPC mortars at 14 days. In a parallel study, additional alkalis in the form of 1N NaOH were added to bring the total alkali content of the cementitious mixes, expressed as Na_2O_{eq}, to $1\% \pm 0.05\%$. Even with this alkali addition to BCSA, there was no impact on the alkali-mitigating behavior of BCSA. This implies that BCSA can take on additional alkalis without causing deleterious side effects.

| (a) BCSA | (b) OPC |
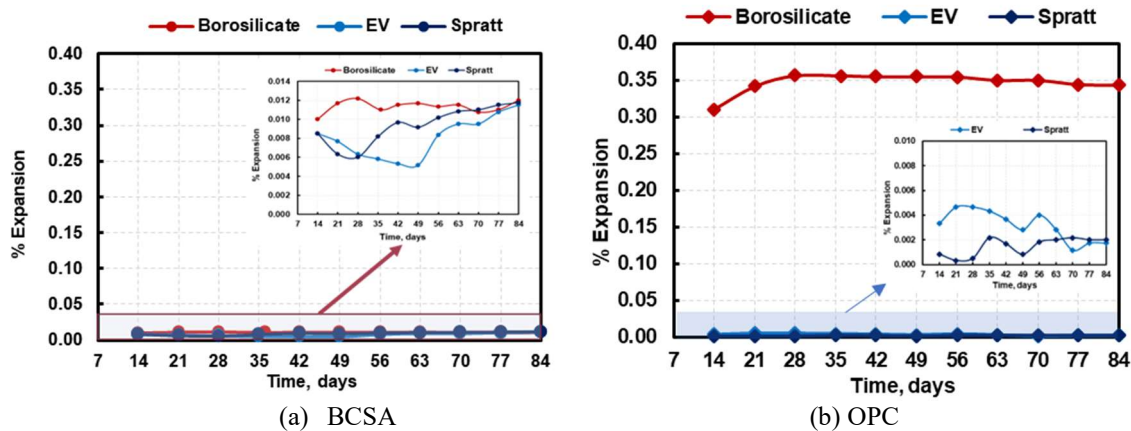
Figure 1. Expansion of mortar bars made with BCSA and OPC with aggregates of different reactivities.

The effectiveness of BCSA can be explained through the action of hydrated alumina. As demonstrated by Szeles et al. (2017), the hydrated alumina consumes $[OH^-]$ to form $Al(OH)^{4-}$. The $Al(OH)^{4-}$ ions bind with the alkalis to form non-expansive C-A-S-H gel, removing both $[OH^-]$ and alkali ions from the pore solution, which are essential for ASR. Increased water demand in the BCSA mortar to form ettringite also leaves less water for ASR. Furthermore, lower total pore volume or a higher fraction of smaller pores, or all of the above in the case of BCSA mortars, prevents the infiltration of hydroxyl ions or external alkalis that can cause ASR. The expansion of the BCSA mortars is well below 0.02%, irrespective of the aggregate used. Based on the specifications for C441 per C1600, a cementitious binder is deemed suitable when the 14-day expansion of the binder is less than or equal to the expansion of the control mix with low-alkali cement ($\leq 0.60\%$ Na₂Oe).

3.2 Findings from ASTM C1260

Figure 2 shows the expansions of BCSA and OPC mortars made with EV and highly reactive Spratt aggregates, per ASTM C1260. BCSA is more effective in mitigating ASR in moderately reactive aggregates (EV) than in highly reactive aggregates (Spratt). The internal alkali content of the mortar bar does not have any significant influence as it is immersed with alkalis while curing in 1N NaOH solution. Despite such an aggressive testing conditions, the BCSA mortars show lower ASR expansion than the OPC mortars, irrespective of the aggregate used. In the case of BCSA mortar with EV aggregate, the expansion at 14 days is nearly 1.5 times lower than with OPC. This difference grows more significant with time.
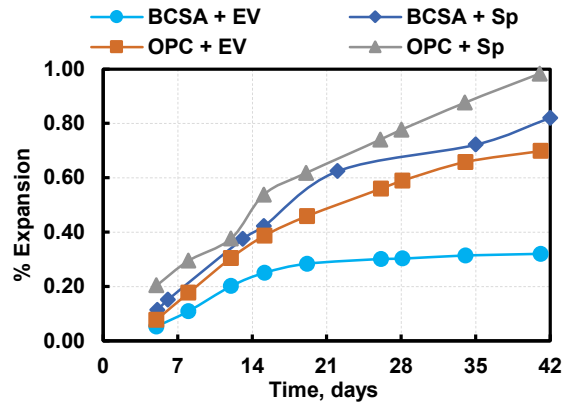
Figure 2. ASTM C1260 expansion of BCSA and OPC mortar bars made with different aggregates/

The expansion of BCSA mortars containing Spratt aggregate is nearly 1.3 times lower than that of OPC mortars with those aggregates. This difference in expansion at 14 days remains approximately the same up to 42 days. For Eagle Valley aggregate, BCSA appears to have a mitigating effect at later ages. Irrespective of the aggregate, BCSA mortars expand less than OPC mortars. It is possible that the smaller pore volume of the BCSA mortars prevents external alkalis from entering the bulk, thereby minimizing expansion of the mortar.

4. Conclusions

1. BCSA can be effective at controlling ASR. An OPC mortar containing a very highly reactive aggregate (borosilicate glass) expands 30 times more than a BCSA mortar containing the same aggregate.
2. The addition of alkali has no significant effect on the expansion of BCSA mortars, indicating that BCSA can accommodate high alkali content without significantly increasing ASR.
3. Negligible expansion is observed when Eagle Valley or reactive Spratt aggregates are used in the C 441 test. This indicates that aggregates of different reactivities can be used with BCSA compared to OPC, which may indicate that aggregate currently deemed unusable could be considered if used with BCSA.
4. ASTM C1260 expansion of OPC mortars increases linearly with age for aggregates of various reactivities. In the case of moderately reactive aggregates, BCSA tempers ASR expansion at later ages.

References

Gartner, E. (2004). Industrially interesting approaches to "low-CO2" cements. Cement and Concrete Research, 34(9), 1489-1498

Sharp, J. H., Lawrence, C. D., and Yang, R. (1999). Calcium sulfoaluminate cements—low-energy cements, special cements, or what?, Advances in Cement Research, 11(1), 3-13,

Zhang, L. (2000) "Microstructure and performance of calcium sulfoaluminate cements." Ph.D. dissertation, University of Aberdeen.

M. Thomas, The effect of supplementary cementing materials on alkali-silica reaction: a review, Cem. Concr. Res. 41 (2011) 1224–1231.

T. Chappex, K. Scrivener, The influence of Aluminum on the dissolution of amorphous silica and its relation to alkali-silica reaction, Cem. Concr. Res. 42(12) (2012) 1645–1649.

Szeles, T., Wright, J., Rajabipour, F., & Stoffels, S. (2017). Mitigation of alkali–silica reaction by hydrated alumina. Transportation Research Record, 2629(1), 15-23.

Comparative Study of Mechanical Properties of Limestone Calcined Clay Cement, Ordinary Portland Cement, and Pozzolana Portland Cement

Akash Mishra[1]*, Priyanshu Sinha[1], Amit Kumar[1] and Shashank Bishnoi[1]

[1]*Department of Civil Engineering, Indian Institute of Technology Delhi, New Delhi, India*

akdheeru@gmail.com, sinha.pkpk@gmail.com, iitd.amitkr@gmail.com, bishnoi@iitd.ac.in

Abstract

Carbon emissions from cement manufacturing are reduced by partially replacing cement clinkers with supplementary cementitious materials (SCM). In this study, Limestone calcined clay cement (LC^3) was prepared by blending 50% of OPC-43 grade with 50% Limestone calcined clay- LC^2 (63.3 % of calcined clay, 31.7% of limestone, and 5% of gypsum), Fly ash-based Pozzolana Portland Cement (PPC) and Ordinary Portland Cement (OPC) was used to compare the mechanical properties at the age of 7 & 28 days of curing for M-25 and M-50 grades of concrete. The specimens for the compressive strength test, flexure strength test, Modulus of elasticity test, and Bond test of concrete with reinforcement of 25mm diameter bars were prepared as per Indian standard codes. The results of the study showed that the LC^3 had higher compressive strength values at the age of 7 days, which is substantiated by flexure strength, modulus of elasticity, and pull-out strength values, whereas at the age of 28 days, LC^3, OPC, and PPC had similar strengths.

Keywords: *Limestone calcined clay cement, Fly ash-based pozzolana Portland Cement, Modulus of elasticity test, Bond test with reinforcement, Pull out strength.*

1. Introduction

OPC is the 2nd most consumed resource after water, and OPC is Manufactured by the process of calcination, where the heating of limestone and clay is done, which leads to the release of carbon dioxide into the atmosphere. The cement industry contributes 8% of worldwide artificial emissions of CO_2 gas, from which 50% is from the chemical process, 40% is from burning fuel, and 5-10% is emissions from electricity for plant machinery and transportation of raw materials (Rao AB, Rubin ES (2002)). With growing environmental demand for low-carbon emitting materials globally, the development of green construction materials is becoming significant in addressing the challenges of climate change. Limestone calcined clay cement (LC^3) is one such cement that has less environmental impact and excellent properties concerning strength and durability (Scrivener K. et al. 2018, Sharma M. 2021, F. Avet et al. 2019)

LC^3 is made by substituting cement clinker with limestone and calcined clay. It is expected to reduce the carbon emission of cement production by 30-40% (Berriel et al. 2016). In this experimental work, the mechanical performance of LC^3 concrete is evaluated and compared with the conventional OPC and PPC concrete.

2. Materials and methods

2.1 Materials

The three types of cement used were OPC- grade 43, PPC prepared by blending 70% of OPC 43 grade with 30 % class F fly ash, LC^3- Prepared by blending 50% of OPC 43 grade with 50% LC^2 containing 63.3 % of calcined clay, 31.7% of limestone, and 5% of gypsum. The aggregates used were crushed angular quartz stones of 20 mm and 10 mm nominal sizes, whereas the fine aggregate was river sand. The mix design of the concrete is listed in Table 1.

Table 1 Mix Design of Concrete as per IS 10262

Materials weight (kg) per m³ of concrete	OPC		PPC		LC³	
	M-25	M-50	M-25	M-50	M-25	M-50
Water Content	165.00	165.00	165.00	165.00	165.00	165.00
Cement Content	366.67	590.00	366.67	590.00	366.67	590.00
Fine Aggregate	638.45	523.87	623.19	501.49	627.41	507.67
Coarse Aggregate (10mm)	495.74	466.41	483.89	446.49	487.16	451.99
Coarse Aggregate (20mm)	743.60	699.62	725.84	669.73	730.74	677.99
Chemical Admixture	3.67	5.90	3.67	5.90	3.67	5.90

The specific gravity of cement was determined using Le Chatelier's flask as per IS 4031 Part-11, and the specific gravity of coarse and fine aggregates was determined as per IS 2386, as listed in Table 2.

Table 1 Specific Gravity of Materials

Material	OPC	PPC	LC³	Coarse (20mm)	Coarse (10mm)	Sand
Sp. gravity	3.17	2.81	3.00	2.81	2.68	2.62

Coarse aggregates were well-graded, and fine aggregates conformed to zone II of IS 383. Malvern Mastersizer 3000E was used for determining the particle size of cement. Isopropyl alcohol was used as a dispersion medium. The particle size is mentioned in Table 3.

Table 2 Particle Sizes of different types of cement

D_x	OPC	PPC	LC³
D_{10} (µm)	5.76	4.53	2.96
D_{50} (µm)	21.0	19.6	14.8
D_{90} (µm)	62.5	58.5	51.9

X-ray Fluorescence of different types of cement was done to determine the oxide composition of the cement, as mentioned in table 4.

Table 3 X-ray Fluorescence of different types of cement

Oxides Component	OPC (%)	PPC (%)	LC³ (%)
SiO_2	20.69	35.22	29.70
Fe_2O_3	5.26	5.54	3.86
Al_2O_3	4.03	12.92	19.10
CaO	59.90	34.51	32.21
MgO	0.98	1.20	1.36
SO_3	2.53	2.86	2.74
Na_2O	0.09	0.42	0.48
K_2O	0.57	0.82	0.46
TiO_2	0.40	1.09	1.39
LOI	4.30	4.10	7.90

2.2 Methods

The materials were dry mixed for two minutes; water was mixed along with chemical admixtures to obtain a homogenous mixture. The specimens for compression, flexural strength, and modulus of elasticity tests were prepared as per IS 516, whereas the pull-out strength IS 2770 part 1 was followed to prepare the specimens. The specimens were demoulded after 24 hours of the casting. Then these specimens were cured in a water tank until the age of testing.

3. Results and Conclusions

3.1 Results

The results of the study are shown in Figure 1 (a, b, and c), and the following results have been obtained.

➢ The flexural strength of LC^3 M-25, at 7 days and 28 days, was found to be higher than PPC and OPC similar trend was observed for LC^3 M-50 concrete.

➢ The 7-day and 28-day pull-out strength of OPC-M-25 specimens was more than PPC and LC^3, and the strength of LC^3 was lower than PPC at 28 days. Whereas in the M-50 grade, the strength of PPC was highest, followed by LC^3 and OPC.

➢ The results of the compressive strength and modulus of elasticity (MOE) for both grades of concrete were found to be similar, where with the increase of compressive strength, the MOE value increases, and the highest compressive strength and MOE values were observed for LC^3 followed by OPC and PPC.
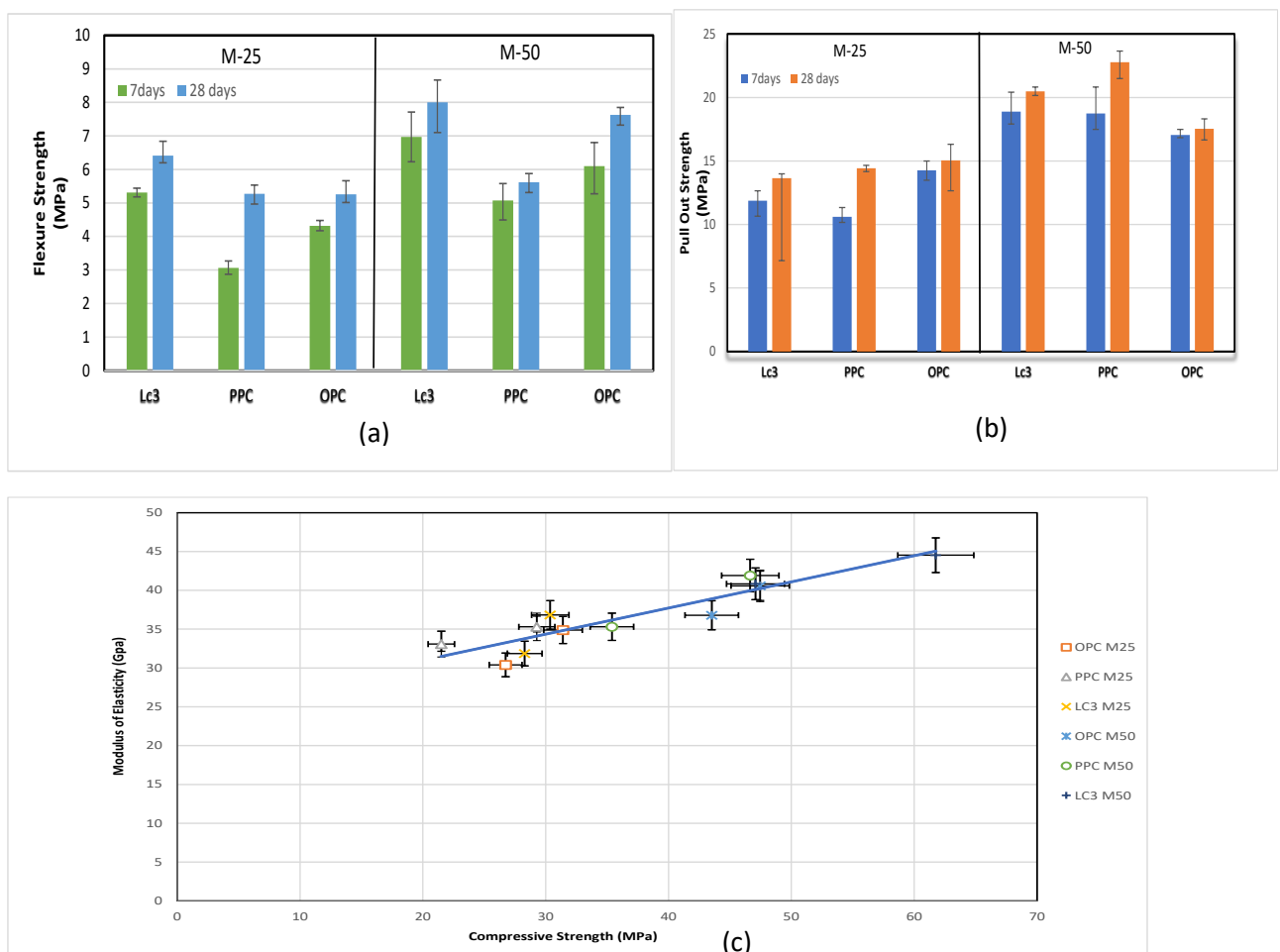
Figure 1 (a) Flexure Strength (b) Pull Out Strength (c) Modulus of Elasticity and Compressive Strength of the concrete samples at 7 and 28 days

4. Conclusions

From the results of the mechanical strengths of concrete specimens, as shown in the graph, it can be seen that LC^3 had similar strengths to OPC and PPC at 28 days, and the following conclusions were made from the study:

- ➢ The 7-day flexural and pull-out strength of the 25 mm steel bars and concrete were higher in LC^3 specimens for both grades of concrete than PPC and OPC, which signifies the high early strength of LC^3; this is because of the synergy reactions between the calcined clays, limestone and cement clinkers.
- ➢ The higher flexure, Modulus of elasticity, and compressive strength values of the LC^3 indicate that with similar mixture proportions, LC^3 binder has better strength evolution in concretes than OPC and PPC.
- ➢ The performance of LC^3 concrete in terms of mechanical parameters other than compressive strength is similar to OPC and PPC.

Acknowledgments

References

Avet, François, Lionel Sofia, and Karen Scrivener. 2019. "Concrete Performance of Limestone Calcined Clay Cement (LC3) Compared with Conventional Cements." *Advances in Civil Engineering Materials* 8(3).

Rao, Anand B., and Edward S. Rubin. 2002. "A Technical, Economic, and Environmental Assessment of Amine-Based CO2 Capture Technology for Power Plant Greenhouse Gas Control." *Environmental Science and Technology* 36(20):4467–75.

Sánchez Berriel, S., A. Favier, E. Rosa Domínguez, I. R. Sánchez MacHado, U. Heierli, K. Scrivener, F. Martirena Hernández, and G. Habert. 2016. "Assessing the Environmental and Economic Potential of Limestone Calcined Clay Cement in Cuba." *Journal of Cleaner Production* 124:361–69.

Scrivener, Karen, François Avet, Hamed Maraghechi, Franco Zunino, Julien Ston, Wilasinee Hanpongpun, and Aurélie Favier. 2018. "Impacting Factors and Properties of Limestone Calcined Clay Cements (LC3)." *Green Materials* 7(1):3–14.

Sharma, Meenakshi, Shashank Bishnoi, Fernando Martirena, and Karen Scrivener. 2021. "Limestone Calcined Clay Cement and Concrete: A State-of-the-Art Review." *Cement and Concrete Research*.

Indian Standards, Bureau *IS 10262 (2019) Concrete Mix Proportioning-Guidelines*.

Indian Standards, Bureau *IS 4031-11 (1988): Methods of Physical Tests for Hydraulic Cement, Part 11: Determination of Density.*

Indian Standards, Bureau *IS 2386-3 (1963): Methods of Test for Aggregates for Concrete, Part 3: Specific Gravity, Density, Voids, Absorption and Bulking.*

Indian Standards, Bureau *IS 383 (1970) Specification for Coarse and Fine Aggregates From Natural Sources For Concrete.*

Indian Standards, Bureau *IS 516 (1959): Method of Tests for Strength of Concrete.*

Indian Standards, Bureau *IS 2770-1 (1967): Methods of Testing Bond in Reinforced Concrete, Part 1: Pull-out Test.*

The 16th International Congress on the Chemistry of Cement 2023 (ICCC2023)
"Further Reduction of CO_2 -Emissions and Circularity in the Cement and Concrete Industry"
September 18–22, 2023, Bangkok, Thailand

Suitable solvent extraction method selection and gel structure evolution for alkali activated slag (AAS) pastes at early age

Dongdong Jiang [1], Zuhua Zhang [2], Caijun Shi [3*]

[1] *College of Civil Engineering, Hunan University, Changsha 410082, China*

Email: ddjiang@hnu.edu.cn
[2] *College of Civil Engineering, Hunan University, Changsha 410082, China*
Email: zuhuazhang@hnu.edu.cn
[3] *College of Civil Engineering, Hunan University, Changsha 410082, China*
Email: cshi@hnu.edu.cn

ABSTRACT

The selection of suitable solvent extraction method for early-age AAS samples is dependent on physical state of extra introduced silicate species, since that the liquid-state silica are inclined to react with ethanol. Before 1d of reaction time, some soluble silica from activator still exists in highly silicious AAS samples. Therefore combined solvent (water followed by ethanol) extraction is advised as the reliable method to halt reaction process and meanwhile effectively remove remanent soluble silica thus no affecting further structural characterization. Meanwhile this study also reports gel structure evolution at very early age on the basis of correct drying procedure. In general the polymerization degree of early gels increases with modulus at constant alkali dosage. In particularly some silica-rich gels are formed at final setting time in highly silicious samples. In addition the structure difference between AAS binders with varied modulus diminishes at 1d due to structural arrangement and higher degree of slag dissolution.

KEYWORDS: *AAS; modulus; solvent extraction; structure*

1. Introduction

It is commonly accepted that the reaction of slag grains in AAS is a solid-fluid reaction that follows a dissolution-precipitation-ion diffusion mechanism. In the first two reaction stages, pore solution composition determines the dissolution kinetics of slag and formation of reaction products if pore solution is saturated or oversaturated correspondingly. In the third reaction stages, the gel pores in the surrounding hydration products are the diffusion channels of ions.

It is reported that unreacted silicate species supplied by activator at early age may react with organic solvent and form high-polymerized products (Palacios et al (2021), Chen et al (2014)), when organic solvent extraction is applied to stop reaction processs. And combined extraction (solvent and combined water-solvent) was seen to reliably stop reaction without altering the reaction product (Palacios et al (2021)). However, there are no explicit recommendation for solvent extraction in respect of AAS samples with varied modulus.

The generation of "primary C-S-H" since initial setting time has been confirmed by SEM and NMR techniques (Palacios et al (2021)). It has also been reported that the exothermic peak representing precipitation of "primary C-S-H" is determined by the predominant silicate configuration in silicate solution (Jiang et al (2022).

Therefore, the paper is written aiming to (1) investigate whether drying treatment affect the nano/microstructure of AAS pastes with varied modulus; (2) if yes in the former purpose, determine the suitable drying process dependent on activator and relative timing points (3) elucidate the gels type of AAS samples especially high modulus ones. The obtained results will contribute to new sights regarding the mechanism of setting for AAS materials.

2. Materials and methods

2.1. Raw materials

Vitreous phases content in slag reach to 98.3% via Rietveld refinement method. The particle size distribution of slag determined by laser particle analyzer ranges from 1.4 μm to 148 μm, thereinto 16.11 μm is characterized as d50. Moreover the X-ray fluorescence technique is conducted to obtain chemical composition of slag, as shown in table 1, in which LOI is loss of ignition at 1000 °C. In addition, The ingredients used to manufacture activators consist of industrial-grade sodium hydroxide, raw waterglass with 64.16 wt% H_2O and SiO_2/Na_2O ratio of 3.3 and deionized water.

Table 1. Chemical compositions of blast furnace slag (by weight, %).

	CaO	SiO2	Al2O3	MgO	Fe2O3	Na2O	K2O	TiO2	SO3	LOI
wt%	38.81	33.81	14.78	7.09	0.36	0.26	0.44	0.52	2.49	1.40

2.2. Mixture design, sample preparation and treatment

Table 2 lists details of mixing proportion of AAS pastes, a constant water (deionized water and water from waterglass) to slag ratio of 0.35 is adopted to achieve satisfactory workability and almost no bleeding phenomenon. Meanwhile Alkaline activator is fabricated with Na_2O dosage of 6%, and three levels of silicate modulus of 0 (hydroxide activation system), 1 and 2 (silicate activation system). In respective of sample preparation process, the certain prepared activator is poured into mixing pot, followed by slag powders. Both of them are stirred at low speed for 120 s, subsequently a rest duration of 15s, then high speed for another 120s. Therein within the short test time of 15s, the slurry adhere to blade and wall should be scraped into pot. And all operations above are performed at ambient temperature of 20 ±1℃.

Table 2 mixture design of AAS pastes

Water /Slag	Slag (g)	Na₂O (wt%)	Modulus (Ms)	Deionized water (g)	NaOH (g)	waterglass (g)	Total water/ (slag+anhydrous activator)
0.35	100	6	0	35	7.74		0.33
			1	21.35	5.4	21.27	0.31
			2	7.7	3.05	42.55	0.30

Two kinds of drying methods are carried out in the text consisting of direct solvent extraction and combined solvent extraction, which are abbreviated hereafter as S and CS respectively. Two drying methods are described in detail as follows: In S method, 1g pastes are mixed with 100 ml ethanol. After a static placing time of 5 min, the liquid media is removed using vacuum-filtration. This procedure is repeated for three times Chen et al (2014). Then the filtered powders are immediately put into vacuum oven stabilized at 40℃ for two days for further characterization. In CS method, around 0.8 g of paste samples are firstly dispersed in 50 mL ultrapure water, then the suspensions are immediately centrifuged at a rate of 10000 r/min for 3min. This water extraction procedure above needs to be repeated until no detectable silicate species dissolves in liquid supernatant, which is verified through statement in Chen et al (2014). Subsequently ethanol extraction is performed as described in S method.

2.3. Experimental methods

FTIR method is applied to soluble residue after SAM method, 1 mg sample is ground together with 100 mg of IR-grade KBr. The resolution and scans set as 1 cm−1 and 64. Thereinto operational procedure of SAM chemical attack refers to (Yip et al (2005)).

3. Results and discussions

Figure 1 is depicted on the comparison between the direct ethanol extraction and combined solvent extraction for AAS samples with modulus ranging from 0 (sodium hydroxide solution) to 2. In the notations for the samples, CS and S indicate combined solvent extraction and direct ethanol extraction. It can be observed that both CS and S method can effectively remove water and halt reaction process, as indicated by H–O–H bending vibration of molecular H_2O around 1640cm⁻¹. And meanwhile CS treatment results in lower intensity of carbonates-related bonds in the range of 1400-1500cm⁻¹, which might be

ascribed to removed cations after water extraction. It can be observed that these two extraction ways cause no effect on sodium hydroxide activation system and direct solvent extraction results in higher polymerized species in silicate activated samples at 10min. Based on this, it can be inferred that there may exist abundant soluble silicate unites at 10min. Moreover at corresponding final setting the majority of soluble silicate unites introduced by activator are consumed and precipitate for samples with modulus no more than 2, since that almost same main peak position and spectra shape are present. But there is a nonnegligible upshift of main peaks for modulus of 2 treated with direct solvent exchange compared with combined exchange method at final setting point. And 1d are proved as reasonable time point for all samples beyond which direct solvent method can be utilized without affecting AAS binders.
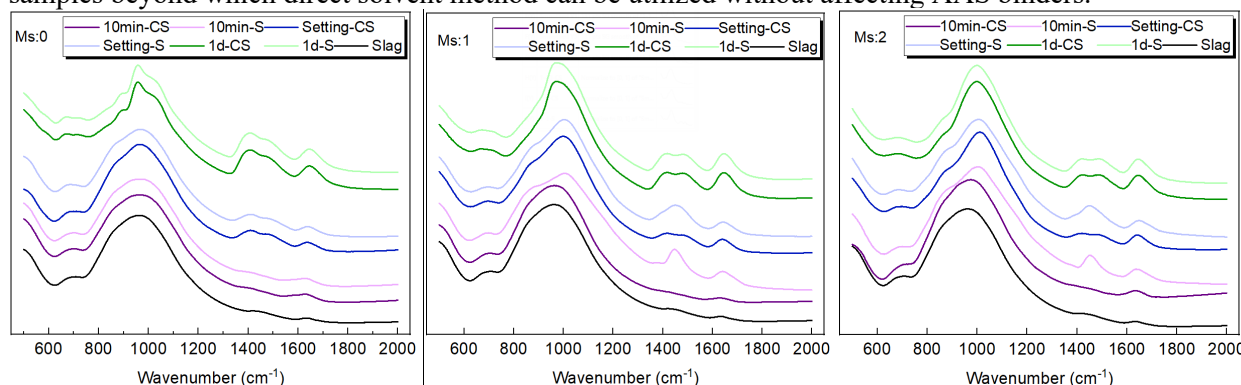
Figure 1. FTIR spectra of alkali activated slag pastes treated by two types of drying methods with alkali dosage of 6% and varied modulus. Thereinto CS and S indicate combined and direct solvent extraction respectively.

It is reported that the phases containing calcium dissolve in the salicylic acid/methanol (SAM) medium, whereas those with no calcium in their composition form an insoluble residue after the attack (García-Lodeiro et al (2009)). As shown in figure 2, regardless of modulus and investigation time, the characteristic profile of unreacted slag centering around 964 cm^{-1} can be obviously observed, which to some degree proves that SAM is a reliable method to dissolve reaction products of AAS binders. The peaks shape and position of all specimens at 10min are comparable with those of slag, indicating that phases susceptible to SAM treatment i.e. calcium-containing phases predominate at very early age such as 10min. The appearance of shoulders locating around 1058cm^{-1} and 1200cm^{-1}, frequency higher than the position of the band typical of C–S–H gels, are similar to the peaks characteristic of Q3 and Q4 silicon tetrahedra in silica gels (García-Lodeiro et al (2008)). This demonstrates that at final setting time, except for the C-(A-)S-H gels which dissolve in SAM process, a silica-rich gel with no or much little calcium in its composition may have been formed in AAS pastes activated with high modulus silicate activator. As reaction proceeds at 1d, the spectra of insoluble residue simply and the characteristic peaks prominent before are detected to decline even nearly disappear, probably because the phases assemblages are in dynamic equilibrium and calcium from slag dissolution is gradually incorporated.
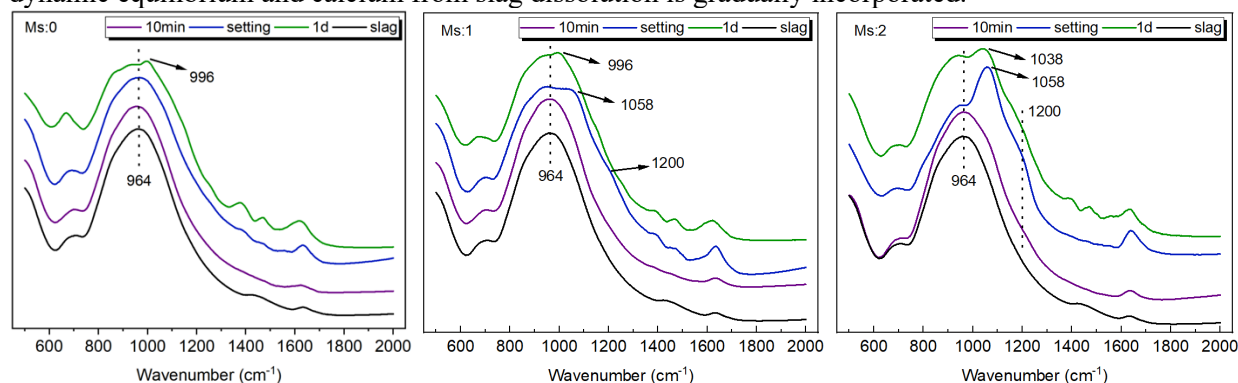
Figure 2. FTIR spectra of insoluble residue of AAS pastes after SAM attack with alkali dosage of 6% and varied modulus.

4. Conclusions

The combined extraction effectively removes soluble species and therefore provides a viable procedure to study structural changes excluding uncertainties. The modulus significantly affects timing point suitable for direct solvent exchange which is more convenient to carry on. 1d are proven to be the right point in time to utilize direct solvent extraction even for highly silicious specimens.

Besides typical C-(A-)S-H gels with main FTIR peak centering below 1000cm^{-1}, silica-rich gels are evidently formed at setting times especially in AAS pastes with modulus of 2, with characteristic band at 1058cm^{-1} and 1200cm^{-1}.

Acknowledgements

References

Palacios, M., S. Gismera, M.M. Alonso, J.B. d'Espinose de Lacaillerie, B. Lothenbach, A. Favier, C. Brumaud, and F. Puertas. (2021) "Early reactivity of sodium silicate-activated slag pastes and its impact on rheological properties", Cement and Concrete Research, 140: 106302.

Chen, X., A. Meawad, and L. Struble. (2014) "Method to Stop Geopolymer Reaction", Journal of the American Ceramic Society, 97.

Jiang, D, C. Shi, and Z. Zhang. (2022) "Recent progress in understanding setting and hardening of alkali-activated slag (AAS) materials", Cement and Concrete Composites, 134: 104795.

Yip, C.K., G.C. Lukey, and J.S.J.V. Deventer. (2005) "The coexistence of geopolymeric gel and calcium silicate hydrate at the early stage of alkaline activation", Cement & Concrete Research, 35(9): 1688-1697.

García-Lodeiro. I, D.E. Macphee, A. Palomo and A. Fernández-Jiménez. (2009) "Effect of alkalis on fresh C–S–H gels. FTIR analysis", Cement and Concrete Research, 39(3): 147-153.

García-Lodeiro. I, A. Fernández-Jiménez, M. Teresa Blanco and Angel Palomo. (2008) "FTIR study of the sol–gel synthesis of cementitious gels: C–S–H and N–A–S–H", Journal of Sol-Gel Science and Technology, 45(1): 63-72.

Case Studies on the Large-Scale use of Low-Carbon Belitic Calcium Sulfoaluminate (BCSA) concrete

Theodore Hanein [1], Julian Calleros[2] and Eric P. Bescher[3*]

[1]*Department of Materials Science and Engineering, University of Sheffield, Sheffield, United Kingdom*

Email: t.hanein@sheffield.ac.uk

[2]*Grupo Cementos de Chihuahua, Chihuahua, Mexico*

Email: jcalleros@gcc.com

[3] *Department of Materials Science and Engineering, UCLA, Los Angeles, CA, USA*

[*]*Email:bescher@ucla.edu*

ABSTRACT

Belitic calcium sulfoaluminate (BCSA) cement has been successfully used for the rapid rehabilitation of large concrete infrastructure such as runway or highway pavements. Typically, such projects require specifying rapid-strength concretes because pavement must be returned to service within a few hours of closure. For these applications, the compressive strength of the concrete should be on the order of 40 MPa in 2-3 hours under penalty of large fines for delays. BCSA is an alternative cement that is not usually familiar to the construction workforce and its use generally requires close collaboration between the cement manufacturer, specifiers, general contractors, subcontractors, and academia. For example, *ad hoc* performance specifications, approvals, concrete mix designs, and delivery methods must be developed, and this can be complex. In this paper, we describe large-scale case studies involving the use of BCSA cement concrete.

KEYWORDS: *Belitic calcium sulfoaluminate concrete, BCSA, low carbon infrastructure*

1. Introduction

Belitic calcium sulfoaluminate (BCSA) was developed in the United States in the early 70s (Ost 1975) and is from the clinker family of cements. Alite, the carbon-intensive and early-strength-imparting phase in PC, is replaced in BCSA by ye'elimite $C_4A_3\bar{S}$. Ye'elimite is much less carbon-intensive, and more efficient at providing early-strength than alite. BCSA is one of many $C_4A_3\bar{S}$-containing binders (Bescher 2020) that can be used as a single cement, i.e. not requiring blending with PC. This makes it a uniquely attractive binder for its Global Warming Potential (GWP) which, is 0.673 kg-CO_2 eq/ton (CTS 2022). An important characteristic of BCSA is that is allowed concrete mixes to reach strengths of approximately 40 MPa (compressive) or 2.8 MPa flexural at pavement opening, in 4 hours [California Department of Transportation Standard Specifications, 2022].

Rapid strength is a crucial economic incentive because it catalyzes the use of the material on short-closure time projects. Finally, compared to other low-carbon cement technologies, BCSA is compatible with established concrete placement logistics developed for PC, such as the use of ready-mix plants, silos and the flexibility cast-in-place concrete. Although BCSA has been used as concrete pavement for over 40 years in the Americas, the practice has remained somewhat below radar. An objective of this article is to briefly discuss a few selected case studies of the use of BCSA on large-scale infrastructure projects. We briefly

cover the specifics of applications in North America, including examples of large projects on the Mexico City-Querétaro highway, large repair programs on the California highway system, and runway rehabilitation at the Seattle airport, and railroad rehabilitation repair. The performance of BCSA pavement in a wet climate was also assessed after 23 years in the field at the Seattle airport.

2. Case studies

2.1 BCSA concrete on highways

The Mexico City- Querétaro highway is the most heavily trafficked highway in Mexico, at 50,000 vehicles per day. A reinforced BCSA pavement system was designed for its rehabilitation. The objective of this project was to rehabilitate large sections of the highway, typically 250 m at a time in less than 12 hours. Combining the low shrinkage (Bescher 2021) of BCSA concrete with steel reinforcement also allowed an increase in joint spacing to 200 m, which is a notable increase in joint spacing over the typical 5-6 m joint spacing in PC-based pavement. Another key aspect of this project was the large haul distance from the batch plant to the site. Citric acid and shaved ice were used as means of controlling the set time of the mix. To accommodate variations in ambient temperatures, mix temperatures were kept between 24 and 32 °C, slab thickness was 22 to 24 cm and each truck was loaded with 6 m^3 of BCSA concrete. BCSA cement content was 470 kg/m^3 and curing of the slabs required 2 hours. Total volume of BCSA concrete placed on this project was 20,000 m^3 at a rate of 250 m^3 per day.

Figure 1- BCSA concrete placement on Mexico City- Queretaru highway.

BCSA concrete is part of a program of rehabilitation of concrete highways in California. Since 1997, approximately 250,000 tons of BCSA cement have been placed on California highways. The specifications are based on a flexural strength specification of 2.76 MPa at opening time of the pavement, in addition to strength at 7 days and other performance criteria. In many US States, the cement is specified as an ASTM C1600 "Rapid Hydraulic Cement", and competes on that basis with other rapid-setting cements. Specifications in Europe or Asia are typically *ad hoc*.

2.2 BCSA concrete pavement on airports
Monterrey International Airport, Mexico

The project at Monterrey International Airport consisted of the replacement of fifteen 100 m taxilanes in the cargo area, consisting of 32 cm-thick slabs, placed at temperatures ranging from 38°C to 45°C. Specifications required a concrete achieving 48 MPa compressive in 6 hours. Haul time was 1.5 hours from the batch plant to the airport and the total volume delivered was 2,500 m^3 in 5 m^3 ready-mix trucks. Citric acid was used as a retarder, in combination with shaved ice. Citric acid concentration varied from 0.6 wt % (cement basis) at night to 1.2 wt% during the day, with 10% of the design water used as ice at night and up to 20% during the day. A total of 500 truckloads were used during the project. It was determined during the project that the concrete mix temperature should not exceed 23°C from the batch plant to the job site.

Figure 2- BCSA Concrete placement at the Monterrey International Airport, Mexico.

Seattle International Airport, United States

Approximately 30,000 m^3 of BCSA concrete have been placed at the Seattle Airport since 1997, in the overnight rehabilitation of the airport's concrete pavement (runway, taxilanes and aprons). Pavement performance after 23 years of service has been assessed. The flexural and compressive strengths of the BCSA concrete was found to have nearly doubled after 23 years in service (Deo, 2023). Concrete carbonation was measured at only 12.5 mm after 25 years. The pH of the hydrated BCSA paste was found to be 12.5 and no deleterious alkali-silica reaction was detected. BCSA was used at the Seattle airport to quadruple the size of concrete pavement and decrease the number of joints (McNerney 2021). Seattle airport remains the largest infrastructure project involving BCSA concrete at airports, but several airports in Asia-Pacific are using the cement: Melbourne Tullamarine, Sydney Hardord Smith and Lanyu in Taiwan, on which 1,200 tons of BCSA were used for runway rehabilitation.

2.3 BCSA concrete use on railroads

Mexico City-Veracruz tunnel

The 3.5 km El Mexicano tunnel on Pico de Orizaba, is the highest-altitude tunnel in Mexico. The railway track on which it is built links Mexico City to Veracruz on the Gulf of Mexico. The window of time for any repairs on the track is limited to 7 hours between train movements. BCSA concrete is currently being used for the rehabilitation of the track. During this short timeframe, a section of the track is removed, the base removed and BCSA concrete slab placed. The concrete is batched at a plant outside the tunnel and sent into the tunnel using two ready-mix trucks placed on a railroad platform. The specifications call for a compressive strength of 35 MPa at 3 hours, and 60 MPa at 28-days. Three hours after placement, a prefabricated concrete support element for the track is placed above the BCSA concrete, allowing installation of the new track and re-opening to traffic. The cement content of the concrete mix is 560 kg.m^{-3} and uses basalt aggregate while the BCSA slab is 22 cm thick. w/c was maintained between 0.40 and 0.45. At 28°C, citric acid is used at a rate of 0.6 wt % (cement basis), varying by 0.1 wt% per degree of increase or decrease in temperature. If the temperature increases to 30°C, the citric acid content is increased to 0.8 wt%, or if the temperature decreases to 27°C, citric acid addition is reduced to 0.5 wt%. Therefore, the range of citric acid use is 0.3 wt% to 0.9 wt%. Approximately 3,500 m^3 of concrete (2,500 tons of BCSA cement) have been used on this project thus far.

Figure 3- BCSA concrete placed on the Pueblo-Veracruz railway tunnel, Mexico

3. Conclusions

Case studies demonstrate that BCSA concrete mixes have been successfully used on large infrastructure rehabilitation projects. These mixes have been developed for delivery of the low-carbon concrete using either volumetric or ready-mix trucks, allowing hauling times up to one hour or more if needed. These mix designs can be adjusted to achieve the specified strength over a wide range of ambient temperatures using citric acid and/or ice. We conclude that in favorable weather/moisture conditions and with appropriate combined focus on concrete mix design, logistics, specifications, contractor expertise, experience in the field demonstrates that BCSA cement concrete can be used for large infrastructure projects.

References

California Department of Transportation, Standard Specifications, 2022

CTS Environmental Product Declaration for Rapid Set Cement, https://www.ctscement.com/assets/doc/info/EPDlabel_RapidSet_Labeling_Sustainability_CTS_Cement.pdf.
Ost B. et al. (1975) "Very High Early Strength Cement", U.S. Patent 3,860,433.
Bescher, E., Kim, J. and Vallens, K. "Belitic calcium sulfoaluminate cement: Hydration chemistry, performance, and use in the United States" (2020) Tsement, November-December 2020.

Bescher, E., Kim, J. and McNerney M (2021) On the differences in Chemistry and Performance between Rapid Strength Concretes, Proceedings of the 12th ICCP (978-0-578-33418-9), December 31, 2021, 188–194,

Deo, O., Win, D., Bhuskute, N., Chung, D. de Ocampo, N. Bescher, E., Fast Setting, Low Carbon Infrastructure Rehabilitation Using Belitic Calcium Sulfoaluminate Concrete (2022), Concrete Solutions 2022, MATEC Web of Conferences 361, https://doi.org/10.1051/matecconf/202236100002.

Deo, O., Bhuskute, N.; Bescher, E. Naga Pavan Vaddey (2022), Belitic Calcium Sulfoaluminate Concrete Runway, Concrete International 45 (2), 27-31.

Hanein, T., Galvez-Martos, J.-L., Bannerman, M.N. (2018). Carbon footprint of calcium sulfoaluminate clinker production. J. Clean. Prod. 172, 2278–2287.

McNerney, M., Kim, J.; Paniagua, F., Paniagua, J. ; Chung, D; Morgan, M.; Deo, O, and Bescher, E., Drying Behavior of a Quadruple-Sized Belitic Calcium Sulfoaluminate Airfield Concrete Slab (2021) Proceedings of International Airfield and Highway Pavements Conference, June 8-10 2021.

The 16th International Congress on the Chemistry of Cement 2023 (ICCC2023)
"Further Reduction of CO2 -Emissions and Circularity in the Cement and Concrete Industry"
September 18–22, 2023, Bangkok, Thailand

Influence of raw and mechanically activated shale on rheological properties of cement based binder

Thirumalini S[1] , Raghunathan Swaminathan[2], Shanmuga Priya T[1], Biju Karakkunnummal[2]
Gayathri Chandran[1] and Aswathy Ajayan[1]

[1]School of Civil Engineering, Vellore Institute of Technology, Vellore, Tamil Nadu, India
thirumalini.selvaraj@vit.ac.in, shanmugapriya.t@vit.ac.in,
gayathri.chandran2022@vitstudent.ac.in, aswathyajayan.s2022@vitstudent.ac.in
[2]FLSmidth Private Limited, Chennai
RSW-IN@flsmidth.com, Biju.Karakkunnummal@flsmidth.com

ABSTRACT

The abundant availability of shale across the world and its pozzolanic and hydraulic properties make it a promising SCM. Two shales CRS and SRS were collected from two different locations to study about the rheological properties of the blended cement paste. Mini-slump test was performed for optimizing the amount of water and super plasticizer for different mixes. A polycarboxylic ether based super plasticizer was used as it can actively reduce the amount of water. The rheological properties of the blended cement paste with shale were investigated using Brookefield Rheometer at a constant shear rate of 5 to 150 s^{-1}. Cement was replaced with 30% raw and mechanically activated shale and the mechanical activation was carried out by grinding in a planetary ball mill of 200rpm. The cement paste with mechanically activated shale exhibited a lower yield stress than the raw shale which shows that less energy is required to make the material flow. Yield stress shows the amount of energy needed to de-flocculate the paste and make it flow. Mechanical activation has reduced the grain size of shale thus decreasing the energy for deflocculation hence reducing yield stress. Cement paste with mechanically activated shale showed better rheological behaviour compared to raw shale mixes.

KEYWORDS: *Shale, Mechanical Activation, Rheology, Yield Stress, Thixotropic behavior*

1. Introduction

Cement production is an energy intensive process as it emits carbon dioxide into the atmosphere. It accounts for 6 to 8% of anthropogenic CO_2 emissions because of its extensive production and consumption [1]. The de-carbonation of limestone during the clinkering process is responsible for about 60% of the CO_2 produced during the manufacturing of Portland cement. Supplementary cementitious materials are materials which exhibit pozzolanic and hydraulic properties and have capability to partially replace cement [2]. The use of SCMs in place of Portland cement has already become a widely researched area in recent years. Previously many studies have been carried out on the use of ground granulated blast furnace slag, fly ash, and metakaolin as SCMs [3-5]. Among these the most commonly used SCM across the world is fly ash. Studies have shown that the resources of above mentioned SCMs are becoming scarce and are located far from cement consumers[6]. This availability issues has led to the need to explore new and novel SCMs.

Clay shale is a less explored material which has physical and chemical properties that makes them a promising SCM[7]. Shale is the most common sedimentary rock, accounting for about 70% percent of the rock in the earth's crust. Based on how it settled inside its parent rock formations, each natural shale has a unique makeup. The Calcareous Shale comprises 20–35% CaCO3 (marls and shaly chalk, 35–65%), 70–85% amorphous silica, 25–35% Fe2O3, and 70–85% siliceous shale. India's clay shale resource availability is about 34.6 million tons from 2015 the total production of shale as follows; Himachal Pradesh contributing 46%, Karnataka 23%, Madhya Pradesh 14%, Maharashtra 11%, and the

remaining 6% percent contributed by Andhra Pradesh & Telangana. Many studies have shown that SCMs replacement upto 30% can improve microstructure and overall quality of cement based materials. Studies have shown that workability and rheological properties of cement paste can be positively impacted by the addition of cementitious materials [8-10]. Fineness of materials in cement paste can positively influence the rheological properties of cement paste by reducing the yield stress values [11]. When shear forces are applied and withdrawn, cement paste reacts in a thixotropic way; agglomerated cement particles will separate under stress, causing a reduction in viscosity, but rebuild over time once the stress is removed, leading to an increase in viscosity. The fresh state of concrete depends on this reversible feature, which has attracted a lot of attention in recent years[12]. The main intention of carrying out this research as studies related to rheological behaviour of shale as SCM is very limited, how ever rheological behavioural study of shale gives idea on the viscoelastic flow behaviour of material as it is directly relaated to strength of material produced. In this study two shales, one calcium rich shale (CRS) and one silica rich shale (SRS) was collected from Kadapa region in Andhra Pradesh. CRS was collected from Dalmia cement plant in Kadapa and SRS was collected at a location far away from cement plant. The rheological properties of cement paste mixes with 30% shale will be studied. As mechanical activation proved to be an effective method in improving the efficiency of SCMs, a comparison of effect of raw and mechanically activated shale in rheology of cement paste will also be studied.

2. Materials and Methods

2.1 Materials

Ordinary Portland cement conforming to BIS specification IS:12269-1987 [13] was used. From the geological settlements of sedimentary rocks across India, two shales were identified. One CRS and SRS collected from Kadapa in Andhra Pradesh was used for the study. The chemical composition of materials used is specified in Table 1. Superplasticizer used for the study is Master Glenium SKY with relative density of 1.08 ± 0.02. Particle size, specific gravity and relative density of raw materials are shown in Table 2. As per ASTM C618 - 12a the selected shale samples has satisfied minimum 50 - 70% of primary oxides $SiO_2+Fe_2O_3+ Al_2O_3$.

Table 1. Chemical composition of raw materials

Materials	Major oxides (%)						
	SiO_2	Al_2O_3	Fe_2O_3	CaO	MgO	SO_3	Na_2O
Cement	15.67	5.21	1.25	64.21	0.78	2.67	0.23
Kadapa-Dalmiapuram Shale	47.31	11.43	6.81	14.35	1.80	0.37	0.57
Kadapa Shale	64.38	14.71	7.25	1.20	1.94	0.10	0.45

Table 2. Physical properties of raw materials

Materials	Type	Average Particle Size (μ)	Specific gravity (g/cc)	Relative Density
Cement	OPC	20.215	3.15	-
Kadapa Dalmiapuram	Raw	315.252	2.29	-
	Mechanically Activated	17.8	-	-
Kadapa	Raw	94.610	2.26	-
	Mechanically Activated	17.982	-	-
Master Glenium SKY 8233	-	-	-	1.08 ± 0.02

2.2 Methods

Raw shale and mechanically activated shale were used for making blended cement paste. Mechanical activation of CRS and SRS was carried out in a planetary ball mill of jar length 75mm and speed 200rpm with 30 zirconia balls of 10mm diameter for a time period of 120 minutes and 90 minutes respectively.
The flow behaviour of super plasticized cement paste with 30% shale has been studied using the mini-slump test created by Kantro [10]. A constant water cement ratio of 0.3 was used and super plasticizer dosage was optimized using mini slump test. The super plasticizer dosage was altered to get a flow of 12 to 13cm. AMTEK Brookfield rheometer (gap width =1 mm) coupled with Rheo 3000 software was used for the rheological experiments. For ensuring the homogeneity all the mixes were prepared without any lumps at a speed of 65 rpm for 2 minutes and placed in the rheometer plate within 60s. Shear rate was gradually increased first from 5 to 150 s^{-1} and then decreased to 5 s^{-1} in 120 load steps.

3. Results and Discussions

The flow curve was plotted using the shear stress and shear rate values obtained from the rheological studies. The values obtained were compared using Bingham model. Bingham model is the most commonly used and widely accepted model for studying the rheological behaviour of cement paste. The Bingham equation is

$$\tau - \tau_0 + \mu_p \dot{\gamma}$$

where τ, τ_0, μ_p and $\dot{\gamma}$ are considered as the shear stress, yield stress, plastic viscosity and shear rate respectively.

Fig 1 shows the shear stress vs shear rate graph of raw and mechanically activated CRS. The graph shows that when shear rate is increased the shear also increases this trend is observed due to the deflocculation of particles on the application of shear. From the graph the yield stress of mechanically activated shale is -3.92Pa and that of raw shale is -11.25Pa.As per Bingham model both raw and mechanically activated CRS showed a shear thickening behaviour with negative yield stress. Table 3 shows the flow parameters based on Bingham Model

The shear stress vs. shear rate graph of raw and mechanically activated SRS is shown in Fig.2. Since particles deflocculate when shear is applied, the graph demonstrates a trend whereby shear stress increases as shear rate increases. According to the graph, mechanically activated shale has a yield stress -17.56Pa and raw shale showed a yield stress of -38.21Pa. The negative yield stres shows that both raw and activated SRS shows a shear thickening behaviour.
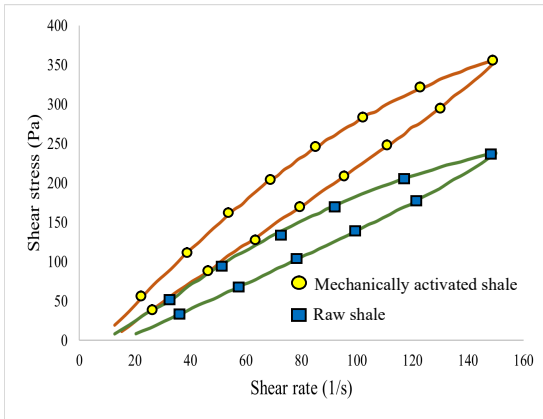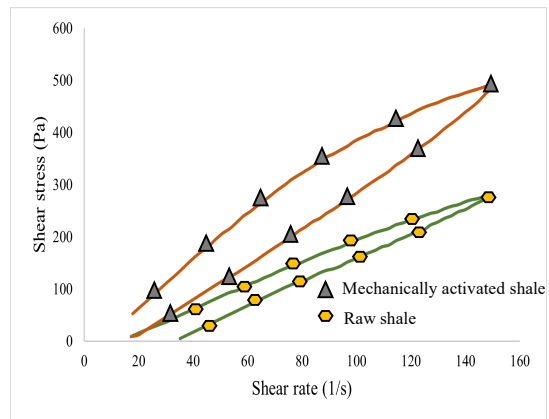
Fig. 1   Fig. 2

Fig. 1 Shear stress vs shear rate graph of raw and mechanically activated CRS
Fig. 2 Shear stress vs shear rate graph of raw and mechanically activated SRS

Table 3 Flow parameters based on Bingham Model

Shale	Shale Type	Bingham Model	
		τ_0	μ_p
CRS	Raw	3.9287	2.474
	Mechanically Activated	11.253	1.696
SRS	Raw	38.212	2.136
	Mechanically Activated	17.561	3.453

CRS had a lesser yield stress when compared to SRS this can be due to better grinding effciency and lessser particle size. Silica rich shales have higher quartz content which makes it difficult to grind due to higher hardness of quartz mineral. Both the shales showed a thixotropic behaviour due to gradual break down of the agglomorates when shear stress applied and reduced gradually [8]. The results indicated that the mixes with mechanically activated shale samples exhibited a lower yield stress than the mixes with raw shale samples which shows that less energy is required to make the material flow.

4. Conclusions

Based on the experimental study the following conclusions were drawn
- Yield stress of mechanically activated CRS was less than that of raw due to lesser particle size and more workability.
- Yield stress of mechanically activated SRS was found to be less than that of raw due to the fineness of the activated shale.
- The rheological property of both mechanically activated shales was better than that of raw shales due to the structural break down and reduction in size.
- The results indicated that the mixes with mechanically activated shale exhibited a lower yield stress than the mixes with raw shale which shows that less energy is required to make the material flow.

References

1. M. Á. Sanjuán, C. Andrade, P. Mora, and A. Zaragoza, "Carbon Dioxide Uptake by Mortars and Concretes Made with Portuguese Cements," *Appl. Sci.*, vol. 10, no. 2, p. 646, 2020.
2. Lothenbach, B., Scrivener, K. and Hooton, R.D., 2011. Supplementary cementitious materials. *Cement and concrete research*, *41*(12), pp.1244-1256.
3. Shaji, N. and Tyrer, M., 2022. Review of fly-ash as a supplementary cementitious material.
4. Oner, A.D.N.A.N. and Akyuz, S., 2007. An experimental study on optimum usage of GGBS for the compressive strength of concrete. Cement and concrete composites, 29(6), pp.505-514.
5. Bakera, A.T. and Alexander, M.G., 2019. Use of metakaolin as supplementary cementitious material in concrete, with focus on durability properties. *RILEM Technical Letters*, *4*, pp.89-102.
6. K. Scrivener and A. Favier, "Calcined Clays for Sustainable Concrete," *RILEM Bookseries*, 2015:531–537.
7. Seraj, S., Cano, R., Ferron, R.P. and Juenger, M.C., 2015. Calcined shale as low cost supplementary cementitious material. In *Calcined Clays for Sustainable Concrete: Proceedings of the 1st International Conference on Calcined Clays for Sustainable Concrete* (pp. 531-537). Springer Netherlands.
8. Park, C.K., Noh, M.H. and Park, T.H., 2005. Rheological properties of cementitious materials containing mineral admixtures. *Cement and concrete research*, 35(5), pp.842-849.
9. A. Neaman, A. Singer, Rheological properties of aqueous suspensions of palygorskite, Soil Sci. Soc. Am. J. 64 (1) (2000) 427–436.
10. A. Gadkar, K.V. Subramaniam, An evaluation of yield and Maxwell fluid behaviors of fly ash suspensions in alkali-silicate solutions, Mater. Struct. 52 (6) (2019) 117.
11. Bentz,D.P., Ferraris, C.F., Galler, M.A., Hansen, A.S. and Guynn, J.M., 2012. Influence of particle size distributions on yield stress and viscosity of cement–fly ash pastes. *Cement and Concrete Research*, 42(2), pp.404-409.
12. R. Ferron, A. Gregori, Z. Sun, S.P. Shah, Rheological method to evaluate the thixotropy of cement pastes for SCC, ACI Materials Journal 104 (2) (2007) 242–250.
13. IS:12269-1987 Indian standard code ordinary portland cement, 53 grade — specification.

The 16th International Congress on the Chemistry of Cement 2023 (ICCC2023)
"Further Reduction of CO_2 -Emissions and Circularity in the Cement and Concrete Industry"
September 18–22, 2023, Bangkok, Thailand

Changes in Rheology and Tensile Properties of UHPC with Silica Fume Content

Zemei Wu [1, 2], Kamal H. Khayat [2]*, Caijun Shi [1]

[1] College of Civil Engineering, Hunan University, Changsha 410082, PR China, Email: wuzemei@hnu.edu.cn;

cshi@hnu.edu.cn

[2] Department of Civil, Architectural and Environmental Engineering, Missouri University of Science and

Technology, Rolla, Missouri, USA, Email: kkhayat@mst.edu

ABSTRACT

High silica fume content used in UHPC can increase viscosity and render agglomeration issue, leading to entrapped air bubbles and reduced mechamical properties related with fiber cluster issues. This study investigates the influecne of silica fume content, ranging from 0 to 25%, by mass of cementitious materials, on rheological and tensile properties of non-fibrous UHPC matrix and UHPC made with 2% micro-steel fibers. Mixtures containing cement and silica fume with targeted mini-slump flow of 280 ± 10 mm were prepared. Test results showed that the highest tensile properties was found on UHPC with 10% to 15% silica fume. The tensile strengths were increased by 65% - 85% in comparirion to the reference mixture without any silica fume. This was consistent with lower viscosity and more uniform fiber dispersion and orientation. The findings from the research highlight the importance of rheology associated with raw materials to modulate tensile properties of UHPC.

KEYWORDS: *Rheology, silica fume, tensile properties, UHPC*

1. Introduction

Properly designed ultra-high performance concrete (UHPC) can deliver high flowability with self-consolidation, high strength and toughness, superior durability, and self-healing ability (De Larrard and Sedran 1994). Silica fume is a critical component in producing UHPC, which plays a significant role in affecting its overall performance due to its high amorphous SiO_2 content and fine and spherical particle size. Previous investigations indicated that the typical silica fume content used in UHPC mixture is approximately 20% to 30%, by mass of cementitious materials (Russell and Graybeal 2013). Such substitution can result in low $Ca(OH)_2$ content and porosity, improved fiber-matrix bond, and enhanced compressive and flexural strengths of UHPC (Wu et al. 2016; Chan and Chu 2014). Lower silica fume content, ranging from 5% to 15%, can be also found in some published articles, given the material characteristics and mixture proportion (Arora et al. 2018).

Depending on silica fume content and other mixture design characteristics, silica fume produces a double-edged sword effect on the performance and cost-effectiveness of UHPC. Low silica fume content can reduce plastic viscosity with limited improvement in microstructure and performance of UHPC. High substitution content can ensure sufficient pozzolanic reaction and pore refinement, but can increase viscosity. It was observed that UHPC mixture prepared with high amount of cement and silica fume is very viscous (Wu et al. 2016). This can lead to the entrapment of air voids during mixing and casting and the risk of having non-uniform fiber dispersion, and eventually reduced mechanical properties (Wu et al. 2016; Arora et al. 2018; Meng and Khayat 2017). Therefore, developing UHPC with optimal silica fume

content and appropriate rheology can lead to denser microstructure and uniform fiber dispersion to benefit mechanical properties.

The main objective of this research is to evaluate the influence of silica fume content, varying from 0 - 25%, by mass of cementitious materials, on rheological and tensile properties of non-fibrous UHPC matrix and UHPC made with 2% micro-steel fibers. The slump flows of the tested mixtures were fixed at 280 ± 10 mm to ensure self-consolidation. The findings from the research highlight the importance of rheology associated with silica fume content to modulate tensile properties of UHPC.

2. Materials and mixture design

2.1 Raw Materials

The binder materials used in this study included ASTM C150 Type III Portland cement and silica fume (SF). The mean diameter and Brunauer-Emmet-Teller surface area of silica fume are about 0.15 μm and 18,200 m^2/kg, respectively. Well-graded river sand with size range of 0 - 4.75 mm and masonry sand with size in the range of 0 - 2 mm with specific gravities of 2.64 were used. Straight brass-coated steel fibers with a diameter of 0.2 mm and a length of 13 mm were used. They show tensile strength and elasticity modulus of 1.9 and 203 GPa, respectively. A polycarboxylate-based high-range water reducer (HRWR) with a solid mass content of 23% was incorporated.

2.2 Mixture proportion

Non-fibrous UHPC matrix and UHPC with 2% steel fibers were employed in this study. The mixtures had a fixed water-to-binder ratio (w/b) of 0.18 and a sand-to-binder ratio of 1.0. Five silica fume contents, varying from 0 to 25%, were employed. The HRWR dosage was adjusted to obtain a mini-slump flow of 280 ± 10 mm as measured with the mini-cone test without any jolting. The six UHPC mixtures incorporating 0, 5%, 10%, 15%, 20%, and 25% silica fume were designated as SF0-2, SF5-2, SF10-2, SF15-2, SF20-2, and SF25-2, respectively.

2.3 Specimen preparation

All mixtures were prepared using a Hobart mixer at room temperature. UHPC dog-bone specimens made with 2% steel fibers were cast from one end of the mold. The mixture was naturally flowed to the other end of the mold to ensure natural-oriented fibers without any intervention. All the specimens were cast and demolded and then cured in lime-saturated water at room temperature of 20 ± 2 °C and 95% relative humidity until testing age of 28 d.

3. Testing methods

3.1 Rheological Properties

A ConTech 5 coaxial cylinders rheometer was employed to determine yield stress and viscosity of the UHPC matrix and UHPC. Typically, the measurements began at 10 min after water addition with samples subjected to pre-shear at a rotational velocity of 0.50 rps for 35 s followed by seven steps of decreasing rotational velocities at a step duration of 5 s. The yield stress and linear term (viscosity) were determined through applying the modified Bingham model given the fact that the majority of the flow curves were non-linear.

3.2 Tensile behavior

Direct tensile testing was conducted using big dog-bone specimens measuring 25 mm in thickness and 526 mm in length with a narrow neck width and length of 50 and 175 mm, respectively. Load frame with a capacity of 250 kN was used to conduct the tensile tests at a displacement rate of 0.5 mm/min. Each end of the specimen was held by a fixture gripped on the load frame using a ball hinge connection. Extension

of the specimen was obtained from two linear variable differential transducer (LVDTs) attached to the frame over a gage length of 160 mm. Three specimens were averaged for each mixture.

4. Results and discussion

4.1 Rheological properties

Fig. 1 shows the yield stress and viscosity (linear term of the modified Bingham model) of the investigated mixtures. The yield stress, minimum stress to initiate the flow of the UHPC matrix, was ranged between 34 and 41 Pa at a fixed mini-slump flow of 280 ± 10 mm. The incorporation of 10% - 15% silica fume reduced the lower viscosity. Besides, the incorporation of steel fibers further increased the yield stress and viscosity to 70 - 80 Pa and 48 - 85 Pa.s, respectively. This is because the increased resistance to flow associated with interlocking effect between steel fibers and surrounding particles, thus increasing the viscosity of UHPC (Khayat and Roussel 2000).
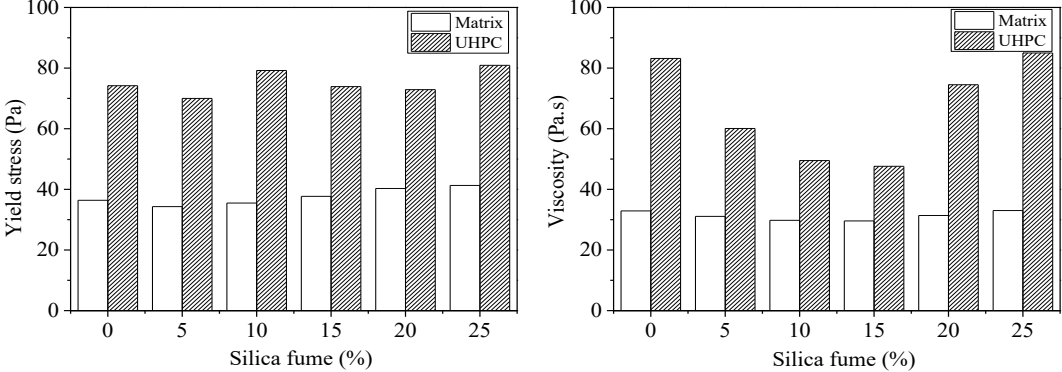
Figure 1. Change in rheological properties of UHPC matrix and UHPC with silica fume content: (a) yield stress; (b) viscosity.

4.2 Tensile behavior

Figure 2(a) illustrates the tensile load-extension relationships of UHPC mixtures made with different silica fume contents, and Figure 2(b) shows the calculated tensile strengths. The tested mixtures exhibited linear tensile load-extension behavior up to the peak load at a small extension of 0.01 mm, followed by gradually decreasing branch. With the increase of silica fume content up to 10%, the tensile strength increased before exhibiting some drop. The use of 10% - 15% silica fume enhanced the tensile strengths of the UHPC matrix and UHPC by 100% - 150% and 65% - 85%, respectively, compared to the reference mixtures. The tensile strength of the UHPC made with 25% silica fume was slightly greater (approximate 1 MPa) than that without any silica fume. This agrees well with the previous rheological results.
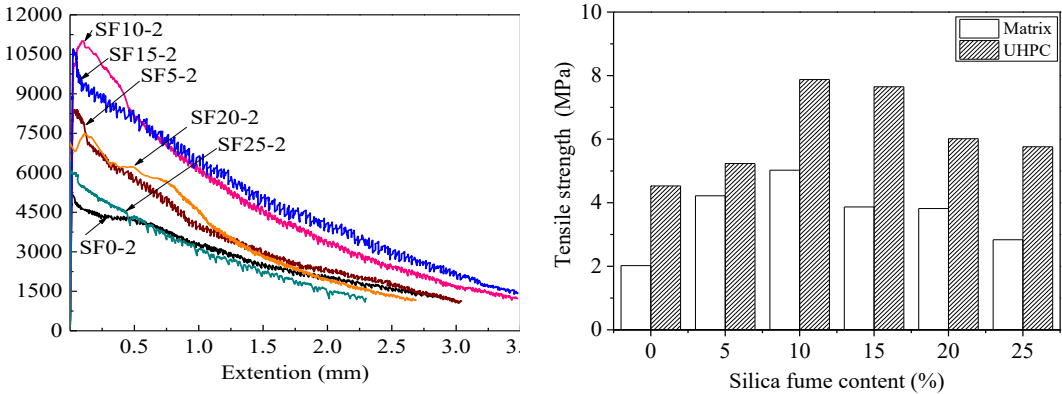
Figure 2. Tensile properties of UHPC: (a) load-extension relationships; (b) tensile strength.

5. Conclusions

The following conclusions can be drawn based on the results from this research:

(1) The HRWR demands for the non-fibrous matrix and UHPC at a fixed mini-slump flow decreased initially with the increase of silica fume content and then increased with further addition of silica fume. The HRWR demands were 2% to 3% and 4% to 8% for the matrix and UHPC, respectively. The incorporation of 10% - 15% silica fume resulted in lower viscosity in comparison with other mixtures.

(2) The optimal silica fume content for tensile properties of UHPC was found to be 10%-15%. Compared to the reference mixture, the tensile strengths of the optimized UHPC mixtures were enhanced by 65% - 85%. This is attributed to uniform fiber dispersion and orientation as confirmed by visual observation of the tensile cracking path during eperiment.

Acknowledgements

References

Arora, A., Aguayo, M., Hansen, H., Castro, C., Federspiel, E., Mobasher, B., Neithalath, N. (2018). Microstructural packing-and rheology-based binder selection and characterization for Ultra-high Performance Concrete (UHPC). Cement and Concrete Research,103, 179 - 190.

Chan, Y. W., Chu, S. H. (2004). Effect of silica fume on steel fiber bond characteristics in reactive powder concrete. Cement and concrete research, 34(7), 1167 - 1172.

De Larrard, F., Sedran, T. (1994). Optimization of ultra-high-performance concrete by the use of a packing model. Cement and concrete research, 24(6), 997 - 1009.

Khayat, K. H., Roussel, Y. (2000). Testing and performance of fiber-reinforced, self-consolidating concrete. Materials and Structures, 33, 391 - 397.

Meng, W., Khayat, K. H. (2017). Improving flexural performance of ultra-high-performance concrete by rheology control of suspending mortar. Composites Part B: Engineering, 117, 26 - 34.

Russell, H. G., Graybeal, B. A., Russell, H. G. (2013). Ultra-high performance concrete: A state-of-the-art report for the bridge community (No. FHWA-HRT-13-060). United States. Federal Highway Administration. Office of Infrastructure Research and Development.

Wu, Z., Shi, C., Khayat, K. H. (2016). Influence of silica fume content on microstructure development and bond to steel fiber in ultra-high strength cement-based materials (UHSC). Cement and Concrete Composites, 71, 97-109.

The 16th International Congress on the Chemistry of Cement 2023 (ICCC2023)
"Further Reduction of CO2 -Emissions and Circularity in the Cement and Concrete Industry"
September 18–22, 2023, Bangkok, Thailand

Understanding the Effect of Slag Particle Size, Shape, and Morphology on the Flow Characteristics of Portland Cement - Blast Furnace Slag Blends

A. Sjoberg[1]*, G. M. Cann[3]*, D. A. Geddes[1,2], J. L. Provis[2], B. Walkley[1]

[1] *Department of Chemical and Biological Engineering, University of Sheffield, United Kingdom*
Emails: amsjoberg1@sheffield.ac.uk, d.geddes@sheffield.ac.uk, b.walkley@sheffield.ac.uk
[2] *Department of Materials Science and Engineering, University of Sheffield, United Kingdom*
Email: j.provis@sheffield.ac.uk
[3] *National Nuclear Laboratory, Workington, United Kingdom*
Email: gavin.cann@uknnl.com

ABSTRACT

Where cementitious grouts are used to encapsulate intermediate level waste, supplementary cementitious materials (SCMs) such as ground granulated blast furnace slag (GGBS) are introduced in high quantities to Portland cement (PC). This blend can be used to produce high fluidity, low bleed grouts, with a suitable low heat evolution during the curing process. These formulations also have the benefit of enhancing longer-term physical properties such as strength, durability and reduced permeability, while GGBS as a by-product of iron production, provides the added benefit of reducing the grout embodied carbon.

Although GGBS is used widely on waste encapsulation plants, not all sources of civil construction industry grade GGBS produce grouts with the properties required for use in encapsulation grouts. The addition of superplasticiser admixtures may allow the use of otherwise unsuitable GGBS supplies in encapsulation grouts and may also improve the grout performance. However, there is little understanding of what physicochemical parameters of GGBS are critical to reliable performance in blended grouts when used in conjunction with superplasticisers.

The work reported here is an initial assessment of commercial GGBS sources produced via a variety of grinding techniques to provide baseline information on the GGBS properties which affect grout performance in non-superplasticised grouts. Different grinding technologies produce GGBS powders with different particle morphologies and thus, it is important to understand how morphology affects the fluidity and workability of a blended grout. An initial assessment of particle size, shape, and morphology of four GGBS is correlated with slump data. The overall aim of this research is to determine the resultant effect on grout flow characteristics and workability in order to establish a relationship between the physical characteristics of the grout and its performance as an encapsulant. This insight helps to reveal fundamental processes controlling dispersion, fluidity and workability of PC-GGBS grouts, providing better understanding of key parameters for robust specification which lays the foundations for further novel research surrounding the interactions between civil-grade GGBS and superplasticisers.

KEYWORDS: *Blended Portland Cement, Ground Granulated Blast Furnace Slag, Wasteforms, Flow Characteristics*

1. Introduction

Cementitious materials are used within the nuclear industry in the UK to encapsulate and immobilise intermediate level waste (ILW). The purpose of this is to produce a passive wasteform that is safe to handle, store and transport during the interim before the waste package (wasteform and container) is disposed of permanently in a geological disposal facility (GDF).

The encapsulation grout must satisfy certain properties and characteristics to ensure effective immobilisation; this paper will focus on the following:

• High fluidity to ensure the highest level of waste infiltration considering complex waste geometry.
• Low water-solids (w/s) ratio to ensure relatively low permeability in cured grout. This reduces the risk of shrinkage cracking of the grout. Low w/s also potentially minimises waste corrosion, gas generation

due to waste/grout interactions or radiolysis of water, and the chances of bleed during the formation of the wasteform.

- Relatively low heat evolution during hydration reaction (occurs between water and cement during curing process) to avoid high temperatures after grout pour. This also aids with minimising the likelihood of shrinkage cracking.
- Predictable characteristics to ensure consistent and reproducible performance, and minimise leaching of radionuclides.

To facilitate the above desired characteristics of the encapsulation grout, supplementary cementitious materials (SCMs), in this case ground granulated blast furnace slag (GGBS), are added to the Portland cement (PC). To minimise grout performance variability and enhance properties, strict parameters have traditionally been applied to all components of the grout, and therefore the nuclear industry has used bespoke powders meeting more stringent standards than those applied in civil construction (Angus et al., 2011). For example, variation of physical characteristics, such as shape and size, of the PC and GGBS particles on a microscale can drastically change characteristics such as fluidity, early strength and setting time (Reformat and Ludwig, 2014).

The cement industry is under increasing pressures to reduce greenhouse gas emissions associate with PC manufacture. (Angus et al., 2010). The resultant changes to the manufacturing process may alter the properties of the PC meaning that the powder may not meet the specifications required for encapsulation of nuclear materials. Similar considerations are true for GGBS. To address the challenge of security of supply, civil construction grade powders that meet British and European (BS EN) Standards are being considered.

This research aims to understand the physical properties of civil-grade GGBS and the effect on the workability of the blended grout. Specifically, this conference paper will focus on the effect of GGBS particle size, shape, and morphology on the flow characteristics of blended PC grouts for use as radioactive waste encapsulants. The outcomes of this preliminary research will provide the baseline data before further research to see if grout performance can be improved by the use of cement additives such as superplasticisers.

2. Mix Design

The performance of four different commercial sources of GGBS powder which were ground using varying grinding mechanisms were assessed (Table 1). These were blended with CEM I (also used as the Sellafield Ltd. standard), taken from a single source for all formulations. All formulations were prepared with a 50:50 (w/w %) GGBS/CEM I powder blend at 0.5 w/s. To respect supplier confidentiality, all sources of GGBS and CEM I have been anonymised.

Table 1: GGBS Grinding Mechanisms

GGBS Sample	Grinding Technology	Granulate Source
GGBS 1	High Pressure Grinding Roll (HPGR)	Blastfurnace on site
GGBS 2	Vertical Roller Mill (VRM)	Blastfurnace on site
GGBS 3	Ball Mill	Blastfurnace on site
GGBS 4	VRM or Ball Mill	Imported – multiple sources

2.1 Sample Preparation

Grouts were prepared in a room temperature laboratory. Grouts were mixed at 500 rpm for 10 minutes. Scanning Electron Microscope (SEM) stubs were prepared in sterile microchemistry laboratories and gold coated.

2.2 Method

Scanning electron microscopy (SEM) was undertaken using a Jeol JSM-6010LA. All images were taken at 15 kV accelerating voltage. Grout fluidity was measured using a standard mini-slump cone (top diameter: 19 mm, bottom diameter: 38 mm and height: 57 mm) procedure (for 3 repeats) where grout spread measurements were taken immediately after initial mixing at t_0. Particle size distribution (PSD) analysis was carried out using a Malvern Panalytical Mastersizer 3000 laser diffraction instrument.

3. Results and Discussion

Table 2: Mini Slump Data – Mean Diameter of Slumped Grout (D) in order of decreasing slump (Left to Right)				
GGBS	GGBS 3	GGBS 4	GGBS 1	GGBS 2
Mean Slump (mm)	85.30	84.56	80.26	68.02

The mean slump data (Table 2) shows that GGBS 3, which was ground using a ball mill, had the largest slump and that GGBS 2, which was ground using a vertical roller mill, has the smaller slump.
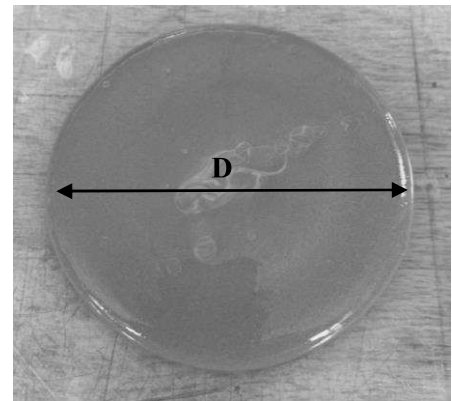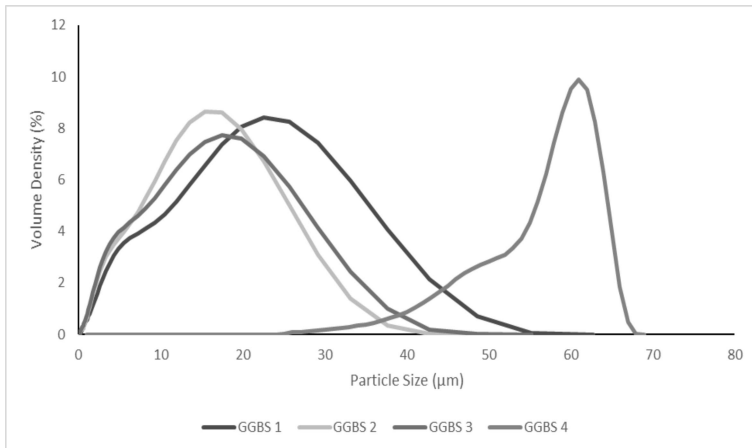
Left: Figure 1: A graph to show the PSD data for all GGBS samples. Right: Fig 2: Mini-Slump Test

It would be expected that the samples with a larger proportion of the smallest particles would have the smallest slump due to the larger surface area to volume ratio increasing water demand. When comparing the PSD data in Figure 1 to the mini-slump data, it can be seen that GGBS 1, 2 and 4 followed a trend of higher slump diameter for coarser PSDs, however GGBS 3 which gave the highest slump did not follow this trend suggesting there are other physiochemical properties influencing the flow characteritics.

GGBS 4 has PSD data of particular interest. The majority of the bulk of particles within GGBS 4 sample have a size of around double that of other samples, as shown by the strong peak at 61 μm. Although this GGBS has the widest range of particle sizes, the majority of the particles are sized between 30 and 70 μm.
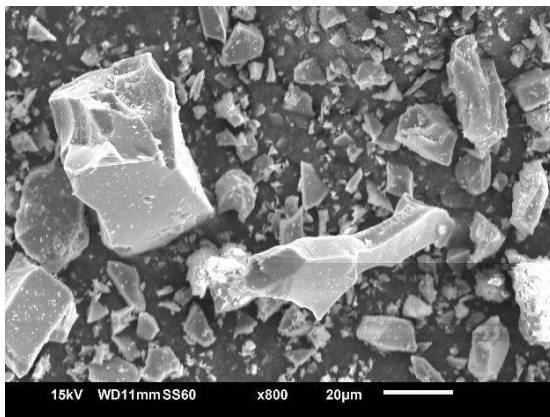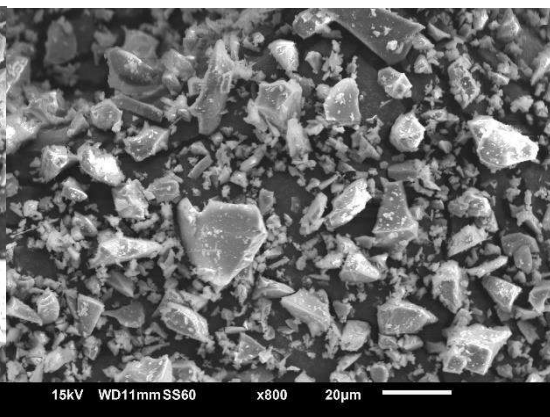
Figure 3: GGBS 1 (HPGR)   Figure 4: GGBS 2 (VRM)
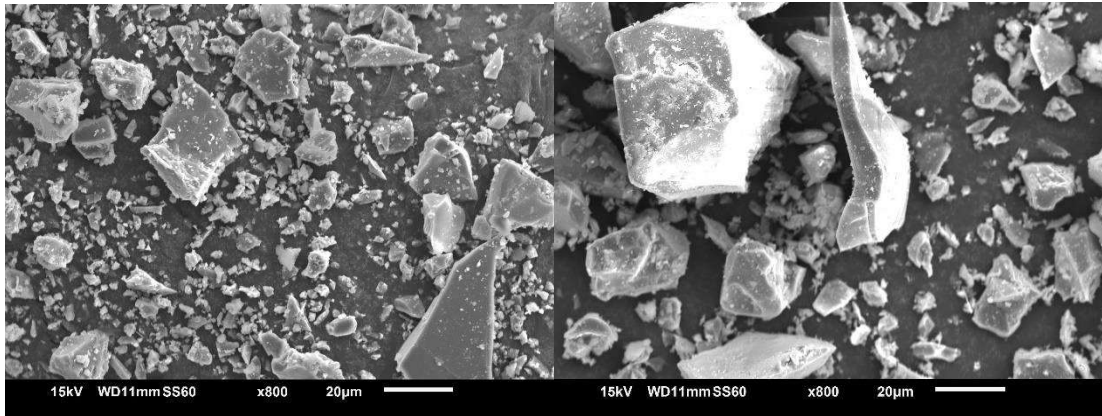
Figure 5: GGBS 3 (Ball Mill)   Figure 6: GGBS 4 (VRM or Ball Mill)

The SEM output (Figure 3 to Figure 6) shows a variety of different particle morphology; all images show the samples at ×800 magnificaiton.

The particles in GGBS 1 are generally longer and thinner, whereas GGBS 2 exhibits smaller and more consistently sized particles. GGBS 3 has generally smaller and flatter particles with a few larger particles present. GGBS 4, however, exhibits lots of large particles, visibily much larger than all other samples. This qualititive analysis can be coherantly compared to the PSD data.

All samples are ground using different techniques and each sample's particle morphology varies considerably. This suggests that the grinding mechanism does influence the particle morphology.

5. Conclusions

- The grinding mechanism used to grind slag to GGBS influences the particle size and morphology.

- The particle size and morphology, influenced by the grinding mechanism, affects the flow characteristics of a grout.

- There are other physiochemical properties influencing the flow characteristics of a grout which cannot be identified from the scope of this paper.

6. Future Work

Chemical properties which could work in conjunction with physical properties to influence the flow characteristics of a blended PC grout will be investigated. Methods such as zeta potential analysis will be undertaken to investigate electrostatic interactions. Further analysis surrounding physical properties such as particle shape and surface area will be conducted to understand the trends identified in this paper. These findings can then be used to understand GGBS interactions with cement additives such as superplasticisers in blended grouts.

7. Acknowledgments

References

M. Angus, J. Borwick, G. Cann, M. Hayes, B. McLuckie and J. Jowsey, (2011) "The Specification of Cement Powders for Waste Encapsulation Processes at Sellafield Site," in Proceedings of Nuwcem 2011 Conference, Avignon, France, 2011.

Reformat, M. Ludwig H M (2014) "Influence of Different Grinding Devices on the Reactivity of Ground Granulated Blast Furnace Slag" published in the *Chemical & Engineering: Comminution and Classification Volume 37, Issue 5*. Weinheim, Germany. Pages 891-894.

Angus, M J. Godfrey, I H. Hayes, M. Foster, S. (2010). "Making Change in the Supply of Cement Powders for Radioactive Waste Encapsulation – Twenty Years of Operational Experience" in Proceedings of WM2010 Conference 2010, Phoenix, AZ.

Sacrificial agents for clayey aggregates. An understanding of mortar and concrete scale

A.C. Gómez[1*], W.A. Echeverri[2], C.A. Orozco[3], C.P. Rodriguez[4]

[1] *Cementos Argos, Medellin, Colombia*
agomezgo@argos.com.co
[2] *Cementos Argos, Medellin, Colombia*
wecheverri@argos.com.co
[3] *Cementos Argos, Medellin, Colombia*
corozco@argos.com.co

[4]*Cementos Argos, Medellín, Colombia*
crodriguro@argos.com.co

ABSTRACT

Nowadays, clay on aggregates is one of many challenges facing the concrete industry due to the high affinity between the polycarboxylate superplasticizer (SP) technology that affects the concrete performance in the fresh and hardened state. The use of aggregates contaminated with clay is limited, so from a sustainability perspective, finding a solution that promotes its use and reaches the desired performance is a need. One of the solutions available to mitigate water demand and admixture dosage for cement dispersion is using sacrificial agents. Two types of commercial sacrificial agents were tested at mortar and concrete, identifying the potential adjustments for two types of clayey fractions in sands available for ready-mix production. First, XRD and TG for the sand (NS1) suggest kaolinite and illite clay presence (T-O type) on the fine sand fraction. At the same time, the second sand (NS2) was identified as smectite-type clay (T-O-T type).

For the equivalent mortar test following the ASTM C 1810 water reduction, and superplasticizer dosage optimization were tested at different dosages for clay mitigators, measuring the impact on workability, and mix aspect. One main finding of this study suggests that sacrificial agents could be as specific as the type of clayey fraction on the sand and could be limited based on sand availability. On the other hand, the amount of sacrificial agent required to keep water demand under control and SP dosage just for cement dispersion is higher (0.3 %-0.7 % w/w of sand proportion) despite the low amount of clayey fraction, which could impact around 30 % of the concrete cost and just a cement reduction about 6% of total cement content.

KEYWORDS: Polycarboxylate Superplasticizer, clay, aggregates, cement-based materials, sacrificial agent

1. Introduction

The use of superplasticizer admixtures in the production of concrete has enabled the development of products with high workability, as well as concretes with low water-cement ratio (a/c), self-compacting properties, and high-performance concretes with excellent durability performance (Ramachandran, 2002). Polycarboxylate technology changed the way of thinking about concrete production and defining new design strategies and new properties for concrete mixes. However, some authors such as Ng et al. (2012), Norwell et al. (2007), Muñoz et al. (2010), Ma et al. (2020), and Jardine et al. (2003) have noted that this type of technology responds poorly in the presence of clayey fractions in the binder or in the aggregate as impurities, which is associated with a high-water demand and a reduction in compressive strength, poor workability, and an increase in admixture dosage.

Based on these findings, tests were conducted on mortar and concrete to determine the advantages and disadvantages of two commercial sacrificial agents to identify the benefits-oriented to maintain concrete performance while using less cement content to lower CO_2 emissions.

2. Materials and methods

The cement type used in mortar and concrete reaches 45 MPa at 28 days. Two sources of sand samples were chosen for this study where one is an alluvial source (NS1), and the second sample is natural sand (NS2) from igneous rock. A second sample for the NS1 mine, CF-NS1 was examined to get a rejected material rich in clayey fractions that support the clay identification.

The XRF oxide components were evaluated using Axios Panalytical and the XRD patterns were assessed using Panalytical X'Pert PRO. The grading curves using the ASTM C 33 protocol. The specific gravity and absorption percentages were calculated using ASTM C 128. Two methods for methylene blue values: ASTM C 1777 for sand passing sieve # 4 and INV- 235-07 for the fine fraction, passing sieve 75 microns. Two commercial sacrificial agents M1 and M2 defined as Polyamine-based material were tested at different dosages in a mortar (ASTM C 1810) and concrete slump loss and compressive strength at 3 days, 7 days, and 28 days.

3. Results and discussion

The chemical composition of the cement, NS1 (Natural Sand 1), CF-NS1, and NS2 (Natural Sand 2) are in Table 1. The LOI for cement corresponds to a material with minimal limestone substitution and the addition of a reactive pozzolan to ensure early strength development.

Table 1. XRF data for cement, NS1, CF-NS1, NS2

	SiO_2	Al_2O_3	Fe_2O_3	MgO	CaO	Na_2O	K_2O	SO_3	LOI	XRD Identification**
Cement	22.77	5.04	3.3	2.39	59.05	0.01	0.39	2.76	4.08	N.M
NS1	69.1	13.5	4.1	2.7	4.3	2.3	0.84	0.1	2.3	Q ++, A ++, Cl-
CF-NS1	49.1	16.9	8.4	4.8	5.5	2.3	1.4	0.4	9.3	Q +, A +, (K, I; N) +
NS2	51.06	14.55	9.99	5.51	6.89	3.89	0.69	0.06	4.94	V ++, Cl-, ++, I,+Q+, An+

** Cl: chlorite, I: illite, K: kaolinite, N: nacrite, H: hornblende, Q: quartz, A: albite. Cl: chlorite, V: Vermiculite, An: Anorthite.
N.M not measured

Figure 1a depicts two images of NS1(left) and NS2 (right); large particles and irregular shapes are distinguished in NS1, as quartz and high muscovite content can also be identified. The geology of the extraction zone for NS1 suggests that it is possible to find clay minerals such as kaolinite and illite identified on the XRD pattern.

N2 is specifically extracted from the felsic portion where minerals such as plagioclases, feldspar, hornblende, biotite, and possible chlorite and clays are found. XDR identification suggests low quartz and anorthite content, and the presence of vermiculite minerals, chlorite, and illite. Visually, NS2 has a higher proportion of fines but fewer high-shape aggregates than NS1. Grading curves for NS1 and NS2 that adhere to ASTM C 33 are depicted in Figure 1b.
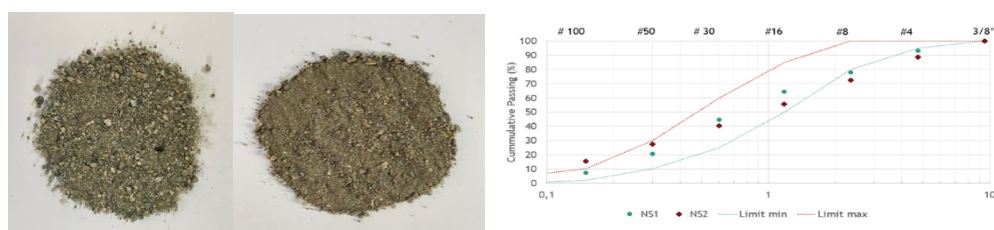
Figure 1. 1a. Images for NS1 (left) and NS2 (right).**1b**. Grading curves for NS1 and NS2.

Table 2 summarizes the basic characterization in accordance with ASTM C 128. The values for NS1 and NS2, which are related to specific gravity and absorption are normal for sand. It is worth noting that NS2 has a higher passing sieve # 200 than NS1 and MBV as well. Furthermore, CF-NS1 from the sand deposit for NS1 had the highest MBV for passing sieve # 200 and the lowest specific gravity, which could be attributed to the presence of clay.

Table 2. Basic aggregate characterization

	Specific Gravity	Absorption (%)	Passing Sieve # 200	MBV (g dye/g sample)	MBV-S200 (g dye/g sample)
NS1	2.63	1.64	3.79	1.46	3.56
NS2	2.67	1.26	6.40	2.57	7.63
CF-NS1	2.02	--	--	--	15.75

The corresponding mortar test is shown in Figure 2a. The test was performed with NS1 and the sacrificial agent M1 at dosages of 0.50%, 0.55%, and 0.60% (w/w of sand), while M2 was applied at doses of 0.40%, 0.50%, and 0.60% (w/w of sand). For the reference mixes the mini-slump retention was roughly 85% and all mixes using M1 got slump retention higher than the reference mix and 12% of water reduction. The same results were obtained for M2 with better slump retention than the reference mix and water reduction of about 25%.
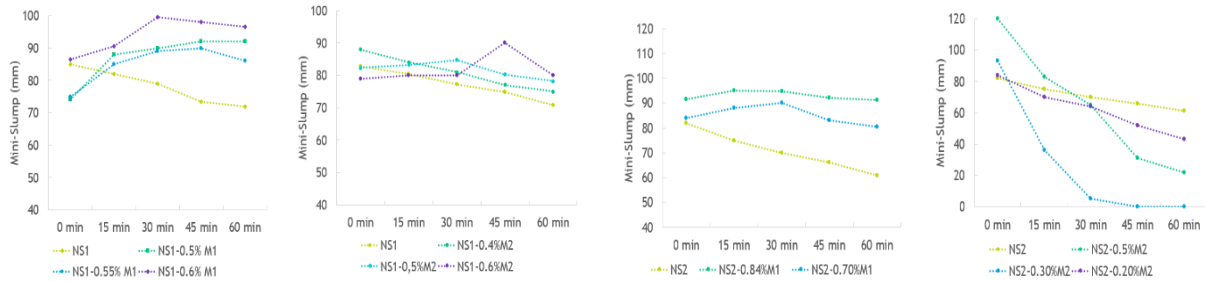
Figure 2. 2a. Slump Loss test for NS1 with M1,M2 (Left). **2b**. NS2 with M1,M2 (Right)

Results for NS2 with M1 and M2 are shown in Figure 2b. M1 molecule had better mini-slump retention than the reference mix, with a water reduction of about 11%. M2 sacrificial agent exhibits a poor response at high and low dosages; due to 28% water reduction, this lack of water directly affects the slump loss of the system. Despite both commercial sacrificial agents being polyamine-based components, Ma et al., (2020) suggest that the molecular weight, the cationic molecule charge, and the clay present on the sand may all have an impact on the chemical and/or physical adsorption.

The dose sensitivity at the equivalent mortar test was used to conduct concrete studies for NS1 with M1 and M2, as well as NS2 with M1. Figure 3a and 3b summarizes the results with NS1 and M1 and M2. In Figure 3a at 0.5 (w/w sand) slump retention of 94% and a water reduction of 7%, the compressive strength increased by 24% after 28 days. Figure 3b, for M2 at 0.40% (w/w of sand) showed 33% strength improvement after 28 days and slump retention of 94% with 15% water reduction. When comparing M1 and M2 for the sand NS1, both sacrificial agents reduce water on their mixes and ensure slump retention: however, the amount of water that each sacrificial agent can reduce may be related to the amount of cement that can be reduced.
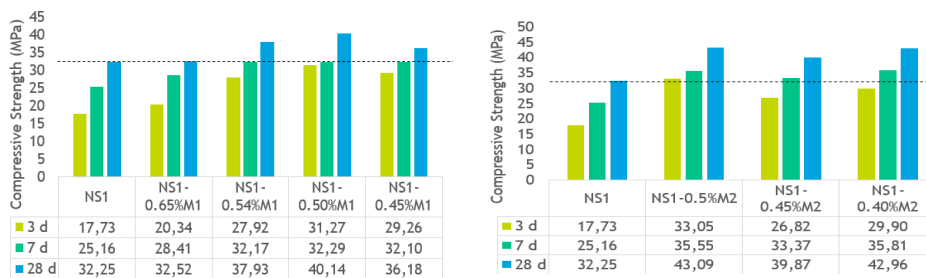
Figure 3. 3a Concrete test NS1- M1 sacrificial agent. **3b**. Concrete test NS1- M2 sacrificial agent.

NS2 To achieve better slump retention while reducing 15% of water content, using M1 was required from 0.50 %-1.0 % (w/w sand) and 33% strength gain after 28 days was obtained. M1 sacrificial agent could be effective in both grains of sand proposed in this study at different dosages that could be related to the amount of MBV of each sand and guarantee a potential cement adjustment while maintaining the same performance.

In addition, a cement reduction test for NS1 and M2 from 15 kg to 25 kg test and is shown in Figure 4. For all scenarios examined, the slump retention was higher than the reference mix. For 0.45% M2-15 kg and 0.45% M2-20 kg, the slump retention was 85% and 88% with a slight gain of strength after 28 days. For a reduction of 25 kg and 0.40%, the slump retention was 90% and 28 days strength improvement was 30% where the cement content was decreased by 25 kg.

	NS1	NS1-0,45%M2-15 kg	NS1-0.45%M2-20 kg	NS1-0.40%M2-20 kg	NS1-0.40%M2-25 kg
3 d	17,73	24,07	20,04	17,40	29,80
7 d	25,16	33,37	28,86	29,35	36,43
28 d	32,25	39,38	37,25	37,21	42,10
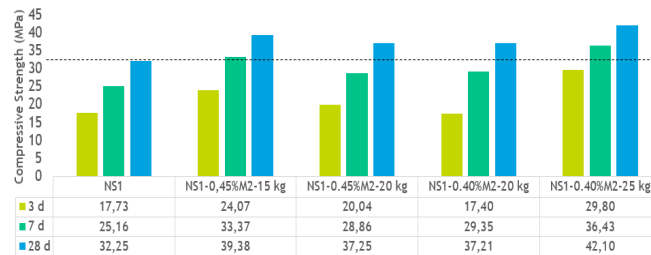
Figure 4. Concrete test with cement reduction with M2.

More sustainable concretes could be produced by minimizing the additional water associated with the clayey fractions present on the aggregates, allowing a 6% reduction in CO_2 for each cubic meter produced or more depending on each scenario.

Conclusions

- Understanding how clayey fractions on aggregates affect concrete, particularly water demand to achieve the same slump that reduces the compressive strength, requiring more cement to ensure performance and emitting more CO_2 per cubic meter. By boosting cementitious efficiency and focusing on the aggregate fraction, the mix can be improved, requiring less cement to achieve the performance required.
- The chemistry behind the sacrificial agents could have a positive or negative effect based on the type of clayey fraction present on each sand, the molecular weight, the cationic molecule charge, and other parameters that need to be linked with the mineralogy of the clayey fraction, and understanding how other minerals, oxides may affect the dosage and effectiveness of the sacrificial agent.
- The heterogeneity of sand sources and the variability in sand extraction involves addressing additional tests and procedures to offer the data required to build trustworthy sacrificial agent molecules and avoid scenarios in which the solution fails.

Acknowledgments

References

ASTM C 33-Standard Specification for Concrete Aggregates. (2018)
ASTM C 128- Standard Test Method for Density, Relative Density (Specific Gravity), and Absorption of Fine Aggregate.
ASTM C 1777- Standard Test Method for Rapid Determination of the Methylene Blue Value for Fine Aggregate or Mineral Filler Using a Colorimeter.
ASTM C 1810- Standard Guide for Comparing Performance of Concrete-Making Materials Using Mortar Mixtures (2021)
INV E-235-07. Valor de azul de metileno en agregados finos.
Jardine, L., Koyata, H., Folliard, K., Chin Ou, C., Jachimowic, F., Chun, B., Jeknovarian, A. Hill, C. (2003). Admixture for optimizing the addition of EO/PO. USA, US 6,670,415 B2.
Ng, S., Plank, J. (2012). "Interaction mechanisms between Na montmorillonite clay and MPEG-based polycarboxylate superplasticizers". Cement and Concrete Research, 42(6), 847–854.
Ma, Y., Shi, C., Lei, L., Sha, S., Zhou, B., Liu, Y, Xiao, Y. (2020). Research progress on polycarboxylate based superplasticizers with tolerance to clays - A review. Construction and Building Materials, 255, 119386.
Muñoz, F., Tejedor, M., Isabel, M, Anderson, Marc, A., Cramer, S. (2010). Detection of Aggregate Clay Coatings and Impacts on Concrete. ACI Materials Journal, 107 (4), 387-395.
Norvell, K., Stewart. G, Juenger, M., Fowler, D. (2007). Influence of Clays and Clay-Sized Particles on Concrete Performance. Journal of Materials in Civil Engineering, 19 (12), 1053-1059.
Ramachandran, V.S., Paroli, M., Beaudoin, J., Delgado, A. (2002). Handbook of Thermal Analysis of Construction Materials. New York, USA, Noyes Publication.

The 16th International Congress on the Chemistry of Cement 2023 (ICCC2023)
"Further Reduction of CO_2 -Emissions and Circularity in the Cement and Concrete Industry"
September 18–22, 2023, Bangkok, Thailand

Effect of the use of different dispersing molecules on the rheological properties and kinetic hydration of Portland cement pastes

F.F. Danila[1*], A.C.R. Martho[2*], R.C.O. Romano[3*] and R.G.Pileggi [4*]

[1] *GCP Applied Technologies, Sorocaba, Brazil*
Email: danila.f.ferraz @gcpat.com
[2] *GCP Applied Technologies, Sorocaba, Brazil*
Email: ariane.martho@gcpat.com
[3]*University of São Paulo, São Paulo, Brazil*
Email: rcorjau@gmail.com
[4]*University of São Paulo, São Paulo, Brazil*
Email: rafael.pileggi@lme.pcc.usp.br

ABSTRACT

The use of water reducers to improve the rheological properties of concrete, in addition to dispersing cement particles, can modify the agglomeration potential of particles and the dissolution kinetics of the clinker phases during the early ages of hydration. In this work two molecules of admixtures based on sodium polycarboxylate were evaluated: the first, with higher dispersion efficiency was named as MR7525 and, the second, with lower dispersion efficiency and higher slump retention was named as MR2575. The study was carried out with the evaluation of cement pastes prepared with Portland cement type CPV, maintaining the constant water-to-cement ratio to evaluate the rheological properties, hydration kinetics and agglomeration. The results indicated differences in the rheological properties of the pastes with different admixtures (initial and depending on the time), facts that can directly impact the process of mixing, transport, application and hardening of the concretes.

Keywords: Portland cement, polycarboxylate, rheometry, Kantro's mini cone, chemical reaction.

1. Introduction

Several admixture technologies can be combined so that performance specifications are met, either from the use of polymers developed to obtain an adequate initial fluidity of the concrete for certain applications, to maintain the workability or even to extend the useful life of the component produced. The chemical affinity between the surface of the cement particle and the admixture is an important parameter for the adequate control of the dosage of the admixture, the specific surface area of the cement defines the dosage of admixture necessary to achieve the specified fluidity for each concrete and the maintenance of workability. The adsorption of the polycarboxylate molecules increases as the dosage of the admixture is increased, until the cement surface is completely covered, thus reaching the saturation or optimal dosage of the admixture. Different polymer structures result in different performances as water reducers or slump retention or to maintain stability. The length and amount of organic chains on the surface of the cement particle and the type, quantity and density of the side chains are responsible for the effectiveness of the steric stabilization of a polycarboxylate ether - PCE in cementitious suspensions, and define the adsorption of these polymers on the surface of the cement particle, in addition to the molecular weight of these admixtures (AÏTCIN et. al, 2016). To adapt admixtures with specific properties to match the requirements of each concrete. The use of rheological control methods can increase the precision of the analyses, since it allows the evaluation according to different shear conditions and the definition of the thixotropy profile, viscosity yield stress, rheological behaviour and consolidation kinetics over time (ROMANO, 2013). This work was carried out with the objective of evaluating the effect of the use of two polycarboxylate-based admixtures on the rheological properties of pastes formulated with Portland cement CP V, using different techniques to determine the ideal content of the admixtures at the initial moments of consolidation over time.

2. Material

A Portland cement type CPV was used , and two admixtures with complementary functions, developed especially for the study, named as MR 7525 and MR 2575. This identification was used to differentiate the amount of dose response polymer (which gives the materials greater initial fluidity), followed by the amount of slump retention polymer to maintain stability. Thus, in the first case, it is expected to obtain greater fluidity and little stability and in the second case, less fluidity and greater stability over time. The polycarboxylate admixtures used in this work are synthetic polymers that have a molecular structure with an organic backbone made of polyoxy-isoprene macromonomers (ethylene glycol), and grafted branches (or side chains) composed of poly-ethylene oxide, they are ester-linked to acrylic units, this conformation has caused polycarboxylate molecules to be often referred to as a "comb" structure. The X-ray fluorescence (XRF) is given in Table 1 (courtesy of the CTL Group), while the particle-size distribution is given in Figure 1 (Malvern Mastersizer 2000/2000E on "wet" samples, i.e. ethyl alcohol).

Property	%
L.O.I	3,90
SiO_2	19,3
CaO	58,9
MgO	3,50
Fe_2O_3	2,40
Al_2O_3	5,40
Mn_2O_3	0,18
TiO_2	0,25
SO_3	4,20
Na_2O	0,40
K_2O	0,88
*Álcali eq.(in Na_2O) *	1,01

* Na_2O + 0,658 K_2O

Real density: 2,91 g/cm³
Specific surface área:1,58m²/g
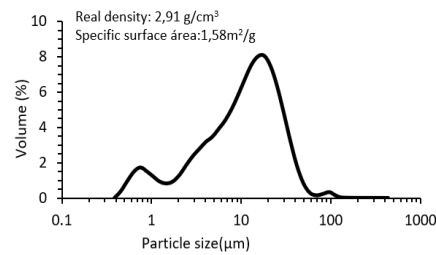
Table 1 and Figure 1: Chemical and physical results for cement CP V

3. Methods

A water-to-cement ratio (w/c) of 0.35 was used for all cement pastes, the pastes preparation, rotational and oscillatory rheometry, and calorimetry protocol was conducted using the same procedure described in described in Ferraz et al. 2020. In order to determine the admixture dosage, deflocculation curves were performed to find an optimum dosage. This resulted in the following dosages for each of the cement types.

4. Results and Discussion

The presentation of the results was divided into two stages, the first of which determined the ideal content of each admixture for the type of cement chosen, and the second evaluated the impact on consistency gain over time. With this strategy, it was intended to monitor the impact of the difference in admixtures in the stage of preparation and application of the cementitious component. Figure 2 shows the spreads (flow) of the pastes obtained from the Kantro cone test.
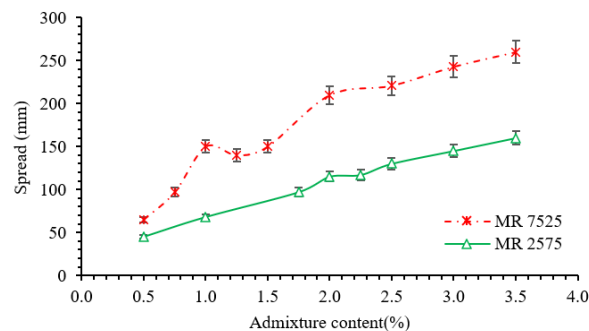
Figure 2: Spreading in the Kantro cone test, in the suspensions with the two admixtures

The higher the amount of DR polymer in the admix., the greater the spreading, following the initial expectation, based on the formulation of the admixtures, in addition, there is a correlation between the increase in the admixture content and the increase in spreading using Kantro mini-cone test. From the rotational rheometry tests it is possible to obtain more complete information about the characteristics of

75

the products under different application conditions. The results obtained are usually presented in the form of graphs of shear stress (or viscosity) vs. shear rate, as illustrated in a didactic way in Figure 9, making it possible to evaluate the rheological behavior profile of each composition. To determine the optimal admixture content, the results of yield stress, viscosity (apparent or plastic) and hysteresis area are used as a function of the content added in the composition (MONTEFUSCO et al. 2017). Based on these parameters, the graphs shown in Figure 3a indicate the variation in apparent viscosity, in b, flow stress and in c, hysteresis area of the pastes as a function of the variation in content and type of admixture.
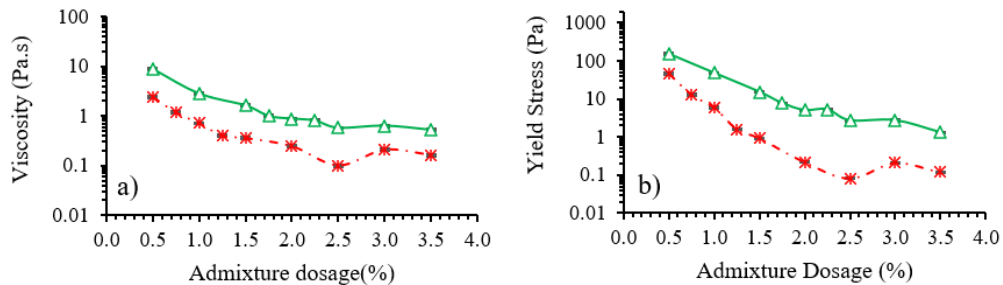
Figure 3: a) Evolution in apparent viscosity and b) yield stress

The choice of the optimized admixture content was made with the viscosity stabilization, but also considered the flow stress as close as possible to zero. The variation range of the admixture content was the same regardless of the type used, however the results of yield stress and viscosity were lower due to the increase in the amount of spreading polymer, converging with what was expected for the action of each admixture. Based on the results of rotational rheometry, it was possible to define that the optimized content of the admixtures was the same (2.5% by mass) and they were used to evaluate the stability over time, presented later. Even with the optimized content being the same for both admixtures, the apparent viscosity in the paste with the lowest amount of opening polymer (MR 2575) was an order of magnitude greater than in the paste with the highest amount of the same polymer. This fact was intensified with regard to the yield stress, the difference between them being two orders of magnitude, which indicates that the admixture acts more by altering the minimum stress necessary for the start of the flow than in the viscosity. In this work, it was possible to correlate the results of the rheological tests with the scattering obtained in the Kantro mini-cone method, as illustrated in Figure 4.
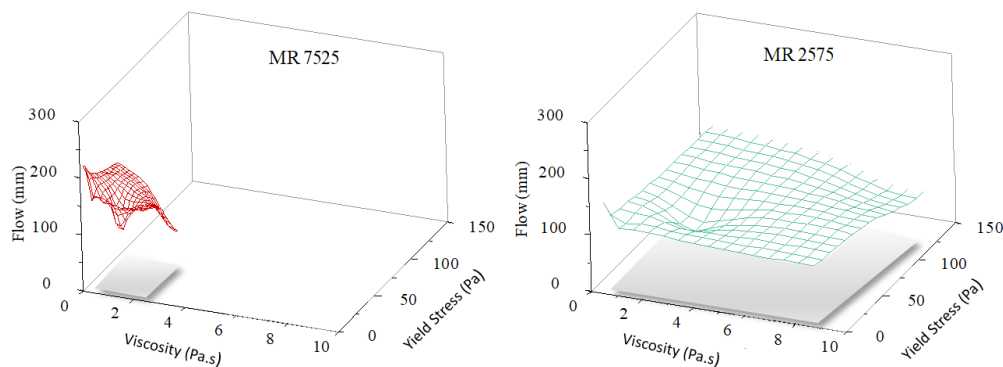
Figure 4: Surface analysis scattering x viscosity x yield stress

With the results presented so far, information is only available on the characteristics of the pastes in the first instants of cement hydration, since the tests were carried out 5 minutes after mixing. However, no information is available on stability over time.

For this, oscillatory rheometry tests were performed and the results are presented below. At this stage, the tests were carried out only for pastes with admixtures at ideal levels.

The results are shown in Figure 5 from the evolution of G' as a function of time after microstructural disruption (a), the particle reagglomeration rate (b) and the scattering measured from the Kantro mini-cone test along of time (c). Polymers intended for fluidity retention (slump-keeper) have slower

76

adsorption, modifying the fluidity of the system later, as observed for the MR2575 product. In addition, such polymers have greater affinity for the hydrates formed during the cement reaction and undergoing hydrolysis with the increase in the pH of the suspension. Thus, the combination of the two types of polymers in the same product made it possible to tailor an admixture for each desired property.
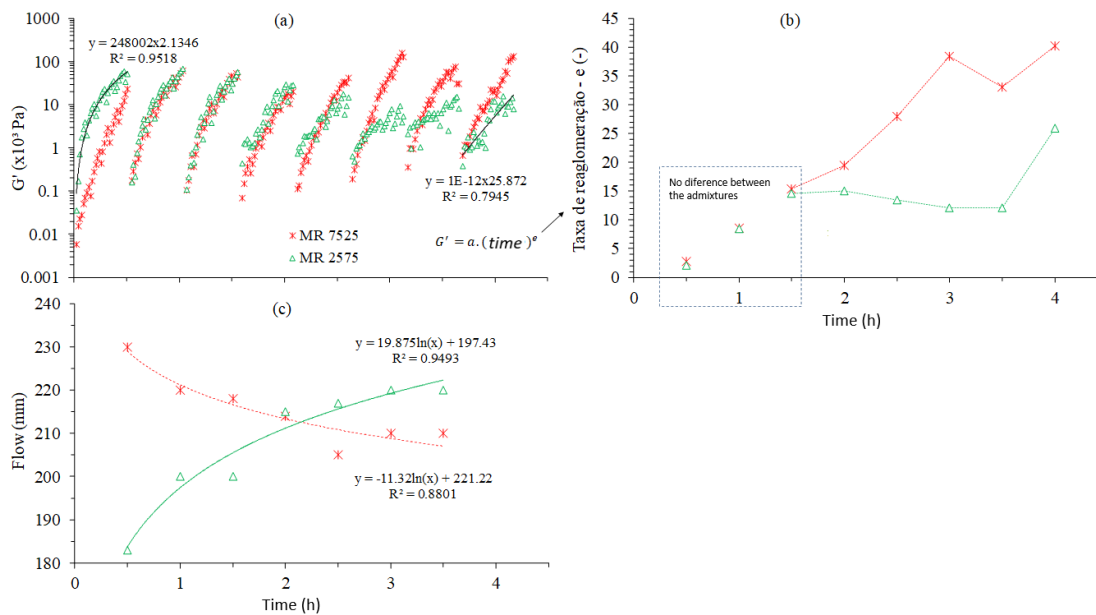
Figure 5: Evolution of G' in function of time after microstructural disruption (a), evolution of the particle reagglomeration rate (b) and scattering measured from the Kantro test along the time

5. Conclusion

The use of different polycarboxylate molecules, in synergy, showed different results regarding the initial dispersion efficiency of the cement particles and the maintenance of the open time.

In this way, it can be inferred that: a) both by rotational rheometry and from the spreading by the Kantro cone, it was possible to observe differences in the rheological behavior and fluidity, between the two admixtures in the pastes with the CPV cement; b) the greater amount of opening polymer resulted in lower values of yield strength and viscosity of the pastes, facilitating the quantified flow from mini-slump; c) from the results of rotational rheometry it was possible to define the ideal contents for each admixture in relation to the type of cement evaluated and d) correlating the scattering results with the rheological parameters, it was confirmed that the change in scattering was governed by both viscosity and yield stress (in this second case, a better correlation between the two techniques).

References
Aïtcin, P.-C.; and Flatt, R.; Science and Technology of Concrete Admixtures, Woodhead Publishing, 2015.
Berodier, E.; Gibson, L.R.; Burns, E.; Cheung, J.; Robust production of sustainable concrete through the use of admixtures and in-transit concrete management systems. Cement and Concrete Composites, Grand Challenges in Construction Materials 2016. v. 101, p. 52–66, 1 ago. 2019.
Ferraz, D; Martho, A.C.R.; Burns, E.G.; Romano, R.C.O.; and Pileggi, R.G.; "Effect of mixing procedure on the rheological properties and hydration kinetics of Portland cement paste," Rheology and Processing of Construction Materials, Mechtcherine, V.; Khayat, K.; Secrieru, E.; eds., 2020.
Romano, R. C. de O., Incorporação de ar em materiais cimentícios aplicados em construção civil. PhD thesis, University of São Paulo, 2013.
Montefusco, H., Maciel, M. H., Brasileiro, G.C.P., Mesquita, J.A.F.S, Evaluation of superplasticizer and particle size distribution of aggregates in the rheological properties of concretes; Conference: Congresso Brasileiro de Cerâmica, Gramado, Volume: 61, 2017.

Aluminum sulfate-based accelerators: rheological implications for 3D-printed concretes

L. Caneda-Martínez [1,2*], E. Keita[1], H. Bessaies-Bey[1], M. Duc[1], B. González-Fonteboa[2], and N. Roussel[1]

[1] *Gustave Eiffel University, Champs sur Marne, France*

Email: E.K. : emmanuel.keita@univ-eiffel.fr; H.B-B.: hela.bessaies-bey@univ-eiffel.fr; M.D.: myriam.duc@univ-eiffel.fr; N.R.: nicolas.roussel@univ-eiffel.fr
[2] *Universidade de A Coruña, A Coruña, Spain*

Email: L.C-M.: laura.cmartinez@udc.es; B. G-F.: belen.gonzalez.fonteboa@udc.es

ABSTRACT

The implementation of digital fabrication in the concrete manufacturing industry, notably extrusion 3D printing, is emerging as a transformative and highly valuable tool for the construction sector. The main advantage of this method is the lack of need for formwork, which translates into greater design flexibility and optimization of materials and time, among other benefits. In the absence of formwork, however, the properties of concrete in the fresh state must be carefully tailored, as they must adapt to the rheological requirements of each stage of the process. In this context, accelerators play a central role. The utilization of alkali-free accelerators (based on aluminum sulfate solutions) has been conventionally relegated to shotcrete applications. However, increased interest in their use has arisen with the emergence of concrete 3D printing.

In this work, studies are conducted to relate the impact of the use of aluminum sulfate as an accelerator on the hydration reactions of cement and its subsequent effect on rheology. For this purpose, the evolution of the hydration reaction is evaluated by in-situ X-ray diffraction (XRD) on cement pastes. In parallel, the pastes rheology is assessed by penetration tests. XRD results allow for the monitoring of ettringite growth over time and the assessment of its impact on solid volume fraction. The results suggest that the evolution of the material rheological properties cannot be solely explained by the increase of the solid fraction caused by the precipitation of ettringite.

KEYWORDS: *concrete 3D printing, accelerators, aluminum sulfate, rheology, ettringite.*

1. Introduction

The digitization of concrete manufacturing has attracted increasing interest in recent times, especially in the field of concrete 3D printing by extrusion, as it promotes greater flexibility in construction and the creation of optimized designs. However, to be successfully printed, concrete must undergo a variety of processes involving demanding rheological requirements, particularly in the fresh state, which frequently implies the optimized use of admixtures. Among them, accelerators are instrumental in satisfying some of the requirements needed in 3D printing. Alkali-free accelerators, conventionally used in shotcrete applications, are one of the most demanded options in the sector. They are based on aluminum sulfate solutions, which are known to be highly effective in accelerating the hydration reactions of aluminates in cement. Even though alkali-free accelerators have been used for years, research related to their effects on the properties of concrete, particularly with respect to its rheology, is scarce.

This work aims to relate the effects of the acceleration of cement hydration caused by aluminum sulfate on the rheological properties of cement pastes. To this end, the study of the rheology of cement pastes by penetration tests is combined with the monitoring of the evolution of cement hydration by means of in-situ X-ray diffraction, focusing on its effect on the changes in the solid volume fraction of the pastes.

2. Materials and methods

A Portland cement type CEM I 52.5 N was used in this study. Its chemical composition is shown in Table 1. Mineralogically, the cement is composed by alite (65.3%), belite (14.1%), C_3A (8.1%), C_4AF (7.6%), basanite (3.2%), gypsum (0.4%) and others (1.3%). A commercial aluminum sulfate hydrate, supplied by Sigma Aldrich, was used as an accelerator.

Table 1. Elemental composition of the starting cement.

Oxide	CaO	SiO$_2$	Al$_2$O$_3$	Fe$_2$O$_3$	MgO	SO$_3$	MnO	Na$_2$O	K$_2$O	TiO$_2$	P$_2$O$_5$	LoI
%	65.17	20.3	4.86	2.8	0.95	2.01	0.11	0.22	0.89	0.24	0.31	1.48

In-situ X-ray diffraction (XRD) was performed on a D8 Advance diffractometer (Bruker AXS) equipped with a LynxEye detector and a cobalt anode, operated at 40 mA and 35kV. Scans were recorded from 8.5º 2θ to 49º 2θ, with a step size of 0.025º and 0.5 s/step. The reference paste (OPC) was prepared at a w/c of 0.35 by mixing the cement with water for one minute by hand. For the accelerated paste (1.5%Acc), 1.5% (by weight of cement) of aluminum sulfate was dissolved in the hydration water prior to the mixing. The pastes were placed in an airtight sample holder covered with kapton film to minimize water evaporation. The quantification of each phase was performed following the Rietveld method, using the software TOPAS v2.4 (Bruker). The G-factor method was applied by measuring a corundum sample of known crystallinity under the same conditions as the pastes (Jansen et al. 2011). In addition, the kapton film was measured by placing it on a single-crystal silicon sample holder, and it was later used as a model to fit the background of the diffractograms of the pastes.

The rheology of the pastes was indirectly assessed by penetration tests, using a VFG Mecmesin handheld force gauge and a 5 mm radius spherical probe. The cement pastes were mixed for one minute in a planetary mixer at 67 rpm, then placed in 4x4x16 cm^3 moulds and vibrated for 30 seconds. The maximum penetration force was measured at different hydration times.

3. Results and discussion

3.1. X-ray diffraction

Figure 1a compares the diffractograms obtained at the beginning of the hydration reaction for the reference (OPC) and the accelerated (1.5% Acc) pastes. Two significant changes with respect to the diffractogram of the anhydrous cement are observed. Firstly, the diffraction peaks corresponding to basanite are no longer detected, but an increase in the gypsum peaks is observed instead. This is consistent with the differences in solubility of both compounds, according to which an immediate dissolution of basanite upon contact with water is expected, leading to rapid precipitation of gypsum due to its low solubility. Secondly, the presence of peaks attributable to ettringite becomes manifest, evidencing the onset of hydration of the aluminate phases.
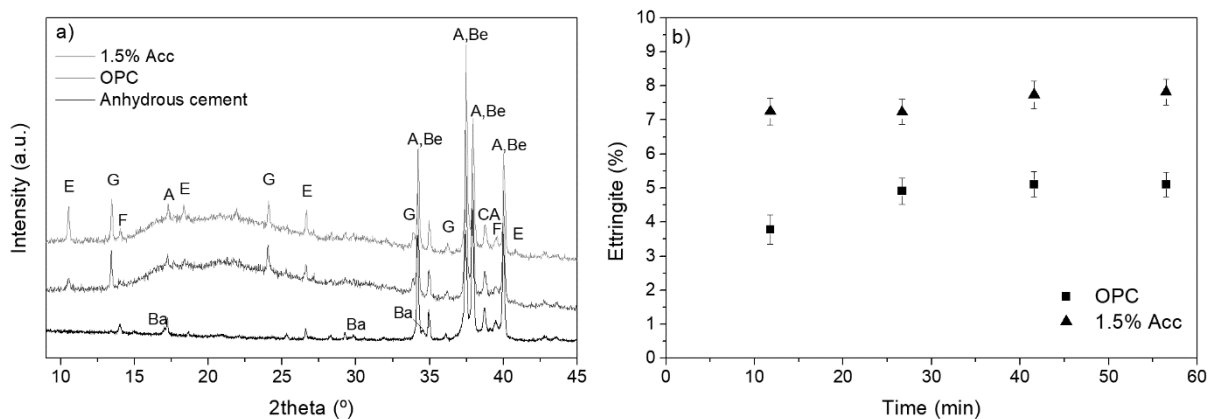
Figure 1. a) Initial diffractograms of the hydrated OPC and 1.5% Acc pastes and of the anhydrous cement (A: alite, Ba: basanite, Be: belite, CA: C$_3$A, E: ettringite, F: C$_4$AF, G: gypsum); b) Ettringite content over time.

The quantification of ettringite over the hydration time of the pastes is shown in Figure 1b. The results reveal that most of the ettringite precipitates in the first minutes of the reaction, although its content continues to increase slowly with time. The addition of the accelerator results in an increase in the initial ettringite formation of 80% with respect to the OPC paste, but this increase is reduced to approximately 50% in subsequent measurements.

3.2 Penetration tests and rheological analysis

The yield stress of the pastes was indirectly evaluated by penetration tests, as penetration forces are known to be directly correlated with the yield stress of cement pastes (Lootens et al. 2009). Figure 2 shows the evolution over time of the maximum forces of the Acc 1.5% paste relative to the initial maximum force of the OPC paste. The addition of the accelerator leads to an overall gain in the penetration force with respect to the OPC paste, resulting in an initial relative increase of approximately 5 times that of the OPC paste. This increase is further enhanced as hydration develops, following an approximately linear initial trend that tends towards stabilization after about 45 minutes. The explanation for this behavior could be found in the precipitation of ettringite, which consumes 32 molecules of water per mole of ettringite formed. This is typically associated with a rise in the solid volume fraction of the mix, and consequently with an increase in yield stress (Jakob et al. 2019). Such gain in the solid volume fraction has been verified by calculating the volume of the phases quantified by XRD, showing an increase of 6-8% in the 1.5%Acc paste with respect to the OPC paste (see Table 2).
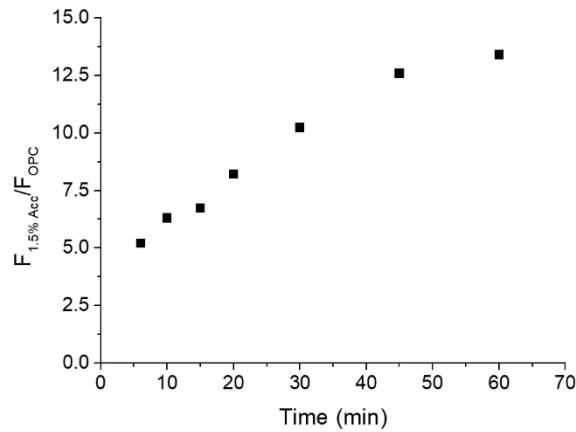
Figure 2. Relative maximum forces of paste Acc 1.5% with respect to the initial maximum force of paste OPC.

The relationship between yield stress and solid volume fraction (ϕ) can be described by the YODEL model (Flatt and Bowen 2006):

$$\tau_0 = \frac{m\, A_0 a^*}{d^2 H^2} \frac{\phi^2(\phi - \phi_{perc})}{\phi_m(\phi_m - \phi)} \tag{1}$$

Where m is a pre-factor associated to the particle size distribution, A_0 is the non-retarded Hamaker constant, d is the average particle diameter, a^* is the radius of curvature of the contact points, H is the surface separation distance at contact points, ϕ_{perc} is the percolation volume fraction and ϕ_m is the maximum packing fraction of the powder.

If we assume that the variation of yield stress in the system is dominated by the changes in solid volume, the YODEL model can be applied to calculate the relative increase in yield stress, based only on the variation of the solid volume fraction. For such calculation, it is assumed that ettringite precipitation does not have a significant effect on the interparticle forces, and therefore that the first term of equation 1 remains unaffected in the accelerated paste. In addition, the change in the maximum packing fraction is considered to be negligible in this hypothetical scenario. A value for ϕ_m of 0.66, measured on the OPC paste by centrifugation (Bessaies-Bey et al.), is considered for the calculations. The percolation volume fraction is assumed to be 0.37 (Perrot et al. 2012). The results in Table 2 show that the predicted relative increase in

yield stress resulting from the increase in solid volume fraction is considerably lower than the relative maximum forces assessed by penetration, despite the fact that both properties (yield stress and penetration force) are known to be proportional.

Table 2. Relative solid volume fraction, penetration force and yield stress of 1.5% Acc with respect to OPC.

	Time (min)			
	10	**30**	**45**	**60**
$\phi_{1.5\%Acc}/\phi_{OPC}$ (computed)	1.07	1.06	1.07	1.08
$F_{1.5\%Acc}/F_{OPC}$ (measured)	6.3	10.2	12.6	13.4
$\tau_{1.5\%Acc}/\tau_{OPC}$ (computed)	1.9	1.9	2.0	2.1

These findings suggest that ettringite precipitation has additional effects on the properties of the paste beyond the increase in solid volume. One possibility could be that the formation of ettringite affects the interparticle forces, and thus the initial term of the YODEL model. This phenomenon could occur, for example, if the ettringite crystals act as bridging agents between particles. Another option could be that the ettringite crystals impact the packing properties. This latter hypothesis would be supported by the characteristic needle-like shape of ettringite, as it is known that elongated particles tend to reduce the maximum packing fraction (Philipse 1996). Both aspects - the impact of ettringite formation on interparticle forces and on maximum packing fraction - are crucial for the understanding of the fresh properties of concrete and for the development of concrete 3D printing, and will be tackled in future works.

4. Conclusions

The addition of aluminum-sulfate accelerators promotes the precipitation of ettringite, which leads to an increase in solid volume fraction and in the yield stress of the cement paste, as evidenced by XRD measurements and penetration tests. However, this rise in yield stress, cannot be fully accounted for by the changes in the solid volume fraction, as other aspects such as variations in the interparticle forces or in the maximum packing fraction must also be taken into account.

Acknowledgements

References

Bessaies-Bey, Hela et al. "Packing Properties Assessement of Cement and Alternative Binders through Centrifugation: Artifacts and Protocol", to be submitted.

Flatt, Robert J., and Paul Bowen. 2006. "Yodel: A Yield Stress Model for Suspensions." *Journal of the American Ceramic Society* 89(4): 1244–56.

Jakob, Cordula et al. 2019. "Relating Ettringite Formation and Rheological Changes during the Initial Cement Hydration: A Comparative Study Applying XRD Analysis, Rheological Measurements and Modeling." *Materials* 12(18).

Jansen, Daniel, Friedlinde Goetz-Neunhoeffer, Christopher Stabler, and Jürgen Neubauer. 2011. "A Remastered External Standard Method Applied to the Quantification of Early OPC Hydration." *Cement and Concrete Research* 41(6): 602–8.

Lootens, D. et al. 2009. "Yield Stress during Setting of Cement Pastes from Penetration Tests." *Cement and Concrete Research* 39(5): 401–8.

Perrot, A. et al. 2012. "Yield Stress and Bleeding of Fresh Cement Pastes." *Cement and Concrete Research* 42(7): 937–44.

Philipse, Albert P. 1996. "The Random Contact Equation and Its Implications for (Colloidal) Rods in Packings, Suspensions, and Anisotropic Powders." *Langmuir* 12(24): 5971–5971.

Flatt, Robert J., and Paul Bowen. 2006. "Yodel: A Yield Stress Model for Suspensions." *Journal of the American Ceramic Society* 89(4): 1244–56.

The 16th International Congress on the Chemistry of Cement 2023 (ICCC2023)
"Further Reduction of CO2 -Emissions and Circularity in the Cement and Concrete Industry"
September 18–22, 2023, Bangkok, Thailand

Development of ultra-fine SAP powder for lower-shrinkage and high er-strength cement pastes made with ultra-low water-to-binder ratio

Jianhui Liu[1,2,3*], Le Teng[4], Zheng Chen[1,2,3], and Caijun Shi[5]

[1] *Key Laboratory of Disaster Prevention and Structural Safety of China Ministry of Education, School of Civil Engineering and Architecture, Guangxi University, Nanning, PR China*
Email: liujianhui@gxu.edu.cn
[2] *State Key Laboratory of Featured Metal Materials and Life-cycle Safety for Composite Structures, Guangxi University, Nanning, PR China*
[3] *State Key Laboratory of Featured Metal Materials and Life-cycle Safety for Composite Structures, Guangxi University, Nanning, PR China*
[4] *School of Materials Science and Engineering, Southeast University, Nanjing, PR China*
[5] *Key Laboratory for Green & Advanced Civil Engineering Materials and Application Technology of Hunan Province, College of Civil Engineering, Hunan University, Changsha, PR China*

ABSTRACT

Superabsorbent polymer (SAP) as internal curing agent can effectively mitigate the autogenous shrinkage and promote cement hydration of ultra-high performance concrete (UHPC). However, it has a risk of impairing the mechanical performance of UHPC given the macro pores left. This study developed ultra-fine SAP powder aiming at securing the lower shrinkage and higher strength of UHPC. The influence of SAP powder on (average diameter (ds) of 5.78-60.85 μm) the water absorption/desorption characteristics, strength, shrinkage, and microstructure of cement paste with ultra-low water-to-binder ratio (w/b) was systematically studied. The results showed that the reduction of particle size of SAP can reduce the spacing distance of SAP in cement paste, which is beneficial for the internal curing, such as reducing the autogenous shrinkage, improving hydration of cement, and increasing the compressive strength.

KEYWORDS: *Autogenous shrinkage; Hydration; Internal curing; Microstructure; Superabsorbent polymer (SAP).*

1. Introduction

The objective of internal curing is to enable a higher internal relative humidity and a lower autogenous shrinkage in concrete by a subsequent release of water from pre-wetted lightweight aggregates (LWA) or superabsorbent polymers (SAP). The gradual release of internal curing water can also promote the hydration of cement. Compared to LWA, SAP can provide a more effective IC due to the higher water absorption.

The effectiveness of internal curing of SAP is related to the SAP chemical composition, content, and particle size. Zhong et al. found that the content of SAP is a factor that affects the internal curing of concrete. The internal curing efficiency or the reduced amplitude of autogenous shrinkage increased as the content of SAP increased. Besides, the size of SAP particles is a key factor on the internal curing efficiency for mitigating autogenous shrinkage. There is a controversy on the effect of particle size on the absorption capacity. The effect of SAP particle size on water adsorption and release characteristics can be influenced by other factors, such as the w/cm, which necessitates an in-depth study.

Because the moisture migration distance is reduced with the decrease of w/b given the dense microstructure. The particle size of conventional SAP currently studied ranges between 50 and 500 μm. The use of ultra-fine SAP can theoretically provide a larger internal curing zone compared to the conventional SAP because of larger specific surface area, which can enhance the cement hydration and reduce autogenous shrinkage of UHPC. However, the reduction of SAP particle size can influence the water adsorption and desorption characteristics, which might compromise the internal curing effect of SAP. Therefore, this study developed the ultra-fine SAP powder and characterized their water absorption and desorption capacity. The effect of

these ultra-fine SAP powder on the strength, shrinkage, and microstructure of paste phase of UHPC was investigated. The test results were used to determine the factors affecting the internal curing due to the variation of SAP particle size. A quantitative model that considers these factors was further established to understand the mechanism of SAP particle size on internal curing. The results of this paper aim to promote the application of using SAP to cure UHPC.

2. Raw materials、 mixture proportion and experimental methods

2.1 Raw materials

The binder materials included P.I. 42.5 Portland cement and silica fume. A high-performance superplasticizer (SP) with a solid mass content of 23% was used in this study to enhance the workability (within 230±10 mm). The SAP powder used in this study was a cross-linked acrylamide/acrylic sodium copolymer, which is derived from manufacturers. The ratio of acrylamide and acrylic sodium is 0.3. The mean particle size of this commercially available SAP was 60.85 μm (noted as S0). Such SAP was ground into four sizes using an air pulverizer. The mean particle sizes of SAP powder were 45.46, 25.87, 11.55, and 5.78 μm, referring to S1, S2, S3, and S4, respectively.

2.2 Mixture proportion

The mixture proportions of cement paste are shown in Table 1.

Table 1 Mixture proportion of cement pastes with or without SAP powder

No.	Binder materials (%)		Total w/b	Additional w/b	SAP (%, by weight of binder)	SP (%, by weight of binder)
	Cement	Silica fume				
R0.18	80	20	0.18	0	0	2.0
R0.22	80	20	0.22	0	0	1.5
S0	80	20	0.22	0.04	0.3	2.0
S1	80	20	0.22	0.04	0.3	2.0
S2	80	20	0.22	0.04	0.3	2.0
S3	80	20	0.22	0.04	0.3	2.0
S4	80	20	0.22	0.04	0.3	2.0

2.3 Experimental methods

The test methods about ^{1}H nuclear magnetic resonance (NMR), Hydration heat, Autogenous shrinkage, Compressive strength, Hydration products and microstructure.

3. Results

3.1 Absorption/desorption properties of SAP

The T2 relaxation signals of cement paste was shown in Fig. 1. The intensity of the peak is presented using different colours. In order to quantify the water content of SAP powder at different time, the amount of water (α) absorbed/released by the unit weight of SAP over time was calculated according to the peak 2 intensity. In general, the water adsorption and desorption rates, as well as the maximum water absorption were shown to be influenced by the particle size of SAP powder. The bigger the particle is, the more pore fluid is absorbed into the cross-linked structure by its original mass.

3.2 Hydration heat

The SAP powder slowly released the water after reaching saturation point, thus promoting cement hydration., As hydration time increased, the heat flow rate of mixtures containing SAP powder was gradually greater than R0.22, which indirectly reflected the water release process of SAP powder.

On the other hand, it means that the increase in heat of hydration is not proportional to the decrease in SAP particle size. It is mainly because larger SAP particle had a lower absorption time and reduced the early-age hydration heat compared with smaller SAP. In addition, for cement-based materials with a certain

water-cement ratios (assuming the porosity is basically the same), there may be a threshold for the SAP particle size; if the particle size is below a certain value, the distribution of SAP particles can lead to a larger range of internal curing area, which is more beneficial for increasing hydration heat and this demonstrated that reduction SAP particle size promoted the early internal curing effect.

3.3 Autogenous shrinkage

Fig. 2 shows that the effect of particle size of SAP powder on autogenous shrinkage. The autogenous shrinkage of R0.18 and R0.22 mixtures were 2630 and 2011 με at 72h, respectively. This implies that the increase in w/b can reduce the autogenous shrinkage. The addition of SAP powder was more effective to reduce the autogenous shrinkage compared to the increase of w/b. This is because the water released form SAP powder can restrain the drop of relative humidity in cement paste.

3.4 Compressive strength

Figure 3 shows that the effect of w/b and particle size of SAP powder on the compressive strength at various ages. The addition of SAP powder and additional water led to a lower compressive strength compared to the reference UHPC made with w/b of 0.18. In fact, the use of conventional SAP can lead to 10-20% reduction in compressive strength of UHPC regardless of the internal curing effect of SAP. The lower decrease of compressive strength for UHPC made with finer SAP can be attributed to the smaller pores left after water desorption. With the increase of hydration age, the reducing amplitude of SAP group dropped because the enhanced cement hydration due to the internal curing effect of SAP compensated the influence of SAP pores on reducing the compressive strength. The influence of SAP particle sizes on compressive strength is mainly related to the spatial distribution and water absorption and release characteristics of SAP powder.

3.5 Hydration products

(1) TG and DTG analysis
The chemical bound water (CBW) and calcium hydroxide (CH) content were calculated. The CBW content increased with the increase of curing age and w/b. This was because the gradual release of water absorbed by SAP powder promoted the cement hydration. This also demonstrated that mixtures with a higher w/b exhibited a greater degree of cement hydration, which is consistent with the CBW content.And, the water absorbed by SAP powder gradually released to promote the hydration of cement, resulting in a higher content of CH. Such results were in an agreement with the variation of CBW content with SAP powder.
(2) 29Si NMR
The variation of 29Si NMR intensity of cement paste made with different particle sizes of SAP powder. The deconvolution results are shown in Table 4. The higher C and H values refers to greater degree of cement hydration and pozzolanic reaction of silica fume. The incorporation of SAP powder was also shown to increase the average C-S-H chain length, especially for the S2 and S3 SAP powder. Thus, it can be concluded that internal curing promotes the hydration of cement pastes, leading to the formation of long chain C-S-H, which is attributed to the continuing hydration of cement and increasing pozzolanic activity of silica fume.
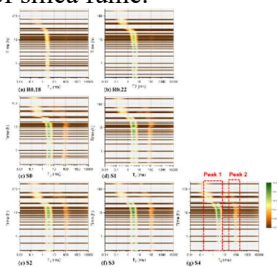
| Fig. 1 T2 relaxation signal of cement paste containing with or without SAP powder | Fig. 2 Autogenous shrinkage of cement pastes with different particle sizes of SAP powder | Fig. 3 Variation of compressive strength of cement pastes with different particles sizes of SAP powder |
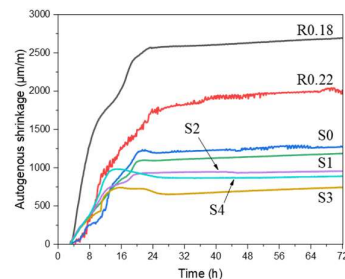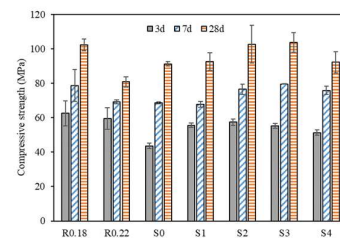
3. Conclusions

Based on the above experimental results and discussion, the following conclusions can be drawn: The maximum water absorption of reduced with decrease of SAP particle size; A linear relationship was found between the water absorption of SAP measured using 1H NMR and Tea bag method; The reduction of particle size of SAP decreased the spacing distance of SAP in cement paste, which benefits to the internal curing, and led to a reduction in autogenous shrinkage, improvement in cement hydration, and enhancement in compressive strength. The decrease of spacing distance between SAP particles and SAP water absorption led to a lower level of shrinkage when the total w/b was kept the same.

Acknowledgements

References

L. Teng, A. Addai-Nimoh, K.H. Khayat. (2023) "Effect of lightweight sand and shrinkage reducing admixture on structural build-up and mechanical performance of UHPC", *Journal of Building Engineering*, 68 106144

Weina Meng and Kamal Khayat, C.K.Y. (2017) "Effects of saturated lightweight sand content on key characteristics of ultra-high-performance concrete", *Cement and Concrete Research*, 101: 46-54

L. Liu, Z. Fang, Z. Huang and Y. Wu. (2022) "Solving shrinkage problem of ultra-high-performance concrete by a combined use of expansive agent, super absorbent polymer, and shrinkage-reducing agent", *Composites Part B: Engineering*, 230(2): 105903

Liu JH, Shi CJ, Ma XW, Khayat KH, Zhang J and Wang DH. (2017) "An overview on the effect of internal curing on shrinkage of high performance cement-based materials.", *Construction and Building Materials*, 146: 702-712

P. Zhong, Z. Hu, M. Griffa, M. Wyrzykowski, J. Liu and P. Lura. (2021) "Mechanisms of internal curing water release from retentive and non-retentive superabsorbent polymers in cement paste", *Cement and Concrete Research*, 14

J. Liu, N. Farzadnia, K.H. Khayat and C. Shi,. (2021) "Effects of SAP characteristics on internal curing of UHPC matrix", *Construction and Building Materials*, 280: 122530

J. Liu, X. Ma, and C. Shi, S . (2021) "Internal curing of blended cement pastes with ultra-low water-to-cement ratio: Absorption/desorption kinetics of superabsorbent polymer", *Journal of the American Ceramic Society*, 104: 3603-18

O.M. Jensen, and P.F. Hansen. (2002) "Water-entrained cement-based materials II. Experimental observations", *Cement and Concrete Research*, 32 : 973-978

J.H. Liu, N. Farzadnia, C.J. Shi and X.W. Ma. (2019) "Shrinkage and strength development of UHSC incorporating a hybrid system of SAP and SRA", *Cement and Concrete Composites*, 97: 175-89

K. Scrivener, R. Snellings, and B. Lothenbach. (2016) "A practical guide to microstructural analysis of cementitious materials", *Crc Press*

Influence of negative temperature hardening on hydration and pore structure evolution of Portland cement paste

Shuai Bai[1*], Xinchun Guan[2]

[1] *School of Civil Engineering, Harbin Institute of Technology, Harbin, China*
Email: bai.shuai@outlook.com
[2] *School of Civil Engineering, Harbin Institute of Technology, Harbin, China*
Email: guanxch@hit.edu.cn

ABSTRACT

This paper investigated the hydration and pore structure evolution of negative temperature hardening cement paste, and the influence of negative temperature (-5 ℃) was highlighted. Thermogravimetric analysis (TGA) and mercury intrusion porosimetry (MIP) was used to gain information on hydration and pore structure. TG results show that negative temperature hardening severely inhibits the hydration reaction, resulting in a significant decrease in the hydration degree, C-S-H gel content and gel-space ratio. However, as the hydration age increases to 120 days, the hydration degree and gel-space ratio of negative temperature hardening cement paste can reach the positive temperature level, while the C-S-H gel content is still lower than the positive temperature level. MIP results indicated that negative temperature obviously delayed the development of pore structure and significantly increases total porosity and most probable pore diameter, indicating that negative temperature hardening seriously affects the compactness of pore structure.

KEYWORDS: *cement paste, negative temperature hardening, hydration, pore structure*

1. Introduction

Hardening temperature is known to affect the reactivity and hardened properties of cement-based materials adversely. Some literature [1,2,3] have provided experimental data to prove that hardening temperature plays a vital role in the development of strength. A decrease in hardening temperature can deaccelerate the strength development of cement-based materials [4,5,6,7].

Hydration progress is the key to affecting the macro strength of hardened cement pastes [8]. Previous studies [9,10,11] have shown the linear, cubic, or exponential relations between the compressive strength and hydration characteristic parameters.

Pore structure is also one of the key factors controlling the strength and durability of hardened cement pastes [12]. All types of pore and pore shapes control the mechanical properties, and the amount of interconnecting pores and the tortuosity of pores mainly affected the durability of concrete [13,14]. Large pores are considered to have more dominant effect on strength and durability, and gel pores mainly affect the shrinkage and creep [15,16].

Therefore, the aim of the present work was to study the hydration and pore structure evolution of negative temperature hardening cement paste. Thermogravimetric analysis (TGA) was used to gain information on hydration degree and hydrates. Mercury intrusion porosimetry (MIP) was used to obtain the pore structure information and pore size distribution, and the pore structure was analyzed with the help of the fractal model.

2. Experiment

2.1 Material and preparation

A commercially available ordinary Portland cement is used as a binder material and the physicochemical properties of the binder material are given in Tables 1. The water to cement ratio of 0.35 was used for all the cement pastes and the pastes were mixed according to ASTM C 305 standard [17]. After pre-curing for 24 h at room temperature, all the pastes were demolded and then cured at +20 °C and -5 °C for 3, 7, 14, 28, 56, and 120 days, respectively.

Table 1. Chemical and mineral composition of cement.

Chemical composition (wt%)	SiO_2	Al_2O_3	Fe_2O_3	CaO	MgO	f-CaO	Loss
	21.14	5.72	3.62	64.84	1.53	1.33	1.13
Mineral composition (wt%)	C_3S	C_2S	C_3A	C_4AF			
	54.30	19.66	9.04	11.00			

2.2 Methods

A thermogravimetric apparatus (TA Discovery SDT 650) was used to obtain the TG and DTG curves. The temperature range of TGA is from 30 °C to 800 °C at 10 °C/min in a nitrogen atmosphere. TG samples were pulverized and then oven-dried at 60 °C for 72 h before testing.

The MIP technique (AutoPore IV 9500, USA) is used to measure the characteristic pore sizes and pore size distribution of cement-based materials. MIP samples were immersed in ethanol for 7 days to remove the free water inside pastes. After immersing, these samples are dried in an oven at about 60 °C for 72h before testing.

3. Results and discussions

3.1 Hydration degree and C-S-H gel content

According to the Refs. [18,19], hydration degree of cement paste is calculated by the chemically combined water content. Based on the thermogravimetric data, the calculated hydration degree of cement pastes cured at +20 °C and -5 °C is presented in Fig. 1. Before 28 days of hydration, the hydration degrees of negative temperature hardening cement pastes are much lower than those of positive temperature hardening cement pastes, indicating that the hydration reaction is seriously inhibited by negative temperature hardening. However, when the hydration age increases to 120 days, the hydration degree of negative temperature hardening cement pastes is similar to that that of positive temperature hardening cement pastes. It is indicated that the hydration degree of negative temperature hardening cement paste can reach the level of positive temperature hardening cement pastes by giving sufficient negative temperature hardening time.

Moreover, the mass loss between 100-250 °C was calculated to estimate the content of C-S-H gel with reference to the Refs. [20,21]. The C-S-H gel content of cement pastes cured at +20 °C and -5 °C is presented in Fig. 2. Unlike the hydration degree, the C-S-H gel content of negative temperature hardening cement pastes are always lower than those of positive temperature hardening cement pastes. As the hydration age increases, the gap of C-S-H gel content gradually shortens, but this gap still exists until 120 days of hydration.
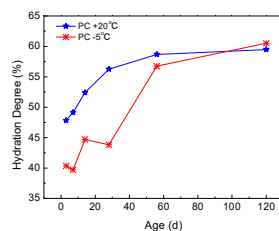
Fig. 1. Hydration degree
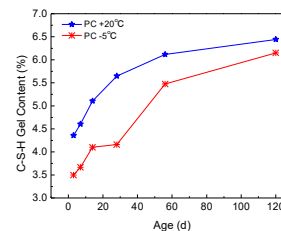
Fig. 2. C-S-H gel content

3.2 Pore size distribution

The pore size distribution curves measured by the MIP method are shown in Fig. 5 for cement pastes cured at +20 °C and -5 °C. It can be seen intuitively that negative temperature hardening changes the pore size distribution of cement paste. The "Twin Peaks" is observed in positive temperature hardening cement pastes (Fig. 3a). The main peak located at 30-80 nm, and the secondary peak located at 80-200 nm. For negative temperature hardening cement pastes (Fig. 3b), the "Twin Peaks" disappeared and the single main peak located at the secondary peak position of positive temperature hardening cement paste, indicating that negative temperature hardening causes the main peak to move forward. The forward movement of the main peak also proves that negative temperature hardening can coarsen the pore diameter of cement matrix. In addition, the 120-day pore size distribution of negative temperature hardening cement pastes also appear in the form of "Twin Peaks", which may be the result of sufficient negative temperature hardening time.
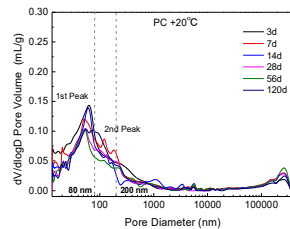
Fig. 3a. Positive temperature hardening   Fig. 3b. Negative temperature hardening
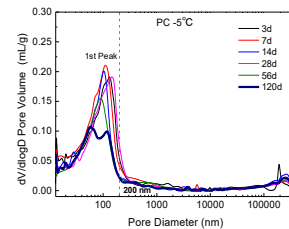
3.3 Characteristic parameters of pore structure

In Fig. 4a, the total porosity of negative temperature hardening cement paste is much higher than that of positive temperature hardening cement paste. In Fig.4b, the most probable pore diameter (corresponding to the peak position of pore size distribution) of negative temperature hardening cement paste is 1.5~2.0 times larger than that of positive temperature hardening cement paste. In Fig. 4c, the median pore diameter of negative temperature hardening cement paste is obviously higher than that of positive temperature hardening cement paste before 56 days. The median pore diameter represents the diameter value at 50% cumulative intrusion volume, which reflects the relative proportion of capillary pores in the overall pore size distribution [22]. This result indicates that negative temperature hardening increases the capillary pore fraction. In Fig. 4d, the threshold pore diameter of negative temperature hardening cement paste is slightly higher than that of positive temperature hardening cement paste. The above results show that negative temperature hardening can significantly increase the pore characteristic parameters, especially total porosity and most probable pore diameter, indicating that negative temperature hardening seriously affects the compactness of pore structure. Meanwhile, as the hydration age increases to 120 days, the pore characteristic parameters of negative temperature hardening cement pastes can approach the level of positive temperature hardening cement pastes.
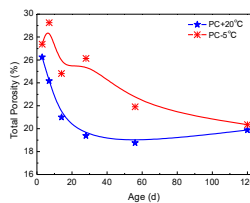
Fig. 4a. Total porosity   Fig. 4b. Most probable pore   Fig. 4c. Median pore   Fig. 4d. Threshold pore
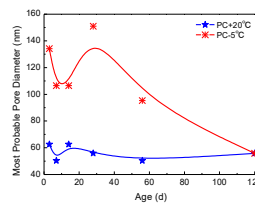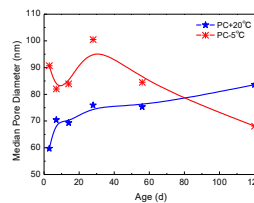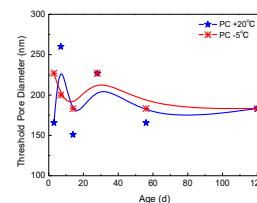
4. Conclusions

Negative temperature hardening severely inhibits the hydration reaction, significantly decreasing in the hydration degree and C-S-H gel content. However, as the hydration age increases to 120 days, the hydration degree of negative temperature hardening cement paste can reach the positive temperature

level, while the C-S-H gel content is still lower than the positive temperature level. It is also indicated that the inhibition effect of negative temperature hardening on the hydration degree and hydration products is different.

Negative temperature hardening delays the development of pore structure and significantly increases total porosity and most probable pore diameter, which seriously affects the compactness of pore structure. Similar to the hydration degree, by giving sufficient negative temperature hardening time, the pore characteristic parameters of negative temperature hardening cement pastes can approach the level of positive temperature hardening.

References

[1]   Kim, J. K. , Moon, Y. H. , & Eo, S. H. . (1998). Compressive strength development of concrete with different curing time and temperature. Cement and Concrete Research, 28(12), 1761-1773.

[2]   Kjellsen, K. O. , & Detwiler, R. J. . (1993). Later-age strength prediction by a modified maturity model. Aci Materials Journal, 90(3), 220-227.

[3]   Carino, N. J. . (1981). Temperature effects on the strength-maturity relation of mortar. Concrete.

[4]   Hafiz, M. A. , Skibsted, J. , & Emmanuel Denarié. (2020). Influence of low curing temperatures on the tensile response of low clinker strain hardening uhpfrc under full restraint. Cement and Concrete Research, 128, 105940.

[5]   Ulm FJ, Coussy O. . (1995). Modelling of thermo-chemo-mechanical couplings of concrete at early ages. ASCE J Eng Mech, 121(7), 785–94.

[6]   Ulm FJ, Coussy O. . (1996). Strength growth as chemo-plastic hardening in early age concrete. ASCE J Eng Mech, 122(12), 1123–32.

[7]   Cervera, M. , Faria, R. , Oliver, J. , & Prato, T. . (2002). Numerical modelling of concrete curing, regarding hydration and temperature phenomena. Computers & Structures, 80(18-19), 1511-1521.

[8]   Pang, X., Sun, L., Chen, M., Xian, M., Cheng, G., Liu, Y., & Qin, J. (2022). Influence of curing temperature on the hydration and strength development of Class G Portland cement. Cement and Concrete Research, 156, 106776.

[9]   Wang, X., & Lee, H. (2012). Evaluation of the mechanical properties of concrete considering the effects of temperature and aging. Construction and Building Materials, 29, 581-590.

[10] Park, K. B., Jee, N. Y., Yoon, I. S., & Lee, H. S. (2008). Prediction of temperature distribution in high-strength concrete using hydration model. ACI Materials Journal, 105(2), 180.

[11] Mehta, P. K., & Monteiro, P. J. (2014). Concrete: microstructure, properties, and materials. McGraw-Hill Education.

[12] Poon, C. S. , Wong, Y. L. , & Lam, L. . (1997). The influence of different curing conditions onthe pore structure and related properties of fly-ash cement pastes and mortars. Construction & Building Materials, 11(7/8), 383-393.

[13] Abbas, A. , Carcasses, M. , & Ollivier, J. P. . (1999). Gas permeability of concrete in relation to its degree of saturation. Materials & Structures, 32(215), 3-8.

[14] Kumar, R. , & Bhattacharjee, B. . (2003). Porosity, pore size distribution and in situ strength of concrete. Cement and Concrete Research, 33(1), 155-164.

[15] Bhattacharjee, R. K. . (2004). Assessment of permeation quality of concrete through mercury intrusion porosimetry. Cement and Concrete Research.

[16] Das, Bibhuti & Kondraivendhan, Ba. (2012). Implication of pore size distribution parameters on compressive strength, permeability and hydraulic diffusivity of concrete. Construction and Building Materials. 28. 382-386.

[17] ASTM C305-14. Standard practice for cmechanical mixing of hydraulic cement pastes and mortars of plastic consistency. Philadelphia: American Society for Testing and Materials; 2014.

[18] R. Yu, P. Spiesz, H. J. H. Brouwers, Effect of nano-silica on the hydration and microstructure development of ultra-high performance concrete (uhpc) with a low binder amount. Construction & Building Materials, 65(9), (2014), 140-150.

[19] L. Lam, Y. L. Wong, C. S. Poon, Degree of hydration and gel/space ratio of high-volume fly ash/cement systems. Cement & Concrete Research, 30(5), (2000), 747-756.

[20] M. Berra, F. Carassiti, T. Mangialardi, A. E. Paolini, M. Sebastiani, Effects of nanosilica addition on workability and compressive strength of portland cement pastes. Construction & Building Materials, 35(none), (2012), 666-675.

[21] C. Alonso, L. Fernandez, Dehydration and rehydration processes of cement paste exposed to high temperature environments. Journal of Materials Science, 39(9), (2004), 3015-3024.

[22] Zeng, Q. , Li, K. , Fen-Chong, T. , & Dangla, P. . (2012). Pore structure characterization of cement pastes blended with high-volu me fly-ash. Cement & Concrete Research, 42(1), 194-204.

The 16th International Congress on the Chemistry of Cement 2023 (ICCC2023)
"Further Reduction of CO_2 -Emissions and Circularity in the Cement and Concrete Industry"
September 18–22, 2023, Bangkok, Thailand

Assessing the Behaviour of Eco-Efficient Concrete Proportioned through Particle Packing Models (PPMs) against Carbonation

M.T. de Grazia[1*], L.F.M. Sanchez[2], and A. Leemann[3]

[1] *University of Ottawa, Ottawa, Canada*
Email: mayra.grazia@uottawa.ca
[2] *University of Ottawa, Ottawa, Canada*
Email: leandro.sanchez@uottawa.ca
[3] *EMPA - Swiss Federal Laboratories for Materials Science and Technology, Dübendorf, Switzerland*
Email: andreas.leemann@empa.ch

ABSTRACT

Using particle packing models (PPMs) along with limestone fillers has been verified as an effective approach to proportion eco-efficient concrete mixtures (i.e., reduced amount of Portland cement) demonstrating suitable performance in the fresh and short-term hardened states. However, reducing Portland cement and increasing limestone fillers may reduce the pH of concrete, which may raise some concerns about concrete durability and long-term aspects, particularly related to carbonation. This work aims to evaluate the performance of three eco-efficient mixtures proportioned with varying cement (i.e., 250, 200, and 150 kg/m³) and inert filler contents against accelerated carbonation. Specimens from the above mixtures were manufactured and stored in an accelerated carbonation chamber at 20ºC, 57% RH and 4% CO_2; the specimens were monitored over time and at 0, 7, 28, and 63 days, a phenolphthalein tracer was used to determine carbonation depth according to the Swiss standards (SIA 262/1:2019 – Annex I). The carbonation coefficients were calculated and compared with concrete bearing a higher carbon footprint (i.e., higher PC and lower limestone filler contents).

KEYWORDS: *Particle packing models (PPMs), limestone fillers, durability, carbonation.*

1. Introduction

Concrete Net Zero is a global initiative aiming to reduce greenhouse gases (GHG) by 15MTs by 2030 before reaching 100% zero emission by 2050 (GCCA, 2022). Concrete production accounts for more than 7% of global CO_2 emissions. Although the primary Net Zero goals are revolved around concrete global emissions, replacing Portland cement (OPC) with supplementary cementitious materials (SCMs) and ground limestone fillers will be critical to the plan's success, as cement production accounts for nearly 6.5% of annual CO_2 emissions (GCCA, 2021). In terms of concrete production total CO_2 emissions, savings in cement and binders may account for a 9% reduction in CO_2 emissions (350Mt CO_2), while improvements in concrete production efficiency may achieve a minimum of 11% reduction in CO_2 emissions (430Mt CO_2). Optimization of concrete mix-design and constituents are the two main subjects described in the Net Zero plan (GCCA, 2021). Past investigations confirmed that eco-efficient concrete mixtures may be designed through particle packing models (PPMs) (De Grazia et al., 2023). Yet, further improvements are seen when combining this mix-design technique with cement replacement materials resulting in GWP lower than 300 kg CO_{2eq} (De Grazia et al., 2023). While the benefits of sustainability are achieved by reducing cement and using industry by-products (i.e., SCMs and inert fillers), fresh and hardened state performance is also maintained when the mix design of concrete is optimized using PPMs. However, for a material to be deemed sustainable, it needs to maintain or surpass durability specifications and long-term performance. PPMs are used to enhance the system's granular skeleton by reducing concrete's porosity (Fennis & Walraven, 2012) which may result in an improvement in concrete performance against distinct deterioration mechanisms (i.e., carbonation, corrosion, freezing and thawing, etc.). However, lowering the

cement content and using limestone fillers may have a negative impact on carbonation. The ability of concrete to protect reinforcement bars from the penetration of carbon dioxide is known as concrete carbonation resistance (Lo & Lee, 2002). It was concluded that when Portland cement is directly replaced by limestone fillers, the carbonation rate increases when compared to concrete with the same w/c (Phung et al., 2015), whereas other studies found no significant effect on concrete carbonation resistance when up to 15% (Lollini et al., 2014) and 35% (Tsivilis et al., 2002) limestone filler was used. This study aims to assess carbonation resistance of eco-efficient concrete mixtures developed with PPMs and containing limestone fillers as the main cement replacement.

2. Experimental procedures

2.1 Materials
This study was developed based on the most recent continuous particle packing model, Alfred model, which is also known as modified Andreasen (1).

$$CPFT = 100 * \left(\frac{D_P{}^q - D_S{}^q}{D_L{}^q - D_S{}^q} \right) \tag{1}$$

where D_P is the particle size in question, CFPT is the cumulative percent finer than D_P, D_L and D_S is the largest and smallest particle size in the system, respectively, and q is a distribution factor (q-factor).

Following the advances in the fresh state behaviour of a previous study (T. de Grazia et al., 2019), the Alfred model particle size distribution range was divided into two parts: powder portion (from D_S to largest diameter available within the powders selected) and aggregate portion (from the smallest diameter of aggregates to D_L). A q-factor of 0.34 and 0.31 ± 0.1 in the powder and aggregate portions, respectively, were chosen in order to achieve the lowest dry porosity (determined through the Westman and Hugill algorithm (Funk & Dinger, 1994).
To further improve the sustainability of the system, two types of limestone fillers were also used in the mixtures: 1) a performance filler (P-filler) and 2) a replacement filler (R-filler) having a particle size distribution smaller than and similar to that of the Portland cement used in this study, respectively. In this case, the ideal amount of P-filler was then determined using the least squares method considering the powder's portion with a q-factor of 0.34. The water-to-cement ratios were selected based on three commonly used compressive strengths in the concrete industry, namely 20, 30, and 40 MPa. Mixtures containing cement content equal to or higher than 250 kg/m³ had an average compressive strength of 39 MPa and a standard deviation (SD) of 2.7, whereas mixtures with 200 and 150 kg/m³ of cement achieved compressive strengths of 33 MPa (SD = 1.3) and 23 MPa (2.3), respectively. Additionally, Portland cement (GU), natural sand, and granite coarse aggregates with a nominal maximum size of 19 mm were used to design the concrete mixtures. To improve the flowability of the concrete mixtures, a polycarboxylate-based high-range (SP) water reducer and a lignosulfonate-based mid-range plasticizer (MR) were used as needed. Table 1 presents the mix design of the control mixture developed with ACI-method (1C-420A) and four sustainable mixtures developed with the PPM-method (i.e., 2C-325P, 3C-250P, 4C-200P, and 5C-150P). The concrete mixtures were labelled according to the amount of cement and mix design (i.e., A: ACI-method and P: PPM method), with label 1C-420-A indicating the mixture with the highest amount of cement (420 kg/m³) developed using the ACI method, and label 5C-150-P indicating the mixture with the lowest amount of cement (150 kg/m³) developed using the PPM method.

2.2 Methods
Concrete cylinders were manufactured and moisture cured for 28 days. The carbonation resistance was appraised using a carbonation chamber setup containing a gas mixture of 4% of CO_2 and a temperature of 20 +/- 1ºC and relative humidity (RH) of 57 +/- 3%, as per SN 505 262/1. Carbonation depth was determined at 0, 7, 28, and 63 days. At each time point, an approximately 2.5 cm slice of the sample was split off and the non-exposed surface was sprayed with phenolphthalein and photographed. 20 carbonation depths were performed as per SIA 262/1:2019 – Annex I at each time point and the carbonation coefficient (K_{ACC}) was calculated through Equation (2).

$$K_{ACC} = (d_K - A)/\sqrt{t} \tag{2}$$

where K_{ACC} is the carbonation coefficient in mm/y$^{1/2}$, d_K is the carbonation depth in mm, A is the initial carbonation depth after curing in mm, and t is the time in years.

Table 1. Mix-design of eco-efficient concrete mixtures.

									kg/m³								
		Powder				**Fine Aggregate**					**Coarse Aggregate**						
Mix-name	PC	Filler P	Filler R	0.15-0.30 mm	0.30-0.60 mm	0.60-1.18 mm	1.18-2.36 mm	2.36-4.75 mm	4.75-9.5 mm	9.5-12.5 mm	12.5-19 mm	Water	w/p*	SP	MR
1C-420A	420	0	0	860	0	0	0	0	311	302	302	189	0.45	0	0
2C-325P	325	0	0	132	163	197	250	313	376	173	293	179	0.55	1.9	1.9
3C-250P	250	41	33	137	170	205	260	326	392	180	306	145	0.45	3.9	3.2
4C-200P	200	42	81	141	174	210	267	334	402	184	313	124	0.38	0	0
5C-150P	150	42	122	144	177	213	268	333	397	182	308	126	0.40	0	0

*w/p refers to water-to-powder ratio, that is, the total of water divided by the total powder mass (cement + limestone fillers)

3. Results and Discussion

3.1 Phenolphthalein Indicator – qualitative analysis

As previously discussed by (Leemann et al., 2015; Leemann & Moro, 2017), the carbonation resistance is highly affected by cement type and w/CaO, which expresses the CO_2 buffer capacity per volume of cement paste. Moreover, the influence of the limestone filler on the carbonation rate is still debated; a recent study found that the CO_2 uptake is increased for samples made with limestone fillers even though the initial permeability is reduced due to the filler effect (Phung et al., 2015), which may be partially explained by the nucleation sites for calcite precipitation which aids the increase of portlandite carbonation. Conversely, (Lollini et al., 2014) concluded that the carbonation rate is similar for concrete presenting similar compressive strength regardless of the percentage of limestone fillers added to the mixture. The propagation of the carbonation front obtained in the samples studied in this work can be seen in Figure 1. The phenolphthalein spray test reveals a consistent carbonation front in concrete 1C-420A, whereas increasing the limestone filler results in a faster-progressing carbonation front at the same time. Analyzing mixtures 1C-420A, 2C-325P, and 3C-250P that, despite having different w/c, achieved roughly the same compressive strength, it is clear that the higher the w/CaO and the lower the limestone percentage, the higher the carbonation depth, specially at 63-days. Yet, 3C-250P carbonation front is very foggy. Furthermore, despite having a lower w/CaO and higher limestone percentage, 4C-200P outperformed 3C-250P in carbonation resistance. As expected, the lowest carbonation resistance was achieved by 5C-150P, the only concrete mixture developed with a percentage of limestone filler greater than 40%.

Mix-name	w/c	w/CaO*	Filler (%)	0-day	7-days	28-days	63-days
1C-420A	0.45	0.73	0%				
2C-325P	0.55	0.90	0%				
3C-250P	0.58	0.94	23%				
4C-200P	0.62	1.01	38%				
5C-150P	0.84	1.37	52%				

*CaO is equal to 61.5% as per the chemical composition of PC obtained by XRF.

Figure 1. Comparison of carbonation fronts over 63 days.

3.2 Carbonation depth – quantitative analysis

The carbonation depth of the concrete mixtures appraised in this work is illustrated in Figure 2. Following the results presented in section 2.1, 1C-420A displayed the highest carbonation resistance, followed by 2C-325P, and 4C-200P. Surprisingly, 5C-150P performed similarly to 3C-250P over the 63-day test. When the

carbonation coefficient K_{ACC} was calculated using Equation (2), the values were 2.17, 21.12, 48.48, 33.87, and 57.41 mm/y$^{1/2}$ for 1C-420A, 2C-325P, 3C-250P, 4C-200P, and 5C-150P, respectively (Figure 3). Although there is a trend between the carbonation coefficient and the mixtures studied, more research is needed to fully understand the behaviours verified, particularly 3C-250P. However, as previously stated, the carbonation front of 3C-250P is cloudy which could have contributed to the uncertainty of K_{ACC} presented in Figure 3. It is worth noting that in this case, because no SCMs were added to the mixtures, w/CaO and w/c have the same relationship to carbonation resistance. Although mixtures 1C-420A, 2C-325P, and 3C-250P had similar compressive strengths, their carbonation depths were incompatible.
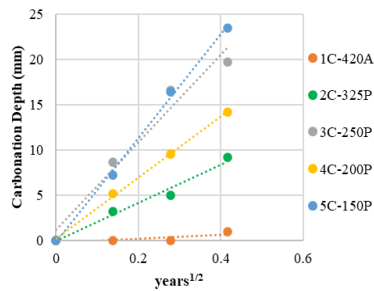
Figure 2. Comparison of carbonation depths.
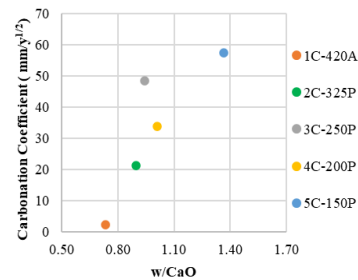
Figure 3. Carbonation coefficient K_{ACC}.

4. Conclusions

As previously verified by (Leemann et al., 2015), the carbonation resistance of the mixtures evaluated presented a direct relationship with their w/CaO ratios, where the higher the w/CaO, the higher the carbonation coefficient and the lower the carbonation resistance, except for 3C-250P which appears to be an outlier.

References

De Grazia, M. T., Sanchez, L. F. M., & Yahia, A. (2023). Towards the design of eco-efficient concrete mixtures: An overview. *Journal of Cleaner Production*, *389*(January), 135752. https://doi.org/10.1016/j.jclepro.2022.135752

Fennis, S. A. A. M., & Walraven, J. C. (2012). Using particle packing technology for sustainable concrete mixture design. *Heron*, *57*(2), 73–101.

Funk, J. E., & Dinger, D. R. (1994). *Predictive process control of crowded particulate suspensions* (S. S. & B. Media (ed.); 1st ed.). https://doi.org/10.1007/978-1-4615-3118-0

GCCA. (2021). *Concrete Future - Roadmap to Net Zero*. https://gccassociation.org/concretefuture/wp-content/uploads/2021/10/GCCA-Concrete-Future-Roadmap-Document-AW.pdf

GCCA. (2022). *Our path to net zero*. https://gccassociation.org/concretefuture/our-path-to-net-zero/

Leemann, A., & Moro, F. (2017). Carbonation of concrete: the role of CO2 concentration, relative humidity and CO2 buffer capacity. *Materials and Structures*, *50*(1). https://doi.org/10.1617/s11527-016-0917-2

Leemann, A., Nygaard, P., Kaufmann, J., & Loser, R. (2015). Relation between carbonation resistance, mix design and exposure of mortar and concrete. *Cement and Concrete Composites*, *62*, 33–43. https://doi.org/10.1016/j.cemconcomp.2015.04.020

Lo, Y., & Lee, H. M. (2002). Curing effects on carbonation of concrete using a phenolphthalein indicator and Fourier-transform infrared spectroscopy. *Building and Environment*, *37*(5), 507–514. https://doi.org/10.1016/S0360-1323(01)00052-X

Lollini, F., Redaelli, E., & Bertolini, L. (2014). Effects of portland cement replacement with limestone on the properties of hardened concrete. *Cement and Concrete Composites*, *46*, 32–40. https://doi.org/10.1016/j.cemconcomp.2013.10.016

Phung, Q. T., Maes, N., Jacques, D., Bruneel, E., Van Driessche, I., Ye, G., & De Schutter, G. (2015). Effect of limestone fillers on microstructure and permeability due to carbonation of cement pastes under controlled CO2 pressure conditions. *Construction and Building Materials*, *82*, 376–390. https://doi.org/10.1016/j.conbuildmat.2015.02.093

T. de Grazia, M., F. M. Sanchez, L., C. O. Romano, R., G. Pileggi, R., de Grazia, M. T., Sanchez, L., Romano, R. C. O., Pileggi, R. G., T. de Grazia, M., F. M. Sanchez, L., C. O. Romano, R., & G. Pileggi, R. (2019). Investigation of the use of continuous particle packing models (PPMs) on the fresh and hardened properties of low-cement concrete (LCC) systems. *Construction and Building Materials*, *195*, 524–536. https://doi.org/10.1016/j.conbuildmat.2018.11.051

Tsivilis, S., Chaniotakis, E., Kakali, G., & Batis, G. (2002). An analysis of the properties of Portland limestone cements and concrete. *Cement and Concrete Composites*, *24*(3–4), 371–378. https://doi.org/10.1016/S0958-9465(01)00089-0

The 16th International Congress on the Chemistry of Cement 2023 (ICCC2023)
"Further Reduction of CO_2 -Emissions and Circularity in the Cement and Concrete Industry"
September 18–22, 2023, Bangkok, Thailand

Resistance of portland-dolomite cement to thaumasite sulfate attack

Jiangtao Xu[1], Duyou Lu[1], and R.D. Hooton[2]

[1] *Nanjing Tech University, Nanjing, China*
Email: xujiangtao18@163.com

[2] *University of Toronto, Toronto, Canada*
Email: d.hooton@utoronto.ca

ABSTRACT

The use of dolomite, $CaMg(CO_3)_2$, to manufacture portland-dolomite cement (PDC) has recently attracted interest as a promising low-carbon cement alternative to portland-limestone cement. However, little is known about the potential for thaumasite sulfate attack in portland-dolomite cement. This study investigated the resistance to thaumasite sulfate attack of PDC with 0~30% dolomite powder exposed to 50g/L Na_2SO_4 solution at 23°C and 5°C, and using portland-limestone cement (PLC) as a comparison. The expansion of mortar bars was measured periodically, and hydration products of cement pastes were examined using X-ray diffraction. The portland cement used had a C_3A = 10% and thus was not sulfate resistant, but results showed that the sulfate resistance of mortar stored at both 23°C and 5°C decreased significantly as dolomite and limestone additions increased. In contrast to limestone, dolomite exhibits a smaller adverse effect on sulfate resistance. When exposed to extremely high sulfate concentrations at low temperatures, PDC made with high C_3A cement is similarly vulnerable to thaumasite sulfate attack to PLC.

KEYWORDS: *thaumasite, sulfate attack, dolomite powder, expansion*

1. Introduction

Conventional sulfate attack proceeds as cement hydrate phases interact with external sulfates to form ettringite and gypsum, which can cause expansion and cracking of cementitious materials. Thaumasite sulfate attack (TSA) is a special form of sulfate attack with thaumasite ($CaSiO_3 \cdot CaCO_3 \cdot CaSO_4 \cdot 15H_2O$) as the deterioration product, that can destroy the C-S-H matrix and transform concrete into a white, non-cohesive mass without any binding properties, which is more severe than conventional sulfate attack. TSA has been reported in Norway, the United States, Canada, France, Germany, Austria, Denmark, and China since its discovery in the 1990s, attracting much attention from both academia and industry (Shi 2012). Thaumasite requires a source of calcium silicate, sulfate, carbonate and excess humidity. It has been shown that low temperature, magnesium sulfate exposure, high-C_3A content in cement, as well as the presence of carbonates may accelerate and promote thaumasite formation (Rahman 2014). The mechanism of thaumasite formation can be both direct and indirect. Thaumasite can be formed directly by a reaction between C-S-H, sulfate, carbonate and water or indirectly by an ettringite transformation due to the structural similarities of two compounds.

Portland-limestone cement (PLC) has been extensively used in building and construction due to its economic, environmental and technical benefits, such as low cost, reduced CO_2 emissions, improved workability, high early strength, and increased formation of hydrates of hemicarbonate and monocarbonate (Wang 2018). However, because PLC is susceptible to TSA, especially at cool temperatures, it is not recommended for sulfate exposure unless used together with sufficient levels of suitable supplementary cementitious materials (SCMs). As an internal source of carbonate, the limestone in PLC can dissolve CO_3^{2-} into cement pore solution and enhance the formation of thaumasite, increasing the risk of TSA (Hooton 2007, Ramezanianpour 2013). However, when appropriate levels of SCMs were used, PLC containing up to 15% limestone performed as well as Portland cement made from the same

clinker in long-term sulfate exposure of concrete at low temperatures (Hooton and Thomas 2016).

Dolomite is a common carbonate rock that often coexists with limestone. Recently, the use of dolomite to produce Portland-dolomite cement (PDC) has received interest as a promising modification of low-carbon portland-limestone cement. Previous studies (Zajac 2014, Xu 2022) have shown that the addition of dolomite may accelerate the hydration of cement and improve early strength, and also result in the formation of carboaluminates and, as a result, ettringite stabilization, which is similar to the behaviour of limestone. Magnesium from dolomite can react to produce increased amounts of hydrotalcite and brucite, potentially increasing the compressive strength of mortar and improving volume stability. In addition, several studies demonstrated that PDC exhibited comparable durability to PLC in terms of chloride penetration and carbonation (Zhang 2022). However, there is little research on the sulfate resistance of PDC, particularly with respect to TSA, which may be favored by the carbonate ions from dolomite. Besides, a field case of TSA occurred in concrete made using dolomite aggregates (Mittermayr 2017).

In this study, the sulfate resistance of portland-dolomite cement with various dolomite contents was evaluated both at 5℃and 23℃, with portland-limestone cement as a comparison. Also, hydration products formed after the sulfate attack on the samples were examined using X-ray diffraction (XRD).

2. Materials and methods

Canadian CSA A3000 Type GU cement, dolomite and limestone were used in this study. The chemical compositions of the raw materials are given in Table 1. The mineralogical composition of the cement by Bogue formula is 53%C_3S, 17%C_2S, 10%C_3A and 8%C_4AF, and so this cement would not be sulfate resistant. The dolomite and limestone powders contained about 93% CaMg $(CO_3)_2$ and 92% $CaCO_3$, and their median particle sizes are about 6 μm and 8 μm, respectively (data provided by supplier). ASTM standard graded Ottawa sand was used for casting mortar samples.

Table 1 Chemical composition of raw materials (wt%)

Materials	CaO	SiO_2	Al_2O_3	Fe_2O_3	MgO	SO_3	K_2O	Na_2O	LOI
Cement	62.20	19.70	5.30	2.60	2.40	2.90	0.62	0.12	2.10
Dolomite	31.45	1.36	0.34	0.10	21.23		0.03		45.06
Limestone	54.48	0.26	0.17	0.03	1.38		0.02	0.06	43.62

Dolomite and limestone replaced cement at 0%, 5%, 15% and 30% by mass, respectively. For all mixtures, mortars with a water/binder/sand ratio of 0.485:1:2.75 were cast into 25×25×285mm prism (for length change) and 50mm cube (for compressive strength) moulds. Paste samples with a water/binder ratio of 0.50 were cast into 12 mm diameter plastic cylinders. After 24 hours, all samples were demolded and stored in tap water at room temperature. These samples were divided into two groups. The first group was immersed in 50g/L Na_2SO_4 solution at 23℃ after the mortars attained a strength of 20MPa (as per ASTM C1012), and the second group was immersed in the same solution at 5℃ after being pre-cured at room temperature for 28 days. The length change of the samples was recorded periodically, and the sulfate solution was renewed every month.

The hydration products of cement pastes were examined by X-ray diffraction. At the selected age, the pastes were crushed and stored in excess ethanol for 24 hours to arrest hydration, and then dried in a desiccator at 40℃ for 24 hours. X-ray diffraction was performed on SmartLabTM 3Kw Powder Diffractometer (Cu Kα1, λ=1.5406 Å) with operation conditions of 40kV and 30mA. The scan speed was set to 5 º/min with a step size of 0.02 °.

3. Results and discussion

3.1 Expansion and visual observations after sulfate exposure at 23 ℃ and 5℃

Fig. 1 show the average length change for mortar bars exposed to 5% Na_2SO_4 solution at 23 ℃ (Fig. 1a) and 5℃ (Fig. 1b). As shown in Fig. 1a, as expected, all of the mortar bars exposed to sulfates at 23℃ exceeded the 0.10% expansion limit before 6 months, due to the high C_3A content of the cement used. After 90 days of exposure, the incorporation of dolomite and limestone in cement significantly reduced the onset time of expansion and increased expansion of the mortars, with higher carbonate content resulting in greater expansions. In comparison to the PLC samples, the PDC mortar bars expanded less. After 210 days, the expansion of PDC5, PDC15 and PDC30 were 0.23%, 0.39% and 0.72%, respectively, whereas the respective expansions of PLC5, PLC15 and PLC30 were 0.29%, 0.60% and 1.06%. For

sulfate attack at 5°C (Fig. 1b), all samples had fractured and disintegrated after 150 days of exposure, exhibiting a more severe attack at lower temperature than at room temperature. It is obvious that a higher carbonate content caused the mortar to fracture sooner. PDC30 and PLC30 began to fracture as early as after 90 days of exposure, PDC15 and PLC15 fractured at 120 days, and GU, PDC5 and PLC5 fractured at 150 days. The expansions of the PDC samples were smaller than those of the PLC samples, although having an equivalent failure time. Moreover, PDC exhibited less visual degeneration than PLC, where mush appeared (Fig. 2). While all mixtures failed, both dolomite and limestone additions further reduced the sulfate resistance of mortar, especially at low temperatures, but dolomite had a less adverse effect on the sulfate attack than limestone.
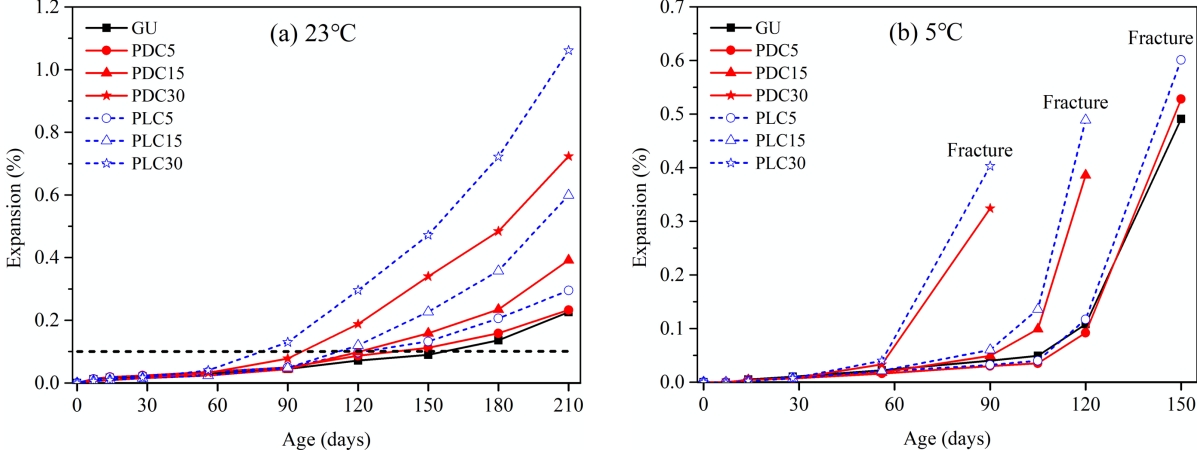
Fig. 1 Length changes for mortar bars exposed to 5% Na_2SO_4 solution at (a) 23 °C and (b) 5°C

Fig. 2 Visual condition of mortar bars immersed in 5% Na_2SO_4 solution at 5°C for 150 days

3.2 Hydration products after sulfate attack at 23 °C and 5°C

Fig. 3a and b show the XRD patterns of paste samples exposed to 5% Na_2SO_4 solution at 23 °C and 5°C, respectively. Ettringite, gypsum, and portlandite were the primary hydration products that formed after 28 days and 180 days of exposure at 23°C (Fig. 3a). The intensities of ettringite and gypsum peaks clearly increased with increasing exposure time, and the PDC and PLC samples, notably the PLC samples, had higher peaks of ettringite and gypsum than the reference GU cement. For the samples exposed at 5 °C (Fig. 3b), ettringite and gypsum were also observed after 28 days of exposure, which is similar to the observation at 23 °C. At 150 days, however, thaumasite was formed in addition to the increase in ettringite and gypsum peaks, and its peaks were significantly increased with the addition of both types of carbonate powders. The formation of thaumasite was more pronounced in the PLC samples when compared to the PDC samples. Furthermore, a significant decrease in portlandite was observed in both the PDC and PLC samples, which can be associated with the enhanced gypsum formation. This demonstrates that, similar to PLC, PDC can suffer from conventional ettringite sulfate attack at room temperature, and initial ettringite attack with late formation of thaumasite at the lower temperature. The lower expansions

of PDC bars compared to PLC are attributable to the lower amounts of corrosion products formed in the cement matrix.
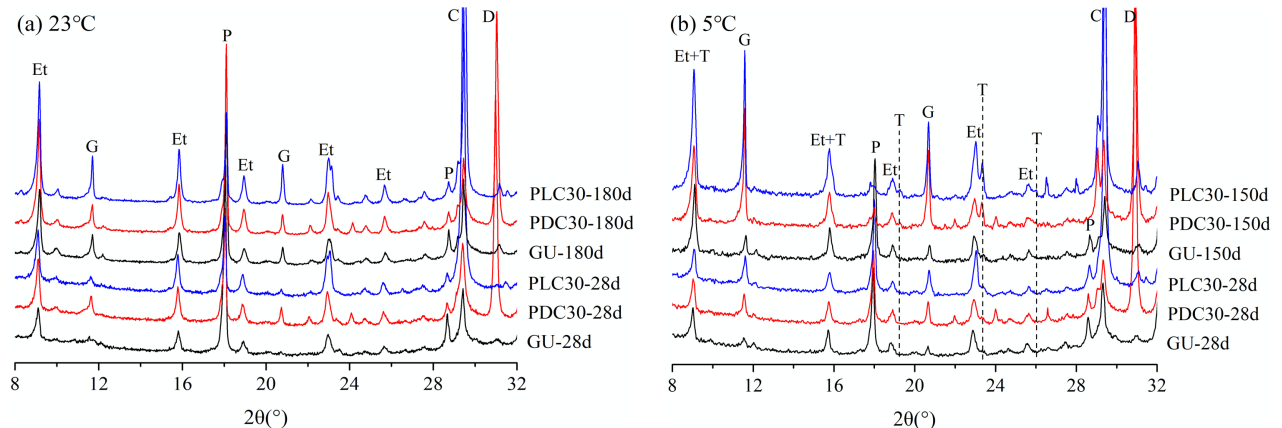
Fig. 3 XRD patterns of paste samples exposed to 5% Na$_2$SO$_4$ solution at (a) 23 °C and (b) 5°C

3. Conclusions

This study investigated the influence of dolomite additions to portland cement on the sulfate attack of mortars exposed at 5°C and 23°C, with limestone additions used for comparison. All mortar samples degraded more severely at lower temperature than at room temperature. At both exposure temperatures, the sulfate resistance of mortar was reduced as a result of dolomite incorporation into cement, with higher dolomite contents resulting in poorer sulfate resistance. However, dolomite additions had less adverse effect on sulfate resistance than limestone additions, which was related to smaller amounts of corrosion products formation in PDC. Similar to PLC, the type of destruction of PDC is conventional sulfate attack at room temperature, and at low temperatures, initial ettringite attack followed by thaumasite sulfate attack.

Acknowledgements

References

Hooton, R. D., Nokken, M., and Thomas, M.D.A. (2007) "Portland-limestone cement: state-of-the-art report and gap analysis for CSA A 3000", *report prepared for St. Lawrence Cement*.

Hooton, R.D. and Thomas, M.D.A., (2016) "Sulfate Resistance of Mortar and Concrete Produced with Portland-Limestone Cement and Supplementary Cementing Materials", Portland Cement Association Research Report SN3285, 2016, 25pp.

Mittermayr, F., et al. (2017) "Environmental controls and reaction pathways of coupled de-dolomitization and thaumasite formation", *Cement and Concrete Research*, 95: 282-293.

Rahman, M.M., and Bassuoni, M.T. (2014) "Thaumasite sulfate attack on concrete: Mechanisms, influential factors and mitigation", *Construction and Building Materials*, 73: 652-662.

Ramezanianpour, A.M. and Hooton, R.D. (2013) "Thaumasite sulfate attack in Portland and Portland-limestone cement mortars exposed to sulfate solution", *Construction and Building Materials*, 40: 162-173.

Shi, C., Wang, D. and Behnood, A. (2012) "Review of thaumasite sulfate attack on cement mortar and concrete", *Journal of materials in civil engineering*, 12: 1450-1460.

Wang, De., et al. (2018) "A review on use of limestone powder in cement-based materials: Mechanism, hydration and microstructures", *Construction and Building Materials*, 181: 659-672.

Xu, J., et al. (2022) "Volume stability of Portland-dolomite cement pastes cured in different conditions", *Journal of Sustainable Cement-Based Materials*, 1-13.

Zajac, M., et al. (2014) "Effect of CaMg (CO$_3$)$_2$ on hydrate assemblages and mechanical properties of hydrated cement pastes at 40 C and 60 C", *Cement and concrete research*, 65: 21-29.

Zhang X., Yu L., and Wu Y. (2022) "Research on the carbonation resistance of concretes containing dolomite powder", *Fullerenes, Nanotubes and Carbon Nanostructures*, 1-12.

The 16th International Congress on the Chemistry of Cement 2023 (ICCC2023)
"Further Reduction of CO$_2$ -Emissions and Circularity in the Cement and Concrete Industry"
September 18–22, 2023, Bangkok, Thailand

Contribution of the thermochemical conversion kinetics to predict the mass transfer of hydraulic binders panels submitted to fire

E. Huby[1], A. Rojo[2], D. Giovannacci[1], J-D. Mertz[1], and Y. Mélinge[1*]

[1] *Laboratoire de Recherche des Monuments Historiques (LRMH), CRC – MNHN, CNRS, Ministère de la Culture – UAR 3224, Champs sur Marne, France*

Email: emilie.huby@culture.gouv.fr, david.giovannacci@culture.gouv.fr, jean-didier.mertz@culture.gouv.fr, yannick.melinge@culture.gouv.fr

[2] *Université de Reims Champagne-Ardennes, Reims, France*

Email: amandine.rojo@univ-reims.fr

ABSTRACT

Better understanding of the fire resistance is the aim with the proposed research works and, more specifically, the mass transfer identification when building materials are submitted to fire. The experimental methodology has been developed by the combination of the data recorded during a fire test at reduced scale and thermo-chemical characterization of a considered recipe. On the one hand, squared panels (550x550 mm²) with constant thickness are heated on one face using the standard fire ISO834 in order to identify the fire resistance properties and the mass change. On the other hand, chemical conversion kinetics of the studied recipe are modeled by means of iso-conversional methodologies at the micro scale. The model combines different parameters such as the temperature, the chemical state and the heat rate. Classically, the combination of the Arrhenius law and the extended Prout-Tompkins model have been used to assess the chemical conversion kinetics. The mass transfer (from exposed side to non-exposed side of the panel) is modelled and compared to the direct measurements. In order to reduce the risk with concrete characterization, such methodology has first been tested using gypsum based material often used as passive fire protection. Obtained results are well correlated with those obtained by direct mass measurement of the panel.

KEYWORDS: *Mass transfer, Fire resistance, Thermo-chemical conversion kinetics, Gypsum-based materials*

1. Introduction

A good understanding of building materials and structures behaviors submitted to fire remains today a real challenge in order to develop new materials able to resist or to increase the performances of the fire protection materials. Furthermore, the improvement of the efficiency of the characterization methodologies is also a big challenge. The present paper is a contribution to better identify experimentally the thermo-hydro-chemical and mechanical (THCM) behavior of building materials at the macro scale. A focus is devoted to the mass transfer identification and its analysis. In fact, when building material is submitted to fire, mass transfer is induced by the thermo-chemical changes. If the porous media is not well adapted, impeded mass transfer can lead to severe mechanical damages as it can be seen in concrete structure (cracks appearance, spalling, explosion…). In order to better understand the fire resistance at reduced scale, an experimental protocol has been developed to test technical solutions (macro scale) as board with constant thickness submitted to fire on one face. In the present paper a first step of the protocol is presented by taking into account of the thermo-chemical changes of the tested material and its characterization. The deduced thermo-chemical model is then used to predict the mass evolution of the board. To prevent the risk of the apparatus being destroyed during the fire test, concrete samples are replaced by gypsum based material for the present study. Such material is generally used for passive fire protection. Finally, the mass transfer is a

combination of the water departure during the dehydration period and the CO_2 departure during the decarbonation period (natural impurity in the gypsum careers). Isoconversionnal methodologies have been applied to characterize and to model the thermo-chemical conversion kinetics of the recipe.

2. Experimental protocols, materials and data treatment

2.1 Fire resistance analysis, studied material and samples

Equivalent one dimensional fire tests have been carried out by means of squared panels laid to close an horizontal electrical furnace, Mélinge et al. (2010). Standard ISO834 thermal fire is fixed on the inner side while the other side remains at the ambient conditions of the test room. Radiative flux is dominant near the exposed side of the board. Conduction regime inside the board is highlighted using thin thermocouples positioned all along the thickness. Radiative thermal flux and strains at the non exposed side are respectively recorded by an IR thermal camera and a lidar. Global damages and mass evolution are characterised after testing for fixed duration. After a cooling period, the residual properties of the panels can then be studied from the exposed to the non-exposed side, Rojo (2013). For the present study, thirty panels (550x550x40 mm) have been made by mixing a β natural hemihydrate of calcium sulfate with water (W/P = 0.65). After a curing period, the main properties of the gypsum panels can be seen in the table 1.

Table 1: Main properties of the studied material. Mix of plaster and water (W/P = 0.65).

Density (kg.m^{-3})	1095	Thermal conductivity (W.m^{-1}.K^{-1})	0.41
Average porosity (-)	0.52	Specific heat (J.K^{-1}.g^{-1})	1.24

Four thermo chemical conversions characterise gypsum material from room temperature to 1000°C, Abriel (1983), Kirfel et al. (1980). The dehydration is well characterised by two combined endothermic reactions between 80 to 200 °C. Then, anhydrite III to anhydrite II exothermic phase transition is observed between 350 and 400°C. The last reaction usually takes place between 600 and 750°C and is due to decarbonation of $CaCO_3$ impurities. Other reactions above 1000°C are not studied in the present works. At the panel scale, previous works helped us to better understand the thermo chemical changes effect along the thickness in fire condition Mélinge et al. (2011) and to describe and model the porosity kinetics, Rojo et al. (2013).

2.2 Thermo chemical changes analyses

Thermo chemical changes are analysed and modelled using thermal analyses (TG/DSC) through non isothermal protocol and for an important spectrum of heat rates which are in good accordance of the fire conditions (1 to 100 K.min^{-1}). Endothermic, exothermic reactions with and without mass variation can be then characterised. Adimensional parameter, $0 \leq \alpha \leq 1$, allows to highlight the chemical state of the recipe and its evolution is introduced. $\alpha = 0$ characterises the non chemically damaged compounds and $\alpha = 1$ characterises the total achievement of the chemical conversion. Then, the thermo-chemical kinetics are classically modelled by the equation 1 which combines the effect of the temperature and the chemical conversion mechanism.

$$\frac{d\alpha}{dt} = f(\alpha).g(T) = \alpha^m(1-\alpha)^n.k\exp^{\frac{-E_a}{RT}}$$ (1)

The temperature effect is well described by the Arrhenius law and the Prout Tompkins model (B1$_{m,n}$) generally used to characterise nucleation processes is well adapted to describe the chemical conversion. Friedman and Flynn-Owaza-Wall (FOW) methodologies combined to non-linear regression analysis have been performed to identify first the activation energy and then the three other parameters of each of gypsum chemical changes, table 2, Rojo (2013).

2.4 Data treatment methodology

When the gypsum panel is thermally loaded by the standard ISO 834, the thermal transfer is presented in the figure 1 from the exposed side to non-exposed side. Significant numbers of thermocouples are implemented along the thickness. This local instrumentation helps to better increase the accuracy of the

mesh in order to interpolate the temperature for each position along the thickness. A high correlation level between the signals helps to ensure the measurement quality and to prevent against a cell damage or the interaction of the thermocouples with cracks development during the test. Such detection during the treatment helps to reject the wrong data. Illustration of a damaged thermocouple is clearly noticed at the 25 mm position referenced from the non exposed side (important noise detection around 6000s). Thus, illustration of two thermocouples closed to a crack development can be seen at the 15 and 20 mm position; Signal deviation from the others is detected from 8000 s. After data validation, the recorded signal is well in accordance with a latent heat material thermally loaded. For a local temperature ranged from 75 to 80 C, a large thermal plateau is reached and the temperature remains constant until the dehydration front reaches the considered thermocouple. This plateau illustrates the effect of the thermal barrier induced by latent heat.

Table 2: Identification of the thermo chemical kinetics of the dihydrated of hemihydrate of calcium sulfate.
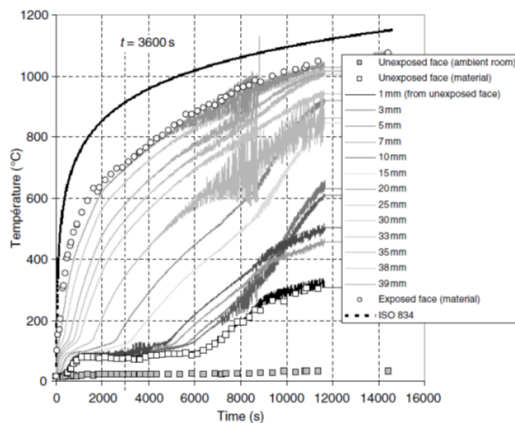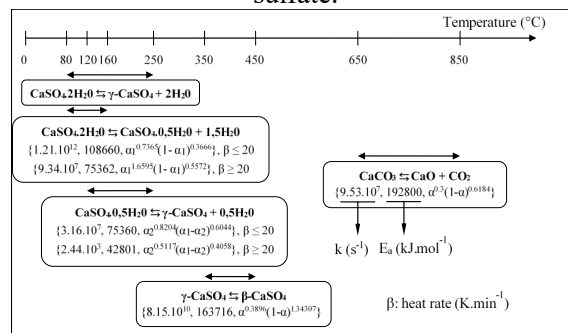
Figure 1: Thermal transfer through a gypsum board (W/P = 0.65) of 40 mm thick heated on one face using the standard ISO 834.
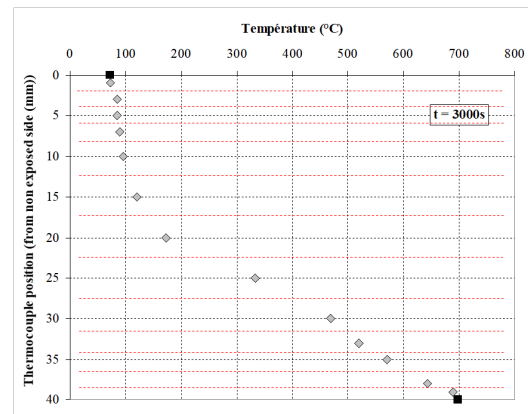
Figure 2: Illustration of the temperature evolution along the thickness at a fixed time. The red line illustrate the mesh of the mass balance.
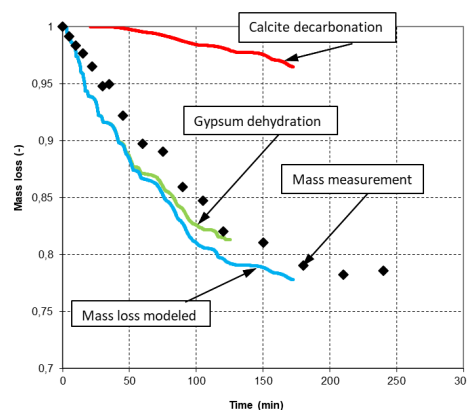
Figure 3: Gypsum board mass evolution versus time during the fire test. Comparison of the direct mass measurement and the modeled one.

From the thermal map, figure 1, temperature evolution along the board thickness can be deduced for a fixed time, figure 2. The used mesh for the mass balance is illustrated in this figure. Local mass evolution can be modeled from the thermo-chemical kinetics and the evaluation of dα/dt for the considered time, equation 2. The mass of the panel is then deduced by means of an integral calculation along the thickness and finally generalised all along the fire test.

$$\frac{d\alpha}{dt}\bigg|_t \approx \frac{(\alpha_{t+1} - \alpha_{t-1})}{2.\Delta t} \tag{2}$$

3. Results and discussion

The obtained results combining the gypsum dehydration process, the calcite decarbonation and the direct mass measurement are presented in the figure 3. Tendency showed by the calculus versus time is in good agreement with the direct measurements even if, and logically, the mass decreasing seems to be faster by the proposed calculus. This expected result helps us highlight the capability of the restricted hypothesis to only consider the chemical changes of the material to accurately reproduce the mass transfer induced by the water and CO2 disappearance. After this first step of the works, the addition of a transport equation through the porous media could improve the quality of the numerical prediction.

4. Conclusions

Dehydration and decarbonation thermo-chemical conversion models have been used to identify the mass transfer of gypsum board submitted to standard fire on one side. The obtained results are in good agreement with the direct mass measurement of the panels. Because of the present works assume the disappearance of the water vapour and the CO_2 just after the chemical conversion, transport regime of the fluid through the porous media seems to be well adapted to characterise the fluid flow regime with permeable porous media. Nevertheless, better prediction of the mass transfer should be obtained by taking into account the direct momentum equation. Such consideration is under way but a permeability level versus mechanical damages advances is needed to really consider this incorporation. Finally, such results represent a new step to better understand the THCM behaviour of building material submitted to fire including the concrete materials.

References

Mélinge, Y., Nguyen, K.S., Lanos C. (2010) "Experimental study of thermo-chemical behaviour of gypsum based material under standard ISO 834 fire condition", *European Journal of Environmental an Civil Engineering (EJECE)*, 14(5): 561-577

Mélinge, Y., Nguyen, K.S., Daiguebonne, C., Guillou, O., Freslon, S., Lanos, C. (2011) "One-Dimensional-Time Study of the Dehydration of Plasterboards Under Standard Fire Condition (ISO 834): Thermo-Chemical Analysis", *Journal of Fire Sciences,* 29(4): 299 – 316

Rojo, A., Mélinge, Y., Guillou, O. (2013) "Kinetics of internal structure evolution in gypsum board exposed to standard fire", *Journal of Fire Sciences*, 31(5): 395-409

Rojo, A. (2013) "Etude de la structuration et du comportement du gypse sous condition incendie" (2013) *PhD thesis INSA Rennes*

Abriel, VW. (1983) "Calcium Sulphate Subhydrate, CaSO4_0.8H2O", *Acta Crystallographica*; C39: 956–958.

Kirfel, A., Will, G. (1980) "Charge Density in Anhydrite CaSO4 from X-ray and Neutron Diffraction measurements", *Acta Crystallographica*; B36: 2881–2890

Increasing circularity and material efficiency using ore sand in concrete - A Brazilian case study

L. Bento[1], M. F. L. Menezes[2]*, A. C. L. Alves[3], M. F. Araújo[4], G. Reis[5] and R. J. P. Reis[6]

[1] *Co-log, Belo Horizonte, Brazil*
Email: luciano.bento@cologcoprodutos.com
[2] *Co-log, Belo Horizonte, Brazil*
Email: mariana.menezes@cologcoprodutos.com
[3] *Consultare Labcon, Belo Horizonte, Brazil*
Email: qualidade@consultarelabcon.com.br
[4] *Consultare Labcon, Belo Horizonte, Brazil*
Email: marcelo@consultarelabcon.com.br
[5] *Consultare Labcon, Belo Horizonte, Brazil*
Email: guilherme@consultarelabcon.com.br
[6] *Consultare Labcon, Belo Horizonte, Brazil*
Email: rubens@consultarelabcon.com.br

ABSTRACT

The most common types of fine aggregates for concrete are natural sands and crushed rocks. The ore sand comes from a new source: the iron ore mining sites. The ore is mainly constituted from hematite and quartz and the beneficiation process aims to separate them. The quartz part, that used to be the tailings, can be used as ore sand for concrete. Since this material is already mined and would otherwise goes to dams or dry stacking, using it reduces exploration from the conventional sources of aggregates. Therefore, the ore sand presents a low environmental impact and enables civil construction to become more sustainable. So, this work aims to evaluate the ore sand application in concrete comparing it with the other three most used sands in Belo Horizonte region. This work shows the characterization of this new fine aggregate and compares a range of concrete mixes using ore sand with the ones using natural sand and crushed rocks from local sources in Belo Horizonte, Brazil. It was found that using 30% of ore sand and 70% gneiss crushed rock was the best sand mix in concrete, increasing material efficiency in the whole compressive strength range evaluated and achieving up to 25% reduction on the cement consumption. It can be explained by ore sand morphology plus the improvement of particle packing that allows the concrete optimization.

KEYWORDS: *Ore sand, co-products, concrete, iron ore, tailings*

1. Introduction

Sand is a key raw material for construction, paving, land reclamation and other applications, so UNEP recommends sand should be recognized as a strategic resource. Its extraction, especially in active sand bodies as rivers, when outpaces the natural supply, causes erosion that extends its effect beyond the deposit to the communities downstream the river system, impacting on land-use changes, air pollution, salinisation, fisheries and biodiversity (UNEP (2022), Golev et al (2022), Hackney et al. (2021)).
In Brazil, approximately 500 million tons of aggregates are used (ANEPAC (2020)). On the other hand, only in the state of Minas Gerais, 290 million tons of tailings and overburdens are generated from the mining activity (FEAM (2018)). The use of these tailings as aggregates can increase the circularity of the local concrete and mortar, as recommended by UNEP to search for diversity material and focus on local solutions (UNEP (2022), Golev et al (2022), Vilaça et al. (2022)). In this context, iron ore beneficiation, which consists of grinding, milling and iron concentrating, generates a sandy tailing. This material

characteristics fit well as a fine construction sand (Faria and Menezes (2022), Almada et al (2022), Kuranchie1 et al (2015), Protasio et al (2021), Shettima et al (2016)). This work aims to compare the ore sand use in concrete with the other three most used sands in Belo Horizonte region.

2. Materials and Methods

The characteristics of the aggregates are presented in Table 1 and the iron ore sand typical chemical characterization in Table 2. It is important to mention that ore sand is potentially innocuous for alkali-aggregate reaction (ABNT NBR 15577:2018). It can be noted that the ore sand is finer than the other sands generally used in concrete. Also, its sphericity is greater than the other sands, although the roundness is the lowest one. The cement used was a CP-V-ARI-RS (high initial strength and sulphate resistant) from Holcim. The admixture was a lignosulfonate *Clarena* from GCP.

Table 1 – Characteristics of the aggregates used on the study

Characteristic		Ore Sand	Natural Sand	Gneiss Sand	Limestone Sand	12,5mm Gneiss Gravel	25mm Gneiss Gravel
Particle Size Distribuition – ABNT NM 248:2003. Accumulated retained material in each sieve (%)	19 mm	X	X	x	x	X	11
	12.5 mm	X	X	x	x	X	80
	9.5 mm	X	X	x	x	26	97
	6.3 mm	X	X	x	x	76	100
	4.8 mm	X	1	x	1	90	100
	2.4 mm	X	3	14	25	98	100
	1.2 mm	1	10	37	44	99	100
	0.6 mm	4	36	54	53	99	100
	0.3 mm	8	74	65	56	99	100
	0.15 mm	33	94	77	60	99	100
	Bottom	100	100	100	100	100	100
Maximum Dimension (mm) - NM 248:2003		0.6	2.4	4.8	4.8	12.5	25.0
Fineness Modulus - NM 248:2003		0.46	2.18	2.47	2.90	6.10	7.08
Powdery Material (passing on 75µm) (%) – ABNT NBR 16973:2021		26.4	0.8	13.2	29.0	1.0	0.2
Real Density (kg/dm³) – NBR 16916:2021		2.78	2.73	2.66	2.74	2.66	2.68
Typical Roundness – ISO 13503-1		0.21	0.44	0.25	0.25	x	x
Typical Sphericity - ISO 13503-1		0.74	0.72	0.68	0.70	x	x

Table 2 – Ore sand typical chemical analysis (X-Ray Fluorescence) and Soluble ions (ABNT NBR 9917:2022)

SiO_2	Fe	Al_2O_3	P	Mn	CaO	MgO	TiO_2	Soluble chloride	Soluble sulfate
84%	10.1%	0.36%	0.01%	0.03%	0.01%	0.02%	0.02%	0.01%	<0.01%

The study goal was comparing the main possibilities for fine aggregates mixes for concrete in Belo Horizonte region through particle packing and Abrams' curves evaluation. So, five concrete series with distinct sand blends were tested: 70 % Natural Sand + 30 % Ore Sand (70NS_30OS); 70 % Gneiss Sand + 30 % Natural Sand (70GS_30NS); 70% Gneiss Sand + 30% Ore Sand (70GS_30OS); 70% Gneiss Sand + 30% Limestone Sand (70GS_30LS) and 70% Natural Sand + 30% Gneiss Sand (70NS_30GS). Each serie was composed by four concrete mixes with 0.45, 0.60, 0.75, 0.90 water/cement (w/c) ratio. In order to carry on the study, the basic concrete mix with 0.60 w/c ratio of each serie was calculated, executed and had it water consumption and mortar content adjusted by ACI Method. With the basic concrete mix defined, the other w/c ratio concrete were calculated and executed. The basic mix (w/c approximatly

0.60) for each sand blend is presented in Table 3. For the 20 concrete, the workability was fixed on 120 ± 20 mm slump test result and compressive strength was evaluated for 3, 7 and 28 day.

With these results, Abrams' curves (compressive strenght vs w/c ratio) were adjusted by least squares method for each sand blend concrete serie. In order to understand the material efficency, the cement consumption for the main concrete types demanded by construction market in Brazil (f_{ck} 15, 18, 20, 25, 30, 35, 40MPa) were calculated based on the Abrams' curve.

Table 3 – Basic concrete mix (w/c ratio approximatly 0,60) for each sand blend serie

Concrete Parameter	70NS_30OS	70GS_30NS	70GS_30OS	70GS_30LS	70NS_30GS
Cement (kg/m^3)	324	341	318	355	326
Natural Sand (kg/m^3)	581	259	-	-	-
Ore Sand (kg/m^3)	261	-	-	-	606
Gneiss Sand (kg/m^3)	-	608	556	606	261
Limestone Sand	-	-	250	272	-
9,5mm Gravel (kg/m^3)	306	283	307	286	281
19mm Gravel (kg/m^3)	713	660	715	667	654
Water (l/m^3)	198	196	201	196	189
Aditional water (l/m^3)	+3.0	-3.0	+6.0	-4.0	-3.0
Admixture (l/m^3)	2.59	2.72	2.86	2.84	2.61
Slump (mm)	12.5	12.0	11.0	11.0	12.0

3. Results

The combined sand particle size distribuition for each concrete serie is presented in Figure 1. In order to analise the particle packing, the ideal distribuition for Andreasen (1930), considering 2,4mm maximum dimension and Q as 0.37, is also plotted. It can be noted that the Ore Sand and the Limestone Sand bring the fines below 0,3mm for ideal packing according to Adreasen that lacks when using only gnaisse and natural sand. Since the gnaisse sand has an important ammount of coarser material above 1,2mm, its blend with Ore Sand and Limestone Sand achieves a distribuition close to Adreasen ideal packing.
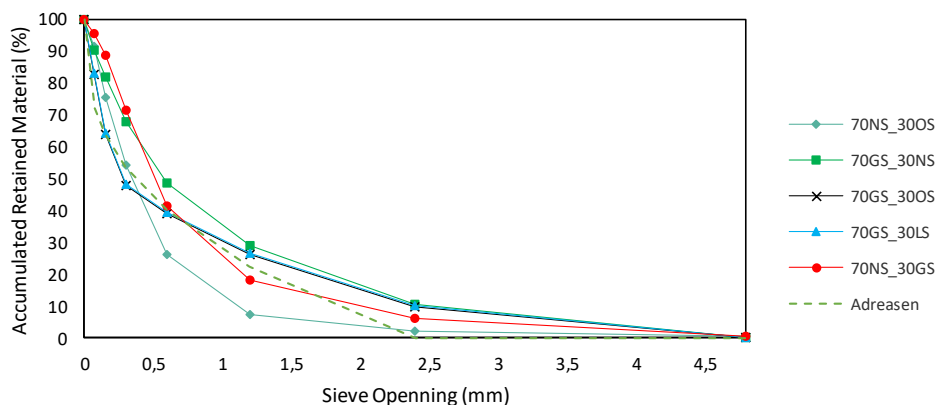
Figure 1 – Sand combined particle size distribuiton for each concrete series and Adreasen distribuition

The concrete results for the 28-day compressive strength and the adjusted Abrams curve for each family is presented on Figure 2. It can be noticed that the R^2 of every serie, is above 0.87, showing a good fit. Comparing the series for each blend, the blend 70% Gneiss Sand + 30% Ore Sand is the one presenting the highest compressive strength in the whole w/c ratio range. Besides this serie, the 70% Natural Sand + 30% Ore Sand is the second best blend on the 0.40 to 0.70 w/c ratio range and on the higher w/c ratio the 70% Gneiss Sand + 30% Natural Sand is the second best pick. The Gnaisse and Ore Sand results can be justified by the particle packing close to ideal Adreasen distribuition, and by the high sphericity of ore

sand and favourable morphology of gnaisse sand, as well. The second best blend being Natural Sand and Ore Sand probably was driven by morphology, since both sands have with high sphericity and high roundness for natural sand, because the combined particle size distribuition was too fine according to ideal Adreasen packing.

The chart shows Compressive Strength (MPa) vs water/cement ratio with the following fitted equations:
$y = 158.54e^{-1.90x}$, $R^2 = 0.98$
$y = 177.21e^{-2.25x}$, $R^2 = 1.00$
$y = 119.34e^{-1.67x}$, $R^2 = 0.93$
$y = 119.21e^{-1.74x}$, $R^2 = 0.87$
$y = 216.65e^{-2.73x}$, $R^2 = 0.99$

Legend: ◆ 70% Natural Sand+30% Ore Sand; ■ 70% Gneiss Sand +30% Natural Sand; ✕ 70% Gneiss Sand +30% Ore Sand; ▲ 70% Gneiss Sand +30% Limestone Sand; ● 70% Natural Sand + 30% Gneiss Sand
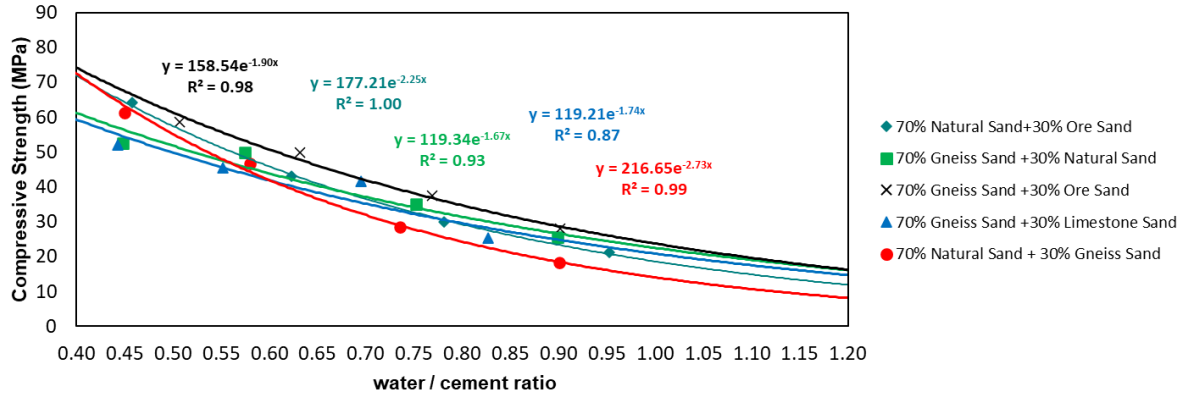
Figure 2 – Abrams' Curves: 28-day compressive strength vs w/c ratio for each sand blend serie

Based on the Abrams's Curves adjustment, the estimated cement consumption for the main market concrete is shown in Figure 3. From the graph, it can be seen that the 70% Gneiss Sand + 30% Ore Sand can diminish cement consumption on the concrete from 10 to 45MPa, reducing up to 25% consumption comparing to the other series. This increase on material efficiency by using the ore sand lowers CO_2 emissions and reduces costs of concrete.

Cement Consumption (kg/m³)

	10	15	18	20	25	30	35	40	45
70% Natural Sand+30% Ore Sand	186	209	222	232	255	281	308	336	368
70% Gneiss Sand +30% Natural Sand	176	202	218	229	258	291	327	367	413
70% Gneiss Sand +30% Ore Sand	159	183	197	207	233	263	295	331	372
70% Gneiss Sand +30% Limestone Sand	183	209	226	237	266	300	337	379	426
70% Natural Sand + 30% Gneiss Sand	212	236	250	260	283	309	336	363	401
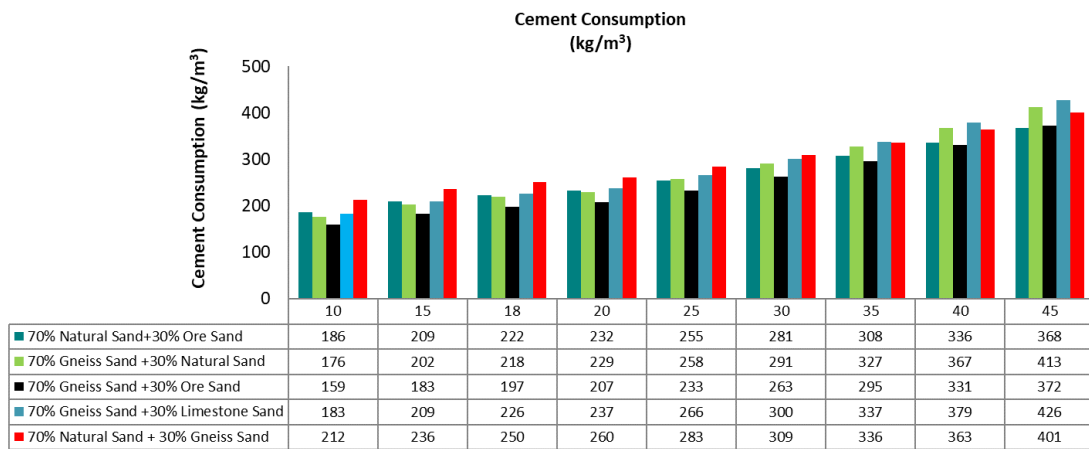
Figure 3 – Cement consumption from f_{ck} 10 to 45MPa concrete for each sand blend

3. Conclusions

The study goal was comparing the available sands mixes for concrete in Belo Horizonte region through Abrams' curves, specially evaluating the ore sand use. The results were consistent that the highest compressive strength in the whole w/c ratio range was the blend 70% Gneiss Sand + 30% Ore Sand. It can be explained by a good particle packing and also by morphology of both sands. This blend allowed to reduce up to 25% cement consumption on concrete, compared to the other sand blends. The second best blend on the 0.40 to 0.70 w/c ratio range is the 70% Natural Sand + 30% Ore Sand. So, besides the circularity gains, using the ore sand enhances the concrete efficency in Belo Horizonte region and contributes to reduce CO_2 emissions of these concrete.

References

Andreasen, A.H.M. and Andersen, J. (1930). "Über die Beziehung zwischen Kornabstufung und Zwischenraum in Produkten aus losen Körnern (mit einigen Experimenten)." *Colloid & Polymer Science*, 50 (3), 217-228.

Almada, B. S., Melo, H. S. S., Duarte, M. S., Aguilar, M. T. P., Garcia, D. C. S, Silva, G. B., Santos, W. S. (2022) "Study of mechanical, durability and microstructural properties of cementitious composite with addition of different iron ore tailings from Brazil." *Journal of Materials Research and Technology*, 18, 1947-1962.

Associação nacional das entidades de produtores de agregados para construção – ANEPAC (2020) *"Panorama ambiental da mineração". Final Report.*

Faria, S. F., Menezes, M. F. L., (2022) "Reduction in cement consumption of concrete by using mining sand" *63rd Congresso Brasileiro do Concreto.*

Fundação estadual do meio ambiente – FEAM (2020) "Dados econômicos." *Final Report*.

Golev, A., Gallagher, L., Vander Velpen, A., Lynggaard, J.R., Friot, D., Stringer, M., Chuah, S., Arbelaez-Ruiz, D., Mazzinghy, D., Moura, L., Peduzzi, P., Franks, D.M. (2022) "Ore-sand: A potential new solution to the mine tailings and global sand sustainability crises" *Final Report*. Version 1.4. The University of Queensland & University of Geneva

Hackney, C.R., Vasilopoulos, G., Heng, S., Darbari, V., Walker, S. and Parsons, D.R. (2021). Sand mining far outpaces natural supply in a large alluvial river. *Earth Surface Dynamics*, 9(5), 1323–1334.

Kuranchie1, F. A., Shukla1, S. k., Habibi1, D. and Mohyeddin, A. (2015) "Utilization of iron ore tailings as aggregates in concrete" *Cogent Engineering*, 2: 1083137

Protasio, F. N. M., Avillez, R.R., Letichevsky, S., Silva, F. A. (2021) "The use of iron ore tailings obtained from the Germano dam in the production of a sustainable concrete" *Journal of Cleaner Production*, 278, 123929.

Shettima, A. U., Hussin, M. W., Ahmada, Y., Mirza, J. (2016) "Evaluation of iron ore tailings as replacement for fine aggregate in concrete." *Construction and Building Materials*, 120: 72–79

UNEP (2022) "Sand and Sustainability: 10 strategic recommendations to avert a crisis", GRID-Geneva, United Nations Environment Programme, Geneva, Switzerland.

Vilaça, A.S.I., Simão, L., Montedo, O.R.K., Novaes de Oliveira, A.P., Raupp-Pereira, F. (2022) "Waste valorization of iron ore tailings in Brazil: Assessment metrics from a circular economy perspective.", *Resources Policy*, 75, 102477.